

Summer 8-15-2018

# Performance Test and Numerical Simulation of an Adjustable Implant for Treating Vocal Fold Paralysis

Hai Zi

hai.zi@maine.edu

Follow this and additional works at: <https://digitalcommons.library.umaine.edu/etd>



Part of the [Biomechanical Engineering Commons](#)

---

## Recommended Citation

Zi, Hai, "Performance Test and Numerical Simulation of an Adjustable Implant for Treating Vocal Fold Paralysis" (2018). *Electronic Theses and Dissertations*. 2913.

<https://digitalcommons.library.umaine.edu/etd/2913>

This Open-Access Thesis is brought to you for free and open access by DigitalCommons@UMaine. It has been accepted for inclusion in Electronic Theses and Dissertations by an authorized administrator of DigitalCommons@UMaine. For more information, please contact [um.library.technical.services@maine.edu](mailto:um.library.technical.services@maine.edu).

**PERFORMANCE TEST AND NUMERICAL SIMULATION OF AN ADJUSTABLE  
IMPLANT FOR TREATING VOCAL FOLD PARALYSIS**

By

Hai Zi

B.S. China Agricultural University, 2013

M.S. China Agricultural University, 2015

M.S. The University of Maine, 2018

A THESIS

Submitted in Partial Fulfillment of the

Requirements for the Degree of

Master of Science

(in Mechanical Engineering)

The Graduate School

The University of Maine

AUGUST 2018

Advisory Committee:

Qian Xue, Assistant Professor of Mechanical Engineering, Advisor

Xudong Zheng, Assistant Professor of Mechanical Engineering, Co-Advisor

Mohsen Shahinpoor, Professor of Mechanical Engineering

© 2018 Hai Zi

# **PERFORMANCE TEST AND NUMERICAL SIMULATION OF AN ADJUSTABLE IMPLANT FOR TREATING VOCAL FOLD PARALYSIS**

By Hai Zi

Thesis Advisor: Dr. Qian Xue, Dr. Xudong Zheng

An Abstract of the Thesis Presented  
in Partial Fulfillment of the Requirements for the  
Master of Science  
(in Mechanical Engineering)

August 2018

Unilateral vocal fold paralysis (UVFP) is one of the most common laryngeal diseases that affect human voice and speech production. It often causes incomplete glottal closure, resulting in voice symptoms including hoarseness, voice fatigue and increased voice effort. One common treatment of UVFP is Thyroplasty Type I, which uses a thyroplasty implant to medialize the paralyzed vocal fold and restore the normal vibration of the vocal fold. However, the surgical outcome is extremely sensitive to the size and shape of the implant. Currently, modifications in the implant size and shape rely upon surgical intuition and experience. The level of voice production restored and satisfaction from patient are variable. Furthermore, the surgical outcome also changes with time as the morphology of the vocal fold changes. In the United States, up to 25% of patients need a revision of the surgery. Therefore, it is desired to have an adjustable implant whose shape and size can be adjusted externally. In this way, the need of reopening the voice box can be permanently removed. This thesis explores employing external forces to control the penetration and shape of the implant. In this way, the contact between the implant and the paralyzed vocal fold can be adjusted as needed. The relationship between the external force, displacement of the implant penetration, and deformation and mechanical stress of the vocal fold was systematically studied in both numerical and experimental ways. Such relationship will inform series of reliably loadings on the device without intensive stress inside the vocal fold. The device is the first step toward a magnetically adjustable implant for Thyroplasty Type I surgery.

## **DEDICATION**

This is dedicated to my parents, Cuiying Li and Zhazhong Zi, who love me, believe in me, inspire me and have supported me every step of the way.

“In addition to burying herself in volumes of books, a consummate scholar frees herself by traveling great distances. “ Without their words, I could never have walked this far...

## ACKNOWLEDGEMENTS

First, I would like to thank Dr. Qian Xue, my advisor and Dr. Xudong Zheng, co-advisor, for introducing me to the fantastic world of mechanical engineering, continually guiding me and giving me knowledge, especially inspiring me to new ideas.

Special thanks to Prof. Mohsen Shahinpoor and S. Ehsan Tabatabaie who encourage me on new ideas and print necessary modes. You offer important contribution to this study. Thanks to Crosby Laboratory Manager Stephen Abbadessa and Administrative Assistant Karen Fogarty who offer help of the current study with their special intelligence, and all of the other wonderful staff in Mechanical Engineering at the University of Maine.

Thanks to group members Biao Geng, Weili Jiang, Geng Liu, Ngoc H. Pham, Jordan Edward Brown for your assistance in my daily research life.

Finally, my sincere appreciation to all of my friends, especially Tiantian Wang and Donghui Hong. When time gets tough, you give me warm encouragement and suggestions.

## TABLE OF CONTENTS

DEDICATION .....	iii
ACKNOWLEDGEMENTS .....	iv
LIST OF TABLES .....	vii
LIST OF FIGURES .....	viii
CHAPTER 1 INTRODUCTION .....	1
1.1 Motivation.....	1
1.2 Background.....	2
1.3 Vocal fold paralysis and medialization surgery .....	7
1.4 Research methods of vocal fold .....	10
1.4.1 Vivo/Excised vocal fold.....	10
1.4.2 Synthetic vocal fold .....	11
1.4.3 Numerical simulation.....	13
1.5 Thesis outline .....	16
CHAPTER 2 EXPERIMENT OF YOUNG’S MODULUS ON SYNTHETIC MATERIAL.....	19
2.1 Introduction.....	19
2.2 Synthetic material generation.....	20
2.3 Testing method.....	21
2.4 Results.....	22

CHAPTER 3 EXPERIMENTS OF VOCAL FOLD DEFORMATION.....	25
3.1 Introduction.....	25
3.2 Methods.....	26
3.2.1 Similarity theory .....	26
3.2.2 Generation of synthetic vocal fold .....	29
3.2.3 Fabrication of testing platform.....	31
3.2.4 Displacement measurement .....	35
3.3 Results and discussion .....	36
3.4 Analysis.....	46
3.4.1 Necessary forces on the prototype of paralyzed vocal fold .....	46
3.4.2 Approximate bilateral symmetry .....	47
3.4.3 Deformation .....	48
CHAPTER 4 NUMERICAL SIMULATION.....	53
4.1 Introduction.....	53
4.2 Methods.....	58
4.2.1 Simulation set up.....	59
4.2.2 Vocal fold part .....	61
4.2.3 Teflon part.....	64
4.3 Results and conclusion.....	66
4.3.1 Comparison of simulations and experiments .....	66
4.3.2 Investigation of adjustable implant .....	68
CHAPTER 5 CONCLUSION.....	77
BIBLIOGRAPHY .....	81
APPENDICES .....	85
BIOGRAPHY OF THE AUTHOR.....	86

## LIST OF TABLES

Table 1. Comparison of experimental results of vocal fold models with different layers to human larynx. ....	13
Table 2. Experimental data and the corresponding Young's modulus .....	22
Table 3. Displacements of Leg 1 and 2 and the corresponding name for 14 experiments.....	37
Table 4. The forces applied on paralyzed vocal fold model in experiments and the necessary forces for prototype in each configuration. ....	46
Table 5. Different meshes used in grid independence (Figure 54). ....	62
Table 6. Comparison of necessary forces between numerical simulation and experiments on four configurations.....	63
Table 7. Comparison of displacements of the monitor point on curve surface of vocal fold model between numerical simulation and experiments. ....	64
Table 8. Draft data of elasticity experiments on synthetic material .....	85

## LIST OF FIGURES

Figure 1. Anatomy of basic components of airway system (Radina, 2016). .....	2
Figure 2. Coronal cross section of larynx and multilayer structure of vocal fold.....	3
Figure 3. Anterior and lateral view of larynx framework (Poppy, 2017). .....	4
Figure 4. Top view of muscles and cartilages around the larynx (Amy 2018). .....	5
Figure 5. Posterior view of muscles and cartilages around the larynx (Karkour, 2018).....	5
Figure 6. A simplified cycle of vocal fold vibration patterns in coronal plane (Story, 2015). .....	7
Figure 7. Examination findings of laryngeal disorder (Anne, 2016). .....	8
Figure 8. Schematic of thyroplasty implant (Buttar, 2017). .....	10
Figure 9. Schematic illustration of autologous thyroid cartilage graft implantation (Tsai, 2017). .....	10
Figure 10. Schematic of multi-layer vocal fold model (Murray, 2011).....	12
Figure 11. Relationship between Young's modulus and volume ratio of silicone thinner. ....	13
Figure 12. Vertical stiffness difference as a function of VMD and subglottal angle (Geng, 2016). .....	15
Figure 13. Three cycles of glottal flow rate and vorticity contours at ten different instants (Zheng, 2011).....	16
Figure 14. The relationship between stress and strain for general metal (Malo, 2017). .....	19
Figure 15. Schematic of testing Young's modulus for synthetic material.....	22
Figure 16. Stress and Young's modulus of synthetic material varies with strain. ....	24
Figure 17. Simplified M5 vocal fold model in normal condition (Murray, 2011).....	25
Figure 18. Three dimensional geometry of M5 and the paralyzed vocal fold used in this study. ....	26
Figure 19. Primitive result of numerical simulation on the relationship between forces applied on Teflon and corresponding displacements.....	27
Figure 20. Negative mode of the paralyzed vocal fold model. ....	29
Figure 21. Separated negative modes of the paralyzed vocal fold model.....	30
Figure 22. 3D printed negative modes of the model of paralyzed vocal fold. ....	30

Figure 23. The prototype of paralyzed vocal fold (right) and the model (left) used in this study. ....	31
Figure 24. Front view of the test platform. ....	32
Figure 25. Vertical view of the test platform. ....	32
Figure 26. Front view of two plates fixed on Teflon. ....	33
Figure 27. Vertical view of two plates fixed on Teflon. ....	33
Figure 28. Front view of the testing platform and paralyzed vocal fold model without loading. ....	34
Figure 29. Vertical view of the testing platform and paralyzed vocal fold model without loading.....	34
Figure 30. Doppler displacement device by Baumer .....	35
Figure 31. The position of Doppler device and marker points on the curve surface of paralyzed vocal fold model. ....	36
Figure 32. Unloading configuration of the paralyzed vocal fold model and Teflon patch. ....	37
Figure 33. Three dimensional coordinates and lateral view of 97 marker points on the undeformed curve surface of vocal fold.....	38
Figure 34. The y coordinates of every point on the curve surface in L0L0R5.2, L0R10.2, and L0R15.2 configurations. ....	40
Figure 35. The external forces applied on Leg 2 when displacements of Leg 2 were 5.2, 10.2, 15.2 mm under the condition of displacement of Leg 1 was 0 mm. ....	41
Figure 36. Different positions of the curve surfaces at L6.0R6.0, L6.0R9.2, L6.0R15.0, L6.0R20.2 configurations. ....	42
Figure 37. The external forces applied on Leg 2 when displacements of Leg 2 were 6.0, 9.2, 15.0, 20.2mm under the condition of displacement of Leg 1 was 6.0 mm. ....	42
Figure 38. The y coordinates of L10.0R10.0, L10.0R15.0, and L10.0R20.0 curve surfaces. ....	43
Figure 39. The external forces applied on Leg 2 when displacements of Leg 2 were 10.0, 15.0, 20.2 mm under the condition of displacement of Leg 1 was 10.0 mm. ....	44
Figure 40. Spatial locations of the curve surfaces when Leg 2 moved from 15.0 to 20.0 mm and Leg 1 was kept at 15.0 mm. ....	45
Figure 41. External forces applied on legs for displacements of Leg 1 at 15.0 and 20.0 mm configurations. ....	45
Figure 42. Y coordinates of marker points on the curve surface of L20.0R20.0 configuration.....	46

Figure 43. Behavior of the curve surfaces when maximum difference between two legs were reached. ....	48
Figure 44. Line numbers on the curve surface (a) and x coordinates of numbered line (b) for L6.0R20.2 configuration. ....	48
Figure 45. Relationship between force on legs and displacements of legs, point 4, 7, and 10 in symmetric configurations. ....	49
Figure 46. Relationship between force on Leg 2 and displacement of Leg 2 under different displacements of Leg 1. ....	50
Figure 47. Relationship between displacement of Leg 2, different points and force on Leg 2 when Leg 1 is at 0 and 6. ....	50
Figure 48. Relationship between displacements of different points and Force on Leg 2 when displacements of Leg 1 are different. ....	51
Figure 49. Forces-rotation relationship considering different kinds of nonlinearities (“Wikiversity”, 2018). ....	56
Figure 50. Finite Element Model of a human knee joint (Naghibi Beidokhti et al., 2016). ....	58
Figure 51. Contact pressure distributions in different time integration algorithms (Naghibi Beidokhti et al., 2016). ....	58
Figure 52. Relative position of the paralyzed vocal fold model and Teflon. ....	59
Figure 53. Boundary conditions for two parts and reference points in numerical simulation. ....	61
Figure 54. Demonstration of mesh on paralyzed vocal fold model. ....	63
Figure 55. Schematic of the position of monitor point on curve surface. ....	64
Figure 56. Geometry of Teflon patch used in numerical simulation. ....	65
Figure 57. Schematic of mesh information used in numerical simulation. ....	66
Figure 58. Comparison of numerical simulation and experiments on relationship between displacements and applied forces of Teflon. ....	67
Figure 59. Comparison of numerical simulation and experiments on relationship between displacements of Teflon and displacements of the monitor point. ....	68
Figure 60. Applied forces on Leg 1 and 2 of Teflon during simulation. ....	69
Figure 61. Displacements of Teflon and paralyzed vocal fold model at the end of step 1 in y direction. ....	70

Figure 62. Displacements of Teflon and paralyzed vocal fold model at the end of step 2 in y direction. ....	71
Figure 63. Applied forces on Leg 1 when displacements of Leg 2 increased.....	71
Figure 64. Relationship of the applied forces and displacements on Leg 2.....	72
Figure 65. Displacements in y direction of the monitor point on curve surface with applied force on Leg 2 increasing. ....	72
Figure 66. Relationship between displacements of monitor point and applied force on each leg when displacement of Leg 1 and 2 was set to 9.2 mm at step 1. ....	74
Figure 67. Von Mises stress distribution across Teflon at the end of step 1.....	74
Figure 68. Von Mises stress distribution across Teflon at the end of step 2.....	75
Figure 69. Relationship between displacements of monitor point and applied force on each leg when displacement of Leg 1 and 2 was set to 13.8 mm at step 1. ....	76
Figure 70. Inner geometry of the built-in base embedded in Thyroid cartilage.....	78
Figure 71. Displacements of the monitor point on curve surface and the corresponding applied force on Leg 2 in prototype of vocal fold and Teflon. ....	78
Figure 72. Relationship between displacements of monitor point and applied force on each leg when displacement of Leg 1 and 2 was 2 mm for prototype of paralyzed vocal fold. ....	79
Figure 73. Relationship between displacements of monitor point and applied force on each leg when displacement of Leg 1 and 2 was 3 mm for prototype of paralyzed vocal fold. ....	79

# CHAPTER 1

## INTRODUCTION

### 1.1 Motivation

Voice plays a significant role in maintaining high quality of life. In particular, some careers (i.e., teachers, waiters, actors, singers, etc.) critically depend on voice. Healthy voice largely depends on the morphology and vibration patterns of the vocal fold. Before phonation, laryngeal muscles will coordinate to bring the two vocal folds from the breathing position, where they are widely apart, to the phonation position, where they are in touch with each other to close the glottis. With the complete close of the glottis, the lung pressure is able to build up. At a threshold, it will separate two vocal folds and induce a propagating mucosal wave on the vocal folds. The propagation of a mucosal wave is an important indicator of healthy voice. Many voice disorders that affect the morphology and mobility of the vocal fold cause an incomplete close of the glottis resulting in an irregular or completely absent mucosal wave. As a result, the voice often becomes breathy and hoarse. For some severe cases, patients can completely lose the voice. According to the report of National Institute on Deafness and Other Communication Disorders (NIDCD), an estimated 17.9 million adults in the U.S. have voice problems (NIDCD, 2018). Among these, unilateral vocal fold paralysis (UVFP) is the most common one. Vocal fold paralysis refers to the loss of nerve supply to one or two the vocal folds. It usually results in an immobile and/or softened vocal fold. One common treatment of UVFP is Thyroplasty Type I surgery which employs a biological implant to push the paralyzed vocal fold to the phonation position to close the glottis. Specifically, during the surgery, the surgeons cut a window through the thyroid cartilage at the level of the vocal fold and insert the biological implant through the window to push the paralyzed vocal fold to the medial position. The surgery attempts to achieve full closure of the glottis, in order for strong vibrations of vocal folds. However, the surgery outcome is extremely sensitive, not only to the size and shape of the implant, but also to the individual patient's vocal fold structural properties which can vary significantly from

individual to individual. At present, modifications in the implant size and shape rely upon surgical intuition and experience. The levels of voice production restored by the surgery and satisfaction rate from patients are variable. Furthermore, the surgical outcome also changes with time as the morphology of the vocal fold changes. In the United States, up to 25% of patients need a revision of the surgery. Therefore, it is desired to have a device, which can adjust the penetration depth and shape of the biological implant externally without reopening the voice box. Such a device will permanently eliminate the need to surgery revision and also often adjust to a fine tune along with the time when the vocal fold morphology changes.

## 1.2 Background

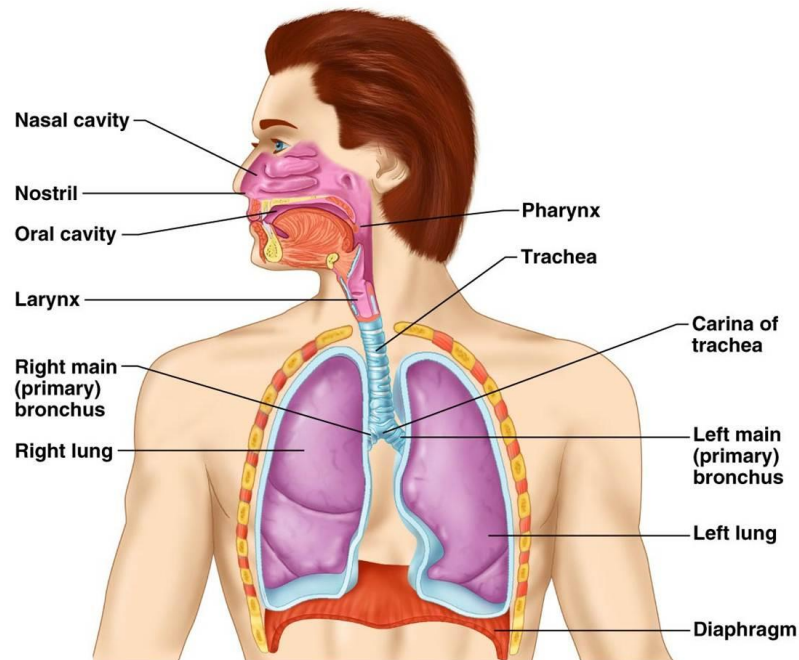


Figure 1. Anatomy of basic components of airway system (Radina, 2016).

Voice production is not only determined by larynx but also by head, neck and chest. A comprehensive understanding of voice production involves many different components, in isolation and in combination. Figure 1 shows the principle components of airway system including lungs, diaphragm, larynx, trachea, nasal and oral cavities. Figure 2 shows details of the coronal cross section of larynx between the trachea and the epiglottis. The narrowest portions in the middle of airway are two vocal

folds. Over vocal folds, another narrow portion are ventricular folds (Titze et al., 1994), also called false vocal folds (Drechsel & Thomson, 2008). Above the false vocal folds is epiglottis, and below the vocal folds is the trachea.

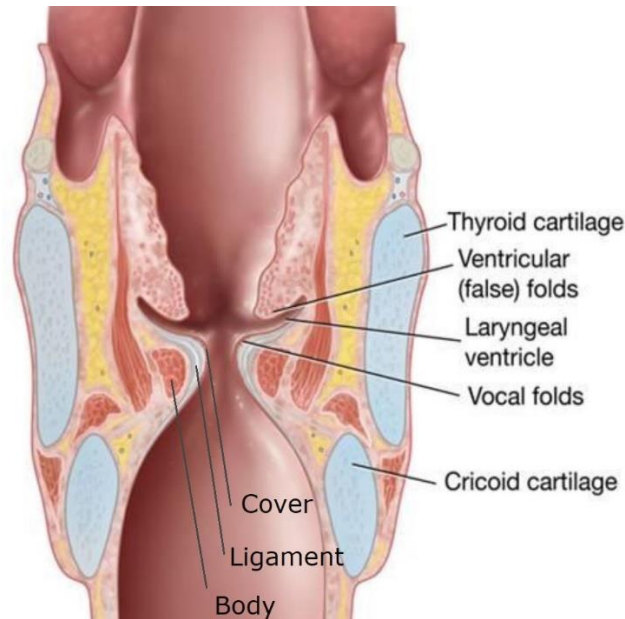


Figure 2. Coronal cross section of larynx and multilayer structure of vocal fold.

The larynx plays a vital role in voice production as it contains the vocal folds. The larynx is also a channel allowing air to pass through and keeping food from blocking airway (Figure 2). In swallowing, sphincter muscles let the larynx move upward in order to block the airway. While in yawning, the pharynx expands and the larynx is compressed and move downward allowing air to pass through. In these behaviors, the larynx can move up and down up to several centimeters (Titze et al., 1994). In front of the vocal fold is the thyroid cartilage, which is also commonly known as the Adam's apple. The cricoid cartilage locates vertically below the thyroid cartilage, forming a ring that surrounds the laryngeal airway. On the top of the posterior part of the cricoid cartilage are two pyramidal arytenoid cartilages. At the base of each arytenoid cartilage are two processes, the posterior muscular process and the anterior vocal process. The movement of arytenoid cartilage can generate adduction for speaking and abduction for breathing and swallowing. The epiglottal chamber, consists of the epiglottis cartilage, and collapses during transportation of solid body and serve as an acoustic resonator during voice production.

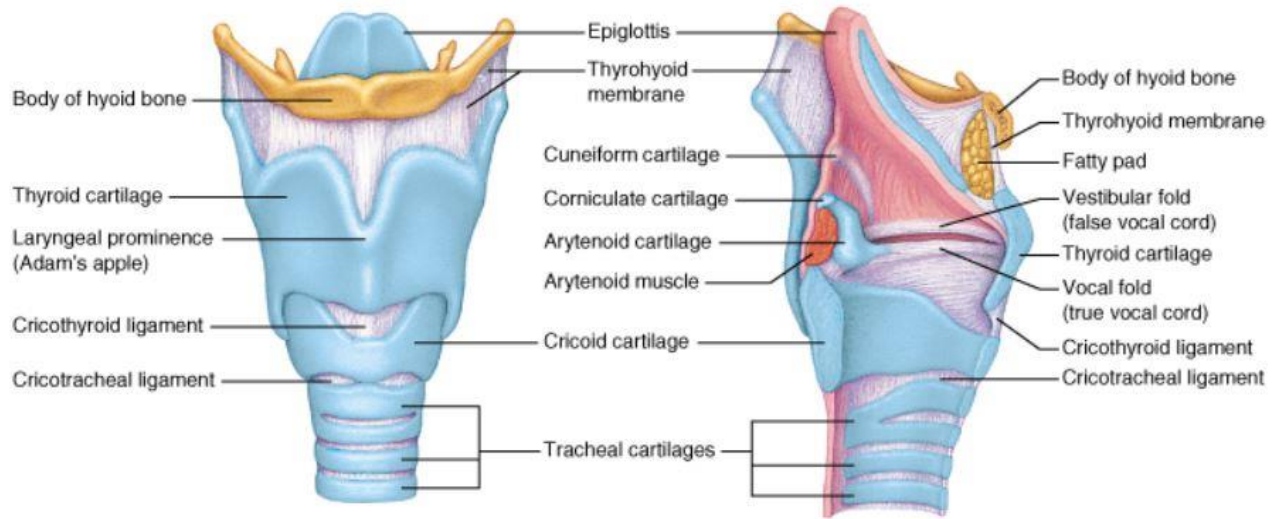


Figure 3. Anterior and lateral view of larynx framework (Poppy, 2017).

In Figure 4, the thyroarytenoid muscle between thyroid and arytenoid cartilages consists most of vocal folds. Starting from the anterior cricoid cartilage, a portion of the cricothyroid muscle is jointed to the thyroid lamina, while another portion is jointed to the thyroid cartilage. Serving as an adductor, a pair of cricoarytenoid muscles starts from the cricoid arch and is linked to the muscular process of arytenoid. A pair of posterior cricoarytenoid muscle connects upward to the muscular process of the arytenoid cartilage, starting from posterior cricoid cartilage.

Specifically, vocal fold is a multilayer structure with different material compositions. From a mechanical point of view, vocal fold can be divided into three layers, cover layer, ligament layer and body layer as shown in Figure 2 (Jiang, Zheng, & Xue, 2017; Xue, Mittal, Zheng, & Bielamowicz, 2012). The superficial layer of vocal fold is the cover layer consisting of a thin epithelium with 0.5 mm approximately in thickness. The ligament, intermediate layer of vocal fold, is 1.1 mm approximately in thickness and consists primarily of elastin fibers in anterior-posterior direction. The major portion of vocal fold is thyroarytenoid muscle in Figure 4 with approximately 7 to 8 mm in thickness, called body layer (Titze, 1994).

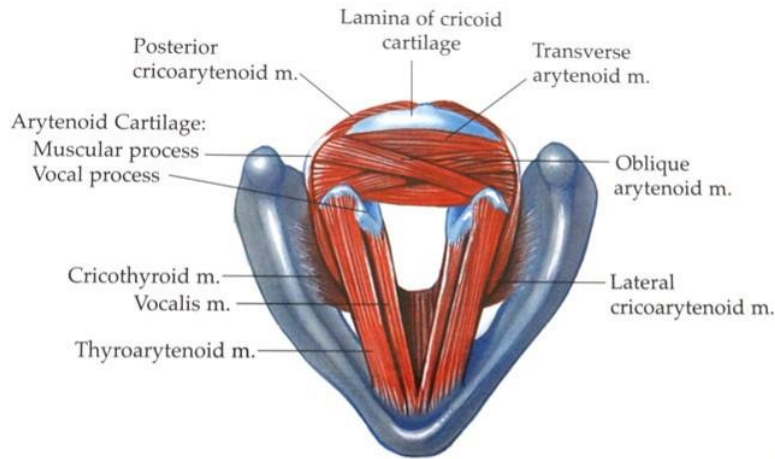


Figure 4. Top view of muscles and cartilages around the larynx (Amy 2018).

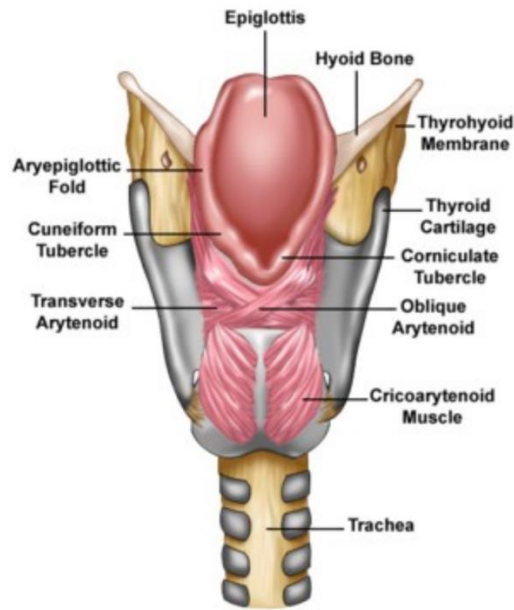


Figure 5. Posterior view of muscles and cartilages around the larynx (Karkour, 2018).

The production of voice is an extremely complex behavior involving different components but can be basically simplified as a general sound produced by a musical instrument. There are three principle parts for any sound produced by instrument: the vibrator, activator, and resonator. The lungs and abdomen serve as an activator which is the source of energy. When the vocal folds are adducted, the compression of air in lungs is done by diaphragm. The vocal folds serve as the vibrator obtained energy from the flow field. When the pressure exceeds a certain threshold pressure, the exhaled air from lungs

pass through the vocal folds generating pressure difference due to Bernoulli effect. The vocal folds are excited into a self-sustained vibration in this way. The initial sound is made. The movement of body layer of vocal fold (vocalis muscle in Figure 4) can also be adjusted by arytenoid cartilage which is controlled by cricoarytenoid muscle via recurrent laryngeal nerve. In this way, human brain can adjust the movement of vocal folds suggesting the pitch and loudness of sound can be changed. The cavities in head work as the resonators indicating voice timbre can be generated (Benninger, Murry, & Johns, 2015).

A simplified cycle of vocal fold vibration patterns is demonstrated in chronological sequence in Figure 6. At first when  $t=1$ , the vocal folds are just in contact with each other due to close of glottis. The arrows suggest the moving directions of vocal folds. At this time, the left and right vocal folds are moving in opposite direction away from midline. They are continuously taking apart in next two figures ( $t=2$  and  $t=3$ ) until the maximum gap is achieved at frame  $t=4$ . In frames  $t=4$  and  $t=5$ , the lower portion of vocal folds turn to move to the middle, whereas, the upper portion of vocal folds are continuously separated. In frames  $t=6$  and  $t=7$ , the upper portion of vocal folds follow the direction of lower portion, moving to the middle. At the end of one cycle when  $t=8$ , the lower parts of vocal folds contact with each other blocking the airway. The frequency of this cycle is over 100 Hz during vocal fold vibration (Story, 2015). Note that during voice production the upper parts of vocal folds are always following the pace of the lower portion resulting in a wave-like motion from bottom to top called “mucosal wave”.

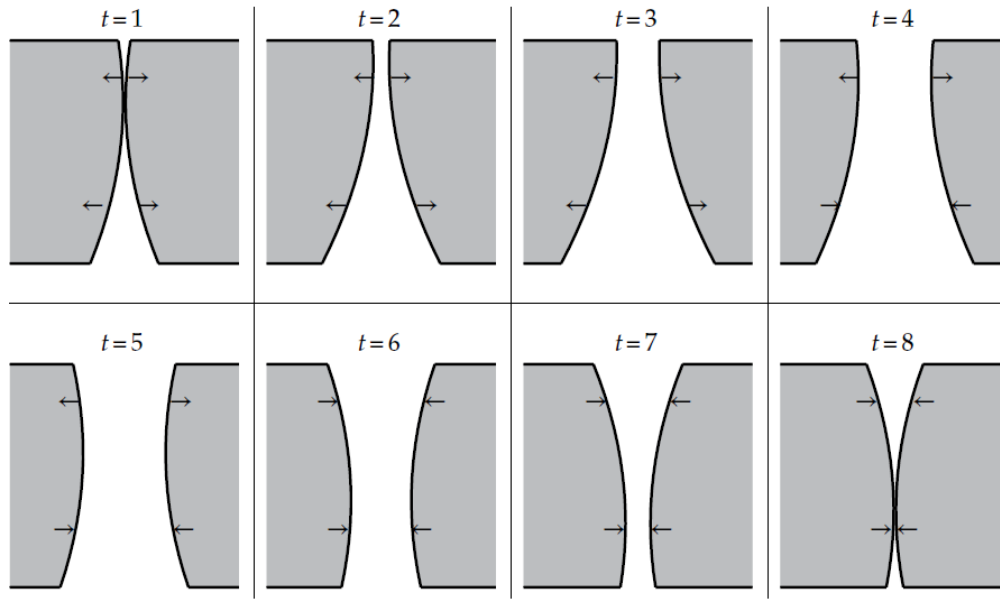


Figure 6. A simplified cycle of vocal fold vibration patterns in coronal plane (Story, 2015).

### 1.3 Vocal fold paralysis and medialization surgery

There are different kinds of diseases and causes relating to vocal fold paralysis shown in Figure 7. Among these, unilateral vocal fold paralysis (UVFP) is the most common one due to the loss of recurrent laryngeal nerve supply to one or both sides of the vocal folds. Figure 7(b) shows the morphologies of vocal fold bowed paralysis in left side. Paralysis can affect the ability to speak, even breathe due to that vocal folds not only participate sound production but only protect airway by preventing food and drink. Symptoms of vocal fold paralysis can involve hoarseness, noisy breathing, loss of vocal pitch, and choking or coughing when swallowing food and drink.

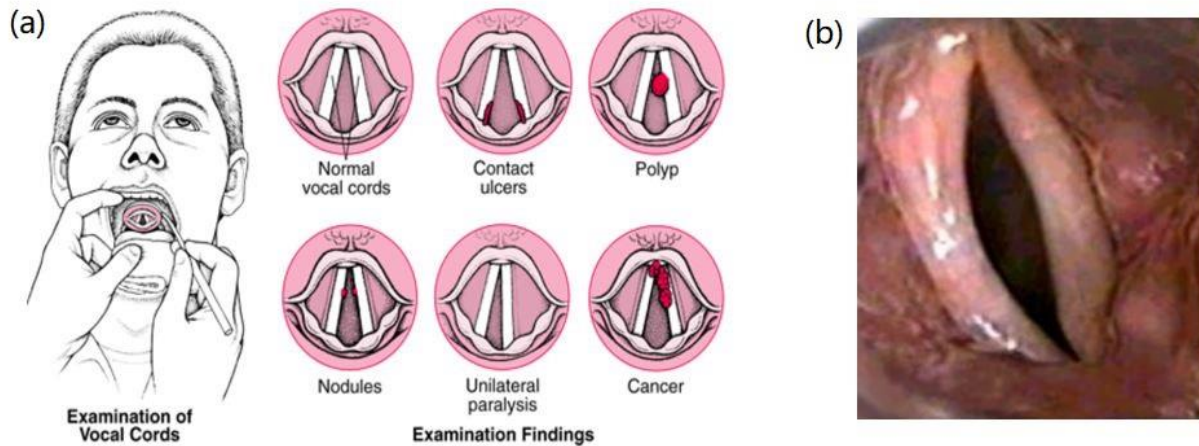


Figure 7. Examination findings of laryngeal disorder (Anne, 2016).

There are different reasons for vocal fold paralysis includes surgery/trauma in neck, malignancy, stroke, even viral infections (Sulica & Blitzer, 2006). Laryngoscopy and laryngeal electromyography were commonly employed as main diagnosis methods (Mayo, 2018). Depending on different causes, the severity of symptoms, and initial time of symptoms, there are different treatments including voice therapy, bulk injections and so on. A significant improvement of voice quality even quality of life are found under voice therapy (Schindler et al., 2008).

Thyroplasty Type I, or called Isshiki technique, is the most commonly used surgical procedure to correct UVCP. In this type of thyroplasty, material is pushed to the middle region through a window at thyroid cartilage on neck under local anesthesia. For this technique in 1970s, silicone was used as material to be pushed to the paralyzed side (Friedrich, 1999). Transcutaneous interfold silicone was also injected into the paralyzed vocal fold (Hirano, 1990). Taken different parameters into consideration, most of outcomes were excellent after surgeries, while some surgeries failed due to insufficient silicone. Autologous fat, an alternative for silicone, was investigated on dogs in vocal fold paralysis (Zaretsky, 1995). Other biomaterials had been used in vocal fold surgery including collagen, glutaraldehyde crosslinked collagen, absorbable gelatin, human abdominal subcutaneous fat, and vocal fold mucosal tissue. Based on experiments of different biomaterials on viscosity, human fat have shown similar material properties with vocal fold (Ingo Titze, 1997).

There are also some disadvantages for silicone as implant material involving long time-consuming, risk of dislocation, and difficulty of fixation. Instead of a bulk injection like silicone, structural implants are also used to reposition the paralyzed vocal fold (Figure 8). A medical titanium implant was developed with several advantages involving excellent biocompatibility, extraordinary fixation and stabilization (Friedrich, 1999). Another material which is a thyroid cartilage was used in medialization laryngoplasty suggesting excellent biocompatibility (Figure 9) (Tsai et al., 2017). In Montgomery thyroplasty implant system, three parts have been employed to treat unilateral vocal fold paralysis: a medicalization implant, measuring devices, and surgical instruments. These surgical instruments are designed for locating and creating the thyroplasty window in thyroid lamina. The measuring devices are used to measure medialization distance to determine the suitable implant size. The implant consists of two major components: a rectangular base and a triangular top. The base made of firm silicone has three tiers: the outer tier locates on the outer surface of the thyroid lamina preventing medial displacement, the middle tier prevents rotation, while the inner tier protects against outward displacement. The triangular top is made of soft silicone to medialize the paralyzed vocal fold. The height of triangular part varies with five sizes for females (6 to 10 mm) and five sizes for males (8 to 12 mm) in 1997 then developed to six female sizes (6 to 11 mm) and six male sizes (8 to 13 mm) at present (Montgomery, 1997). This kit is available at Boston Medical Products company. The VoCoM system for vocal fold medialization employs different sizes and shapes of implants made of hydroxyapatite. The main advantage of this hydroxyapatite implant is long biocompatible clinical use. Moreover, a malleable implant consisting of homopolymer of polytetrafluoroethylene, called Gore-Tex or Teflon, can be used for medialization surgery through a window on neck. The following study is based on the Teflon material.

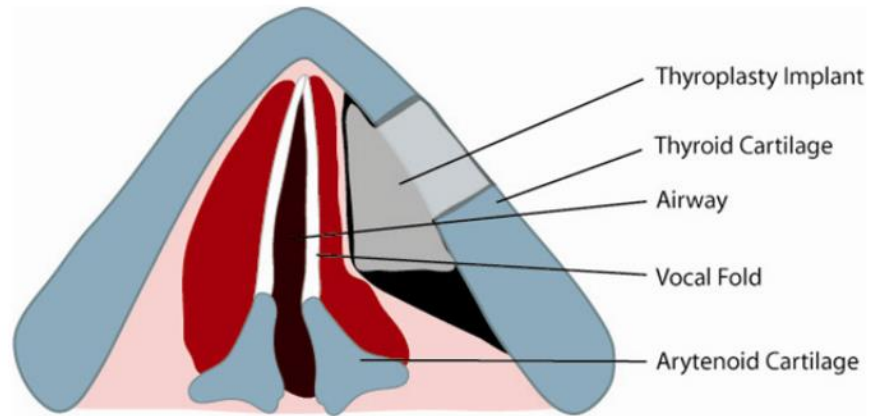


Figure 8. Schematic of thyroplasty implant (Buttar, 2017).

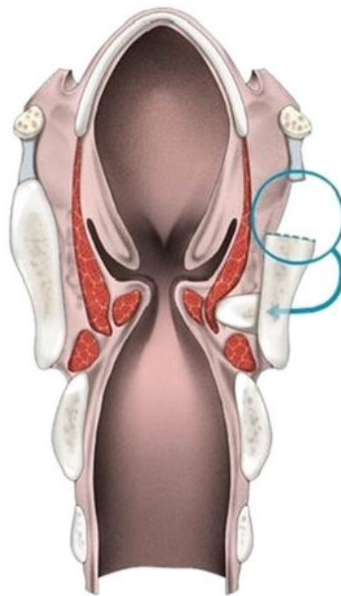


Figure 9. Schematic illustration of autologous thyroid cartilage graft implantation (Tsai, 2017).

## 1.4 Research methods of vocal fold

### 1.4.1 Vivo/Excised vocal fold

Vivo or excised laryngeal models are ideal materials to study voice production as they represent the realistic conditions. Digital kymograms have been used as a powerful tool for visualization and classification of vocal fold vibration. They are also used for biomechanical (Wittenberg, Tigges, Mergell, & Eysholdt, 2000). This technique can date back to the 1970s. Clinically, phonation onset, irregular vocal

fold vibration, particular anterior-posterior vibration modes and running speech had been quantitatively investigated with the help of this technique. Microstructures were mounted on the surface of excised human vocal folds in order to track the movement of the surface by a digital camera (Doellinger & Berry, 2006). The vibrations were monitored under different boundary conditions involving glottal airflow, a force applied to the muscle in vocal fold and force on the thyroid cartilage. Only different glottal airflow yielded significant effect on vibration. In addition, animal larynges (e.g. porcine, canine) were also employed in experiments. An excised porcine larynx was investigated to study nonlinear behavior of vocal fold vibration (Giovanni et al., 1999). However, due to some disadvantages of vivo/excised vocal fold involving limited access, opacity, deterioration and shrink after a short period, vivo vocal fold is not the best material in experiment.

#### **1.4.2 Synthetic vocal fold**

Synthetic vocal folds have been increasingly used to study vocal fold vibrations. They usually fall in to three categories: static, driven and self-oscillating. Static vocal folds employ same geometries with true vocal folds with no motion. They are useful in investigating the relationship between pressure and velocity in different vocal fold configurations. In experiments, metal models of vocal fold were fixed in wind tunnel with three different glottal divergence angles (Erath & Plesniak, 2006). One of rigid vocal folds was driven by a piston connecting an electrical motor to study the pressure distribution within glottis (Deverge et al., 2003). The advantages of static rigid vocal folds are no strict requirement on material properties, fabrication and operation.

In recent years, self-oscillating synthetic vocal fold was successfully developed. The model has evolved from simple geometries to realistic human laryngeal geometries. Most synthetic vocal folds were generated by combination of three solutions (Ecoflex 0030 A, Ecoflex 0030 B and silicone thinner) in different volume ratio. Originally, volume ratio of Evergreen 10 part A: Evergreen 10 part B: Everflex at 1:1:4 was used to fabricate a one-layer vocal fold model with Young's modulus of 13.7 kPa (Thomson,

Mongeau, & Frankel, 2005). In this study, self-oscillating frequency and onset pressure were obtained but experimental results did not agree well with results obtained in a human excised larynx. Another researcher employed the same synthetic model to study the glottal flow structure involving vortex generation, convection and jet flapping based on modern flow visualization and digital particle image velocimetry (Neubauer, Zhang, Miraghaie, & Berry, 2007). In later work, this one-layer synthetic model was evolved to two-layer model: cover layer and body layer. The body and cover layer had Young's moduli of about 22.5 and 4.1 kPa under different volume ratios of solutions (Drechsel & Thomson, 2008). With this two-layer model, vibration frequency, pressure distribution, flow rates and flow structures were investigated. Another two-layer model, cover layer with 4 kPa and body layer with 10 kPa, was used to study the influence of air sacs connecting main vocal tract in human relatives (Riede, Tokuda, Munger, & Thomson, 2008). In total, the experimental results of two-layer model were more accurate than the previous one-layer model. However, due to the orthotropy of human vocal folds, an acrylic fiber with the Young's modulus of 2.8 GPa was embedded into ligament layer in anterior-posterior direction as reinforce material shown in Figure 10. The behavior of this multi-layer synthetic vocal fold model agreed well with published data of excised human larynx. Table 1 compared three experimental parameters of vocal fold models with different layers to human larynx based on references. For onset pressure of voice production and frequency of vocal fold vibration, the range of four-layered vocal fold model agreed well with data of human larynx. Only the flow rate of four-layered vocal fold models beyond the range of human larynx.

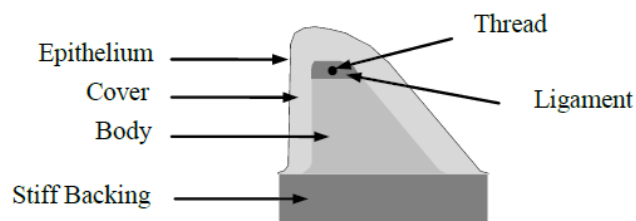


Figure 10. Schematic of multi-layer vocal fold model (Murray, 2011).

Table 1. Comparison of experimental results of vocal fold models with different layers to human larynx.

Model	Onset Pressure (kPa)	Frequency (Hz)	Flow Rate (ml/s)
One-layer	1.15		169
Two-layer	0.48	132	103-232.2
Four-layer	0.27-0.37	87-102	270-500
Human larynx	0.29-0.49	98-246	70-200

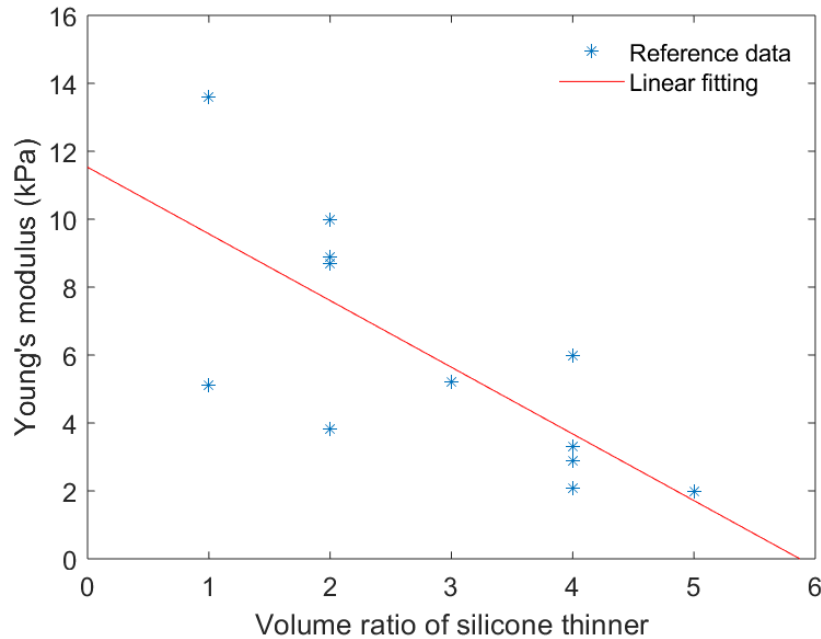


Figure 11. Relationship between Young's modulus and volume ratio of silicone thinner.

Based on references, the volume ratio of Ecoflex 0030 part A and B was always same 1:1. Figure 11 shows the Young's modulus after generation with different volume ratios of silicone thinner in references. It is worth noting that the difference of Young's modulus was quite large in different references although the volume ratio of silicone thinner was same. However, there is a negative relationship between silicon thinner and the resulting Young's modulus. In other words, more silicon thinner suggested small Young's modulus.

### 1.4.3 Numerical simulation

Numerical simulation has also been increasingly used to study voice production. Computer models have evolved from early two-mass type of model to recently continuum mechanics based model. They have provided a supplemental approach for studying quantities that are extremely difficult or even

impossible to measure through experimental approaches. The finite element model (FEM) was a commonly used model for analyzing the deformation and stress inside the vocal fold (Thomson et al., 2005). Finite element model also contributed to find the stresses distribution across the vocal fold during contact of two vocal folds (Gunter, 2004; J. J. Jiang, Diaz, & Hanson, 1998). A 3D three-layer isotropic vocal fold model based on FEM was used to quantitatively investigate the airflow velocity and pressure distribution as well as vocal fold displacement (Rosa, Pereira, Grellet, & Alwan, 2003). Based on commercial finite-element package (ABAQUS), different voice disorders were analyzed involving inhomogeneous anisotropic material properties and complex boundaries (Alipour, Berry, & Titze, 2000). The contact force between two vocal folds had a strong relation with Von Mises stress, compressive stress, and vertical shear stress (Gunter, 2003). The FEM model also verified that the vocalis and muscularis parts of the thyroarytenoid muscle played important roles in arytenoid movement (Hunter, Titze, & Alipour, 2004). Based on finite-element model, the impact pressure was found to be the square root of lung pressure approximately (Tao, Jiang, & Zhang, 2006). Derived from CT images, 3D finite-element model of the vocal tract was employed to quantitatively study variations in vocal tract input impedance. (Vampola, Laukkanen, Horacek, & Svec, 2011). The FEM was also used to quantify the influence of different material stiffness and the subglottal skew angle of vocal fold. Figure 12 shows the difference of vertical stiffness has relationship with the vertical material difference (VMD) and subglottal convergence angle (Geng, Xue, & Zheng, 2016).

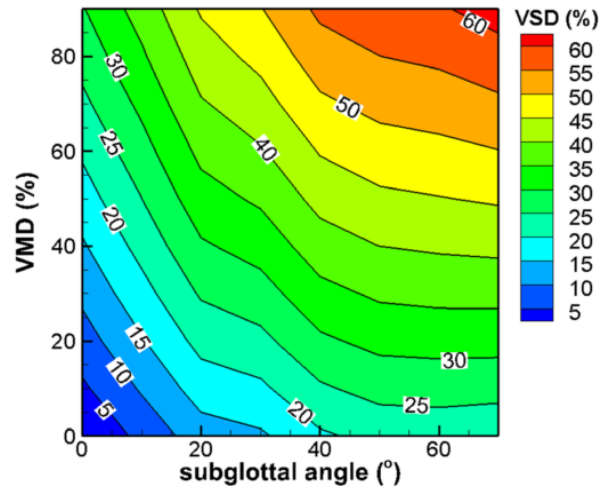


Figure 12. Vertical stiffness difference as a function of VMD and subglottal angle (Geng, 2016).

It is shown that the Immersed Boundary Method (IBM) is an extremely accurate and versatile approach due to the strongly coupled interaction between airflow and elastic vocal folds (Peskin, 2002; Mittal and Iaccarino, 2005; Mittal *et al.*, 2008; Mori and Peskin, 2008; Atzberger, Kramer and Peskin, 2009; Seo and Mittal, 2011). Two-dimensional IBM was employed to investigate the flow structure under asymmetric glottal jet (Zheng, Mittal, & Bielamowicz, 2011). Another two-dimensional model was used to obtain frequency of the self-sustained vocal fold vibration which was similar to normal human phonation (Zheng *et al.*, 2011).

A coupled sharp-interface immersed-boundary-finite-element method was employed to simulate flow-structure interaction. The coupled solver suggested robust and accurate results for complex flow structure interaction problems (Zheng *et al.*, 2011). Results involved, but not limited to, the cycle of glottal flow rates (Figure 13), open quotients, glottal shape in different configurations, and vibration amplitude (Zheng *et al.*, 2011). The simulation results agreed well with established human data. The limitations of numerical simulation include, but not limited to, long simulation time, a turbulence transition, mucosal wave propagation (Murray, 2011; Xue *et al.*, 2012).

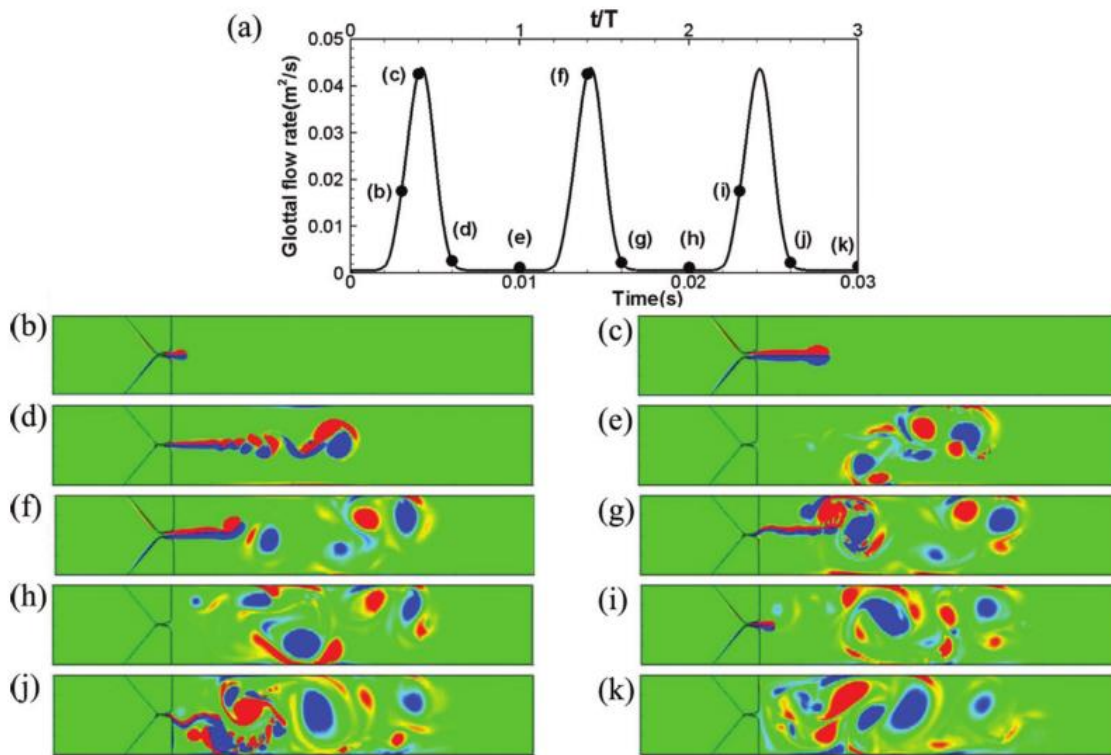


Figure 13. Three cycles of glottal flow rate and vorticity contours at ten different instants (Zheng, 2011).

### 1.5 Thesis outline

In this study, a new adjustable device suitable to every patient will be measured in order to replace up to 12 different sizes of implants. The aims of this study are:

1. Generating a synthetic vocal fold and Teflon based implant model to simulate the implant insertion process;
2. Finding the relationships between the forces on legs of Teflon implant, the corresponding displacements of legs and deformation of the curve surface on vocal fold;
3. Develop a nonlinear computer model to simulate the process;
4. Examine the relationship between experiments and numerical simulation.

The organization of this thesis is as follows.

Chapter 2 is experiment of Young's modulus on synthetic material. In this chapter, synthetic material which was used in this study was generated at first. A simple test device suitable for a synthetic cuboid was made to test the Young's modulus of this synthetic material when the cuboid was applied by different external forces. The relationship between stress and strain which is a curve suggesting nonlinear behavior of this synthetic material was found at the end of this chapter.

Chapter 3 is experiments of synthetic vocal fold model deformation. In this chapter, similarity theory was employed at first to find approximate forces which was suitable to be measured in experiment by amplifying the prototype of vocal fold. Afterwards, synthetic paralyzed vocal fold model was generated. A test platform for investigating the relationship between the applied forces on legs of Teflon and the deformation of the curve surface will be introduced in details. Based on this test platform, 14 groups of experiments will be implemented to measure the relationship between displacements of legs of Teflon and corresponding applied forces for both symmetric and asymmetric configurations, including the three-dimensional shape change of vocal fold. Two conclusions involving the necessary forces on prototype and bilateral symmetry will be explained in details at end.

Chapter 4 is numerical simulation. Under the same boundary conditions in experiments in chapter 3, the results from numerical simulation and experiments will be compared as a validation for numerical simulation suggesting numerical simulation is a convincing tool. Afterwards, different boundary conditions similar to conditions in surgery are used to simulate processes in reality. The relationship in surgeries between the deformation of curve surface on paralyzed vocal fold synthetic model and the displacements of different legs of Teflon, and the necessary forces applied on legs are investigated quantitatively with the help of numerical simulation.

Chapter 5 is conclusion. The results of numerical simulation agrees well with results from experiments. The relationships used on the prototype in surgery are concluded from the model.

Appendix A provides draft data of experiments in chapter 2 and 3 in details.

## CHAPTER 2

### EXPERIMENT OF YOUNG'S MODULUS ON SYNTHETIC MATERIAL

#### 2.1 Introduction

Elasticity including Young's modulus, shear modulus, and bulk modulus is the inherent property of a material as a resistance to deformation under external applied loads. In this study, only Young's modulus is studied. Young's modulus is a measure of the ability of one material to withstand changes under tension or compression. Young's modulus can be described by a relationship of stress and strain, which is a curve showing the relationship between the average applied force per unit area called stress and the deformed length per unit length called strain. Figure 14 shows the relationship between stress and strain for general metal material. In general, the curve is nonlinear beyond the elastic limit shown in Figure 14. However, under the condition of small deformation ( $-20\% \leq \varepsilon \leq 20\%$ ), the stress has an approximately linear relationship with strain. Within the elastic limit, the slope of stress-strain curve is the Young's modulus for one material.

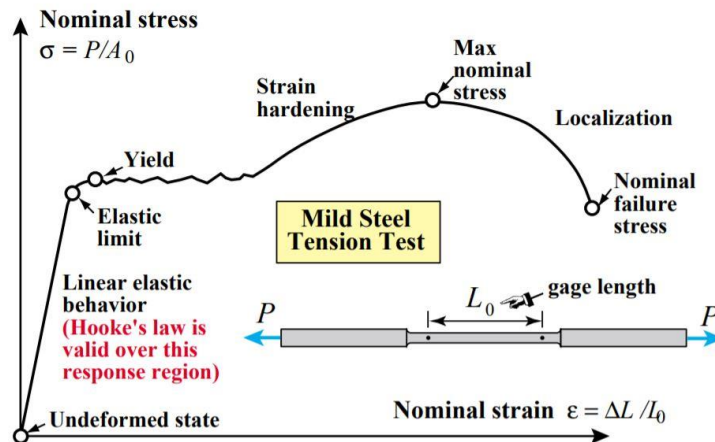


Figure 14. The relationship between stress and strain for general metal (Malo, 2017).

In general, the Young's modulus is measured by tension and/or compression via experiments.

Samples in different shapes have been used to measure the Young's modulus. A cylindrical sample which

was 2.54 cm in diameter and 1.3 cm in height was tested using an EnduraTECELF 3200 test instrument (Thomson et al., 2005). Another cylinder specimen which was 8 mm in diameter and 50 mm in length was tested in an Instron 3342 tensile test device. In another experiment, the strain of each cylinder specimen reached 40% but the Young's modulus was only valid within the range of 20% (Murray, 2011). Another Young's modulus in a tension experiment was obtained by using cylindrical specimen which was 8 mm in diameter and 6 cm in length but the strain ranged within 40% not 20% (Riede et al., 2008). The Young's modulus was measured using a new technique, Indentation method (Chhetri, Zhang, & Neubauer, 2011) where the indentation diameter is 1 mm and the indentation depth is 1 mm (Mendelsohn, 2011). Another Young's modulus was tested within the range of 0-20% (Zhang, Neubauer, & Berry, 2006). When incompressibility is assumed (Kerdok et al., 2003), the Young's modulus can also be obtained from shear modulus by the following equation:

$$G = \frac{E}{2(1+\nu)} \quad (2-1)$$

Based on Figure 11, the tested Young's modulus varied in different years and researchers under the same volume ratio of silicone rubber to silicone thinner from the same product Ecoflex 0030 (Smooth-On, Inc.). For example, when the volume ratio of Ecoflex 0030 A: Ecoflex 0030 B: silicone thinner was 1:1:1, the Young's modulus was 13.6 kPa from researcher Spencer in 2008, whereas 5.51 kPa from researcher Zhang in 2011. As a result, the Young's modulus should be measured in this study.

## 2.2 Synthetic material generation

Elasticity is the inherent property of one material, regardless of the cross section area of a specimen. In order to apply external distributed forces uniformly on the cross section area, a cuboid specimen which was 156.9 mm in length, 13.0 mm in width, and 6.0 mm in height was used to measure the Young's modulus of the synthetic material in this study.

In step 1, a negative mode of this cuboid was made using SolidWorks and printed by three dimensional printer. The Young's modulus of body layer which is the major portion of vocal folds ranges from 10 to 30 kPa in different references. As a result, the volume ratio 1:1:1 is selected in step 2 to generate the synthetic material. Three solutions Ecoflex part A, Ecoflex part B, and silicon thinner with same volume ratio were mixed well before uniformly injected into the negative mode. In step 3, the mixed solutions cured to a solid cuboid body after 24 hours at room temperature.

### **2.3 Testing method**

A cuboid specimen which was 156.9 mm in length, 13.0 mm in width, and 6.0 mm in height was generated to measure the Young's modulus of the synthetic material in this study. One end of the specimen was fixed while the other end was attached different weights suggesting external forces as shown in Figure 15. Compared to the original length in horizontal position, the elongation due to gravity was relatively small. As a result, the valid length of this specimen without loading was 132.1 mm.

During this experiment, 21 weights indicating gradually increased external forces were applied on the bottom tape one by one. In each interval, the applied force and the corresponding valid length were recorded when the system became static. This measurement was repeated two times in order to decrease measurement error by taking the average of valid lengths under same applied forces.

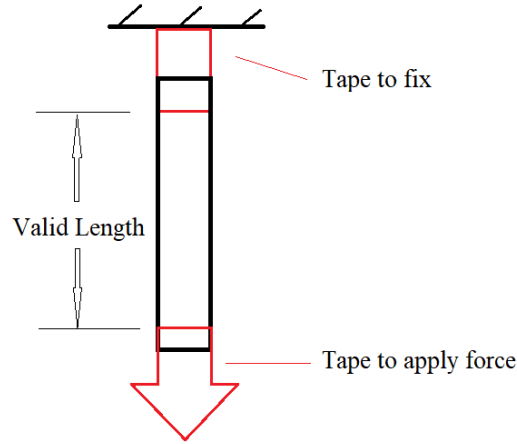


Figure 15. Schematic of testing Young's modulus for synthetic material.

## 2.4 Results

Table 2 shows the external forces applied on the specimen and the corresponding elongation, and the original draft data is attached in Appendix A. As a result, the stress can be calculated as force per unit area. Meanwhile, the strain can be calculated as deformation per unit length. Specifically, based on the first applied force, the Young's modulus can be calculated as below:

$$E = \frac{\text{stress}}{\text{strain}} = \frac{F / A}{\Delta L / L} = \frac{F \cdot L}{\Delta L \cdot A} = \frac{0.03668 \cdot 0.1321}{0.0022 \cdot 0.000078} = 28234.4 Pa \quad (2-2)$$

Table 2. Experimental data and the corresponding Young's modulus

Weight No.	Force (N)	Unload Length (m)	Elongation (m)	Unload Area (m <sup>2</sup> )	Stress	strain	E (Pa)
0	0	0.1321	0	0.000078	0	0.0%	
1	0.03668	0.1321	0.00220	0.000078	470.2	1.7%	28234.4
2	0.05502	0.1321	0.00330	0.000078	705.3	2.5%	28234.4
3	0.06374	0.1321	0.00405	0.000078	817.2	3.1%	26655.5
4	0.07845	0.1321	0.00500	0.000078	1005.8	3.8%	26573.5
5	0.16181	0.1321	0.01115	0.000078	2074.5	8.4%	24577.5
6	0.23536	0.1321	0.01700	0.000078	3017.4	12.9%	23447.2
7	0.44130	0.1321	0.03650	0.000078	5657.7	27.6%	20476.2
8	0.90712	0.1321	0.09155	0.000078	11629.7	69.3%	16780.8
9	1.08854	0.1321	0.11675	0.000078	13955.6	88.4%	15790.5

10	1.24544	0.1321	0.13885	0.000078	15967.2	105.1%	15191.0
11	1.29448	0.1321	0.14575	0.000078	16595.9	110.3%	15041.6
12	1.45138	0.1321	0.16595	0.000078	18607.5	125.6%	14812.0
13	1.61810	0.1321	0.18675	0.000078	20744.8	141.4%	14674.1
14	1.74558	0.1321	0.20340	0.000078	22379.3	154.0%	14534.4
15	1.90249	0.1321	0.22220	0.000078	24390.9	168.2%	14502.8
16	2.15746	0.1321	0.24740	0.000078	27659.8	187.3%	14769.0
17	2.34379	0.1321	0.26425	0.000078	30048.6	200.0%	15021.4
18	2.54973	0.1321	0.28665	0.000078	32688.8	217.0%	15064.3
19	2.66741	0.1321	0.29290	0.000078	34197.5	221.8%	15421.6
20	2.87335	0.1321	0.30800	0.000078	36837.8	233.2%	15799.6
21	3.16755	0.1321	0.32405	0.000078	40609.6	245.3%	16553.8

Figure 16(a) shows the relationship between stresses and strains in the range of  $0 < \varepsilon \leq 245\%$ . In general, the relationship of stress and strain can be assumed linearity within a small range  $0 < \varepsilon \leq 20\%$ . As a result, the slope of stress and strain curve within small range is the Young's modulus. However, beyond the small range of strain, strong nonlinearity between stress and strain is shown in Figure 16(a). Figure 16(b) shows that Young's modulus of synthetic material varies with strain. The young's modulus decreases from 28234.4 Pa to 14502.8 Pa, then increases to 16553.8 Pa when strain is 245.3%. This decrease-increase trend of stress-strain curve agrees well with the nonlinear behavior of rubber material. The tested values of Young's modulus of synthetic material ranges within the range of Young's modulus in references. This stress-strain curve is limited to the condition where the volume ratio of Ecoflex 0030 A: Ecoflex 0030 B: Silicone thinner was 1:1:1.

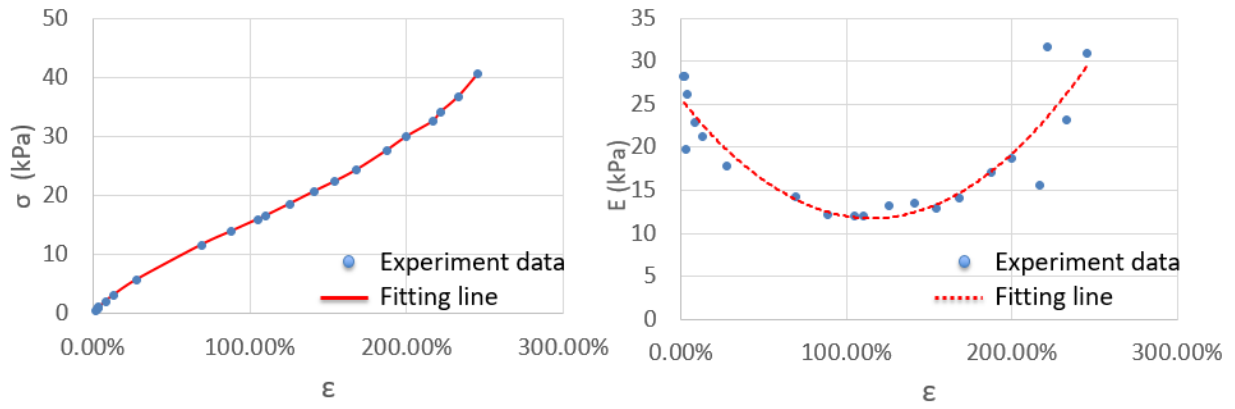


Figure 16. Stress and Young's modulus of synthetic material varies with strain.

## CHAPTER 3

### EXPERIMENTS OF VOCAL FOLD DEFORMATION

#### 3.1 Introduction

Simplified geometry model of vocal fold in normal condition M5 (Scherer et al., 2001) has been widely used for both experiments and numerical simulations. Experiments were performed to quantify the influence of different material and geometric parameter on the flow-induced responses based on M5 model (Brian A Pickup, 2010). Numerical simulations were performed to investigate the asymmetric deflection of glottal jet based on 2D M5 (Zheng et al., 2011). Four vocal fold models based on M5 (Figure 17) were quantitatively studied on onset pressure, frequency, maximum gap, flow rate, and medial surface motion (Murray, 2011).

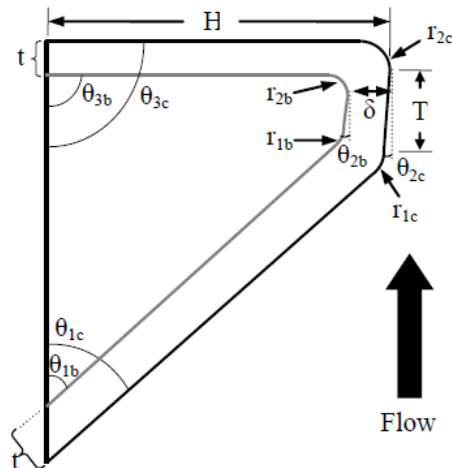


Figure 17. Simplified M5 vocal fold model in normal condition (Murray, 2011).

The introduction of Thyroplasty Type I, or Isshiki technique, which is the most commonly used surgical procedure to correct UVCP has been discussed in Section 1.3. The geometries of paralyzed vocal fold has not been concluded in details but are similar to those in Figure 7 in general. As a result, a curve

surface from cylindrical boundary are used to represent the paralyzed vocal fold in Figure 7(b). Seldom references on the deformation of vocal fold in synthetic rubber-like material has been found.

### 3.2 Methods

#### 3.2.1 Similarity theory

The M5 vocal fold geometry (Scherer et al., 2001) was used as the prototype of vocal fold in normal healthy conditions. The main size of M5 is shown in Figure 18. In order to model a paralyzed vocal fold, a cylinder with 16.5 mm in diameter was cut from the M5 vocal fold. The axis of this cylinder was perpendicular to the top surface of vocal fold. This cylinder was long enough to cut through the M5 vocal fold. The z coordinates of the center point on the top surface of this cylinder was 7.5 mm, half-length of vocal fold in z direction. The Schematic of prototype of the paralyzed vocal fold was shown in Figure 18.

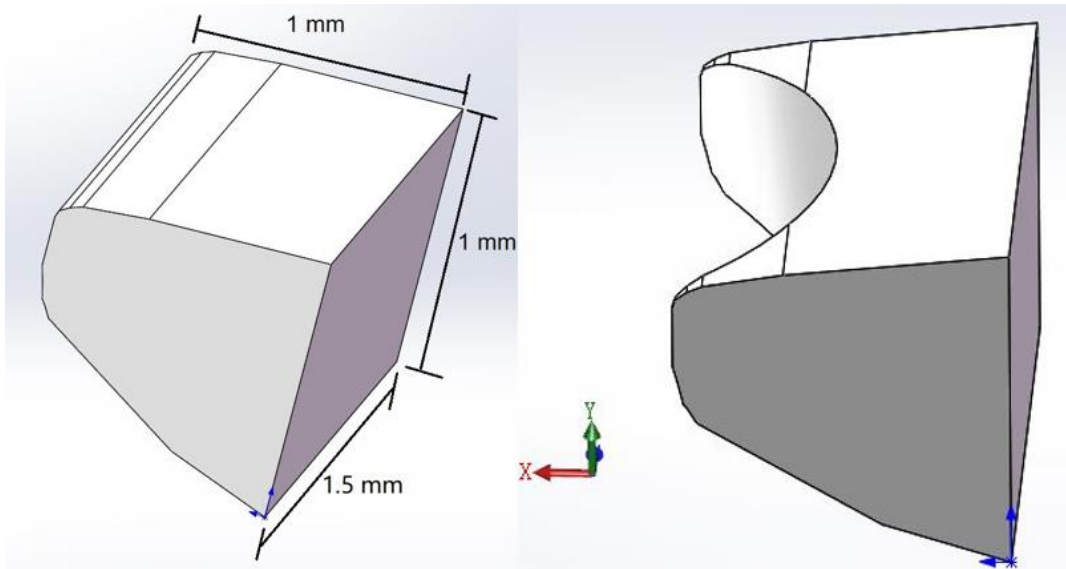


Figure 18. Three dimensional geometry of M5 and the paralyzed vocal fold used in this study.

Based on the primitive result of numerical simulation as shown in Figure 19, when the displacement of both legs of the Teflon was 1 mm, the corresponding force applied on Teflon was about 0.11 N. This level of force is too tiny to be measured in experiment. Moreover, the experimental error must be large if

this level of forces are directly measured. To make life easier and make the results accurate enough, similarity theory is necessary to be employed in this study in order to amplify the forces in experiments.

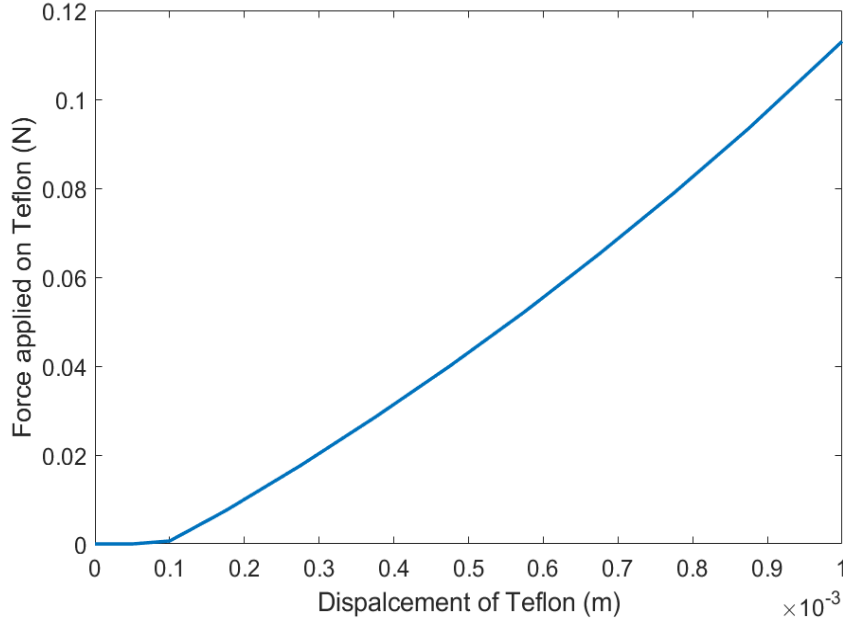


Figure 19. Primitive result of numerical simulation on the relationship between forces applied on Teflon and corresponding displacements.

Similarity theory has been applied for generalization of results in many different areas, especially in fluid mechanics. Under similar conditions, it is possible to gain important new insights without seeking solutions for problems in real sizes. In other words, researchers replace the investigation of a phenomenon in extreme size by the investigation of an analogous phenomenon with a proper size which is easier to be measured in laboratory conditions.

The length of prototype in anterior-posterior direction was 15 mm,  $\lambda = 4.6$  was chosen as scale factor as a start. As a result, the length of vocal fold model can be obtained by

$$\frac{L_m}{L_p} = \lambda \tag{3-1}$$

Where subscripts  $p$  and  $m$  related to the prototype and the model respectively. With Hooke's law:

$$E = \frac{\sigma}{\varepsilon} = \frac{F/A}{\Delta L/L} = \frac{F \cdot L}{\Delta L \cdot A} \quad (3-2)$$

Where  $E$  is the Young's modulus,  $F$  is the force applied on an object under tension or compression,  $A$  is the actual cross-sectional area perpendicular to the applied force,  $\Delta L$  is the change in length,  $L$  is the original length of the object.

In prototype experiments,

$$E_p = \frac{\sigma_p}{\varepsilon_p} = \frac{F_p/A_p}{\Delta L_p/L_p} = \frac{F_p \cdot L_p}{\Delta L_p \cdot A_p} \quad (3-3)$$

In model experiments,

$$E_m = \frac{\sigma_m}{\varepsilon_m} = \frac{F_m/A_m}{\Delta L_m/L_m} = \frac{F_m \cdot L_m}{\Delta L_m \cdot A_m} \quad (3-4)$$

Equation (2-5) divided by (2-4) when Young's modulus was equal due to same material,

$$\frac{E_m}{E_p} = \frac{\frac{F_m \cdot L_m}{\Delta L_m \cdot A_m}}{\frac{F_p \cdot L_p}{\Delta L_p \cdot A_p}} = \frac{F_m}{F_p} \cdot \frac{L_m}{L_p} \cdot \frac{\Delta L_p}{\Delta L_m} \cdot \frac{A_p}{A_m} = 1 \quad (3-5)$$

The ratio of external forces in prototype to forces in model can be obtained by

$$\frac{F_m}{F_p} = \lambda^2 \quad (3-6)$$

In figure 18, the prototype of vocal fold is cut by a cylinder resulting in a gap which is approximate 5 mm. If linear relationship between applied forces and displacements was assumed as a start, when the displacement of the model of paralyzed vocal fold is 18.4 mm, which is 4.6 times of 4 mm in prototype, the force applied on the model of paralyzed vocal fold can be obtained by

$$F_m = 0.11(N) \cdot 4 \cdot \lambda^2 = 9.6(N) \quad (3-7)$$

The amplitude of this force applied in model is proper to be measured in laboratory conditions.

### 3.2.2 Generation of synthetic vocal fold

In step 1, a three dimensional prototype of paralyzed vocal fold was made using SolidWorks as shown in Figure 18. Geometry in details is described in Section 3.2.1. In step 2, in order to cast the solid body of paralyzed vocal fold model, a negative mode of this model was made in Figure 20. The negative mode of paralyzed vocal fold model was separated into two individual parts in order to obtain the solid body as a whole after the solutions were cured (Figure 21). In step 3, the separated negative modes of vocal fold model were printed using three dimensional printer at Biomedical Engineering Lab at the University of Maine at Orono as shown in Figure 22. In step 4, three solutions with volume ratio of 1:1:1 were mixed together in a container and stirred well. Afterwards, the mixed solution was injected into the assembled negative modes. The gap between two negative modes through which the solutions can flow should be sealed. In step 5, the synthetic solid body of paralyzed vocal fold model can be generated after 24 hours at room temperature. The generation time can be shorten at higher temperature. Figure 23 shows the prototype of paralyzed vocal fold (right) and the model (left) used in this study which is 4.6 times of prototype.

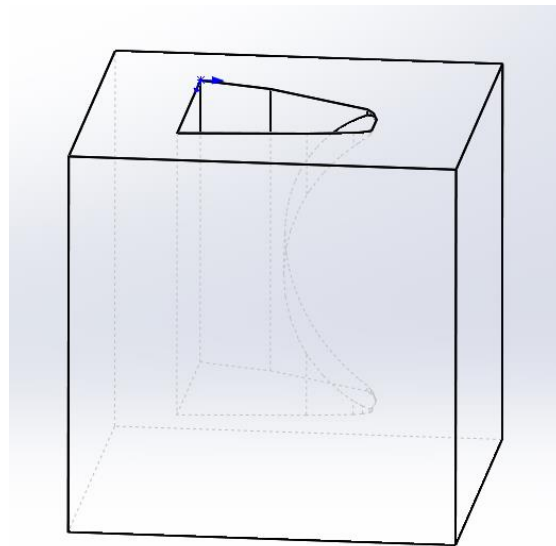


Figure 20. Negative mode of the paralyzed vocal fold model.

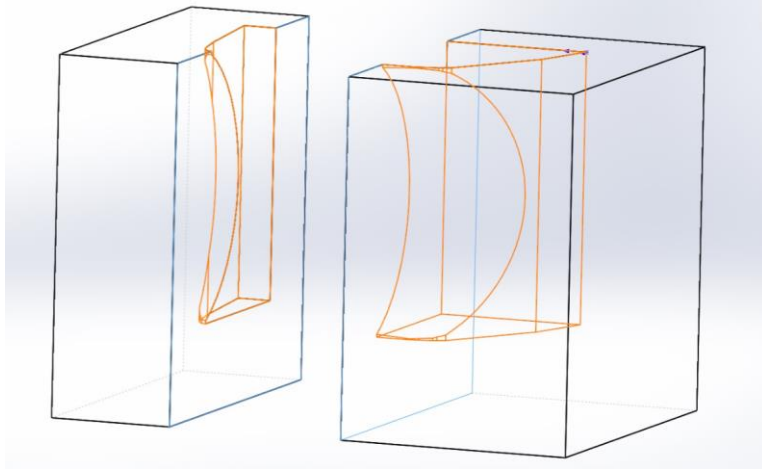


Figure 21. Separated negative modes of the paralyzed vocal fold model.

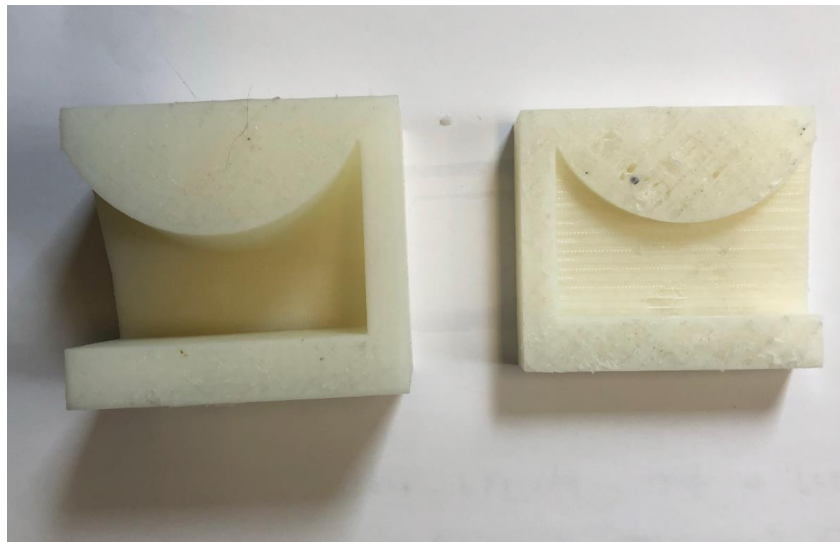


Figure 22. 3D printed negative modes of the model of paralyzed vocal fold.

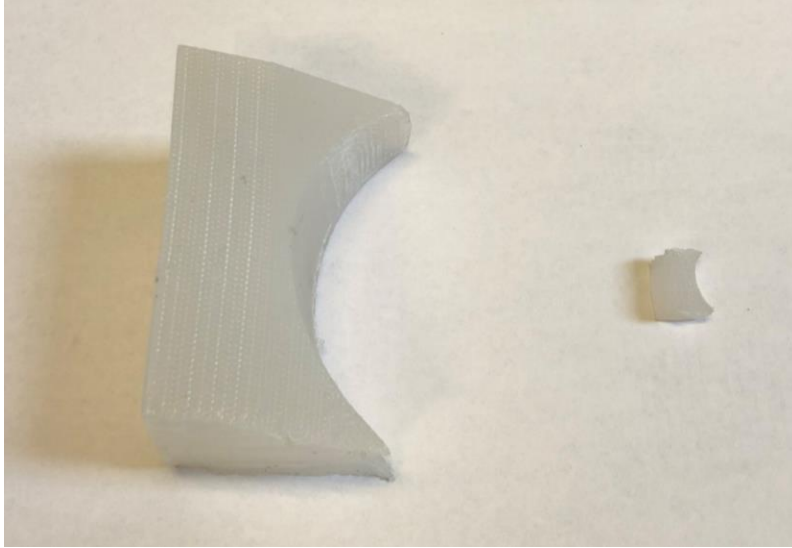


Figure 23. The prototype of paralyzed vocal fold (right) and the model (left) used in this study.

### **3.2.3 Fabrication of testing platform**

In order to apply different forces on two legs of Teflon patch, a new device has been fabricated as shown in Figure 24 and Figure 25. In Figure 24 and 25, the two legs of Teflon patch are fixed on the transparent thick plate except vertical movement. Two parallel grooves in this thick plate make the legs of Teflon to pass through. Under different external forces, the legs of Teflon can move only in vertical direction. Two small vertical thick transparent plates in Figure 24 and 25 are used to fix left and right boundaries of the paralyzed vocal fold model. Two long aluminum sticks support the paralyzed synthetic vocal fold model in vertical direction. Four legs made of wood support the whole platform.



Figure 24. Front view of the test platform.

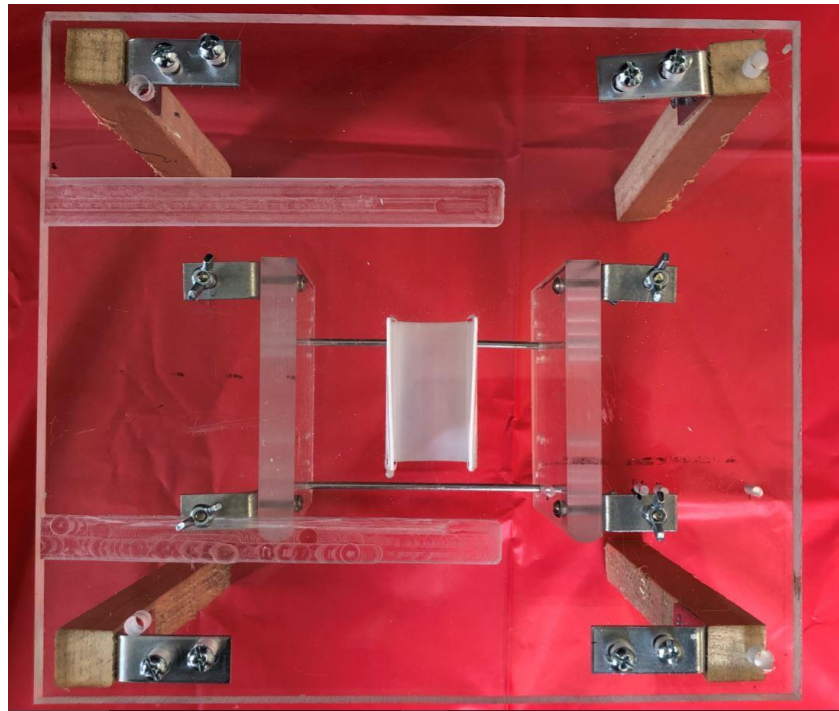


Figure 25. Vertical view of the test platform.

In order to support different weights on the two legs of Teflon, two cubes offering horizontal surfaces were fixed on legs of Teflon in Figure 26 and 27. The depth of two slots were same in order to make two surfaces in same height. The length of the Teflon patch used in experiment was 100 mm. The

paralyzed synthetic vocal fold and the fabricated structure were assembled in Figure 28 and 29. Under different loadings, the bottom part of Teflon will push the paralyzed vocal fold only in vertical direction.



Figure 26. Front view of two plates fixed on Teflon.

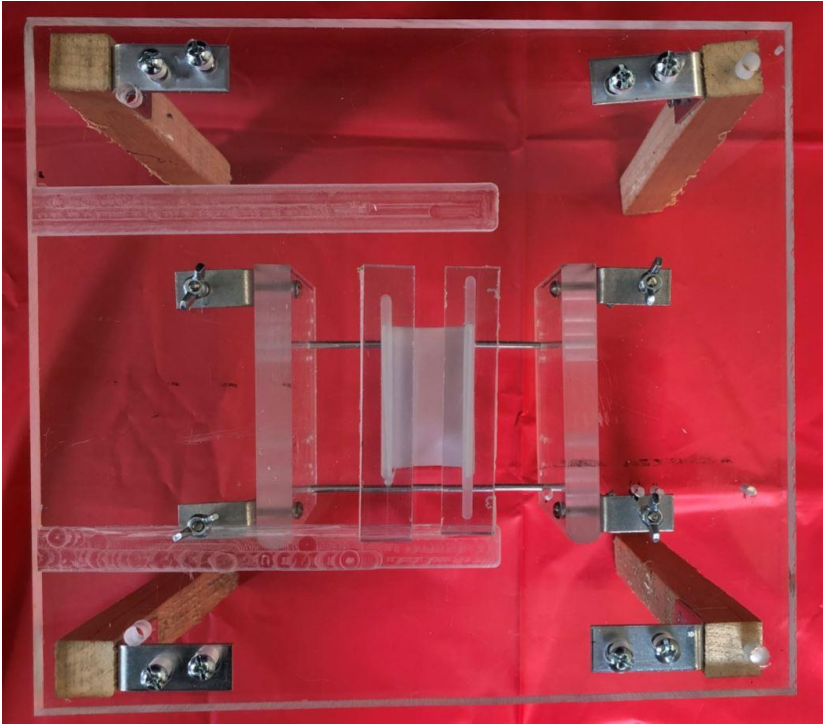


Figure 27. Vertical view of two plates fixed on Teflon.

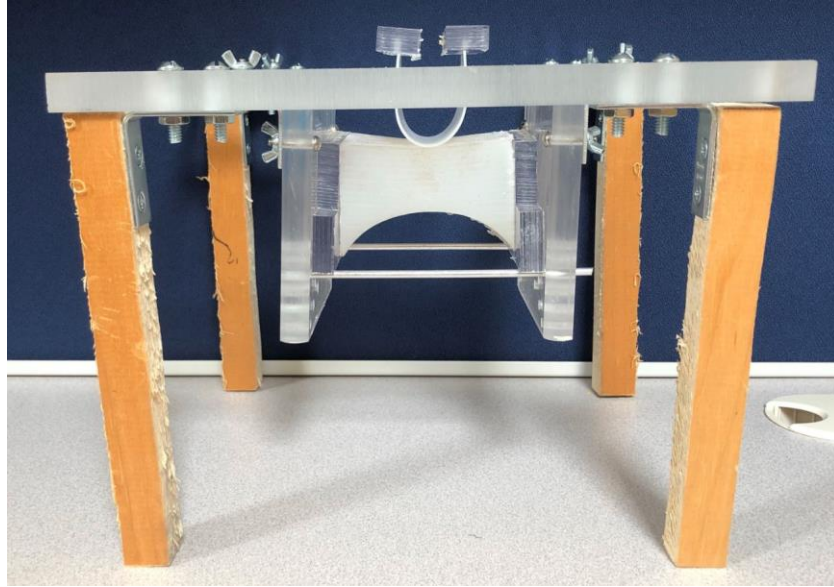


Figure 28. Front view of the testing platform and paralyzed vocal fold model without loading.

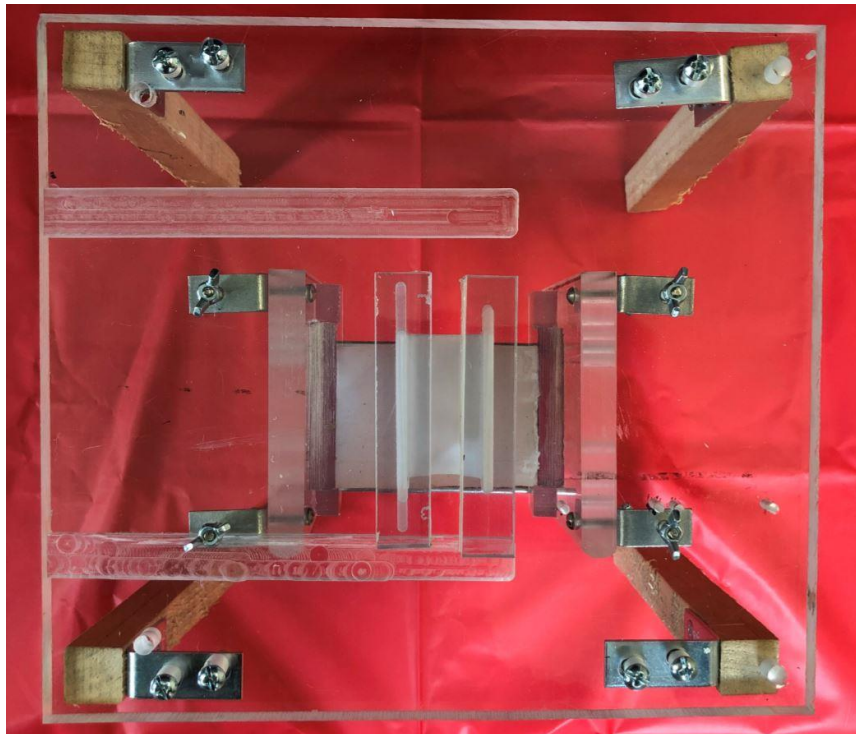


Figure 29. Vertical view of the testing platform and paralyzed vocal fold model without loading.

### 3.2.4 Displacement measurement

The Doppler technique was employed to measure the displacements of several marker points on the curve surface of the paralyzed vocal fold model in this study. Laser with fixed wavelength is transmitted by transmitter and reflected by objects. The time of laser travelling has a linear relationship with the distance between transmitter and an object. For this device, the time of laser travelling has a linear effect on the voltage received. This device (shown in Figure 30) and Laboratory Virtual Instrument Engineering Workbench (LabVIEW) were obtained from Biomedical Engineering Lab at the University of Maine at Orono. Calibration is necessary before measurement.



Figure 30. Doppler displacement device by Baumer

This technique can only measure the distance of one point on the curve surface of the model of paralyzed vocal fold. There are 97 marker points on this curve surface shown in Figure 31. During the experiment, laser transmitted by Doppler device traced the vertical position of every marker point one by one. In other words, when the curve surface was deformed by external force applied on Teflon, 97 distances were measured one by one when this system became static. Figure 31 shows the laser transmitted by Doppler device is pointing one marker point on the curve surface.

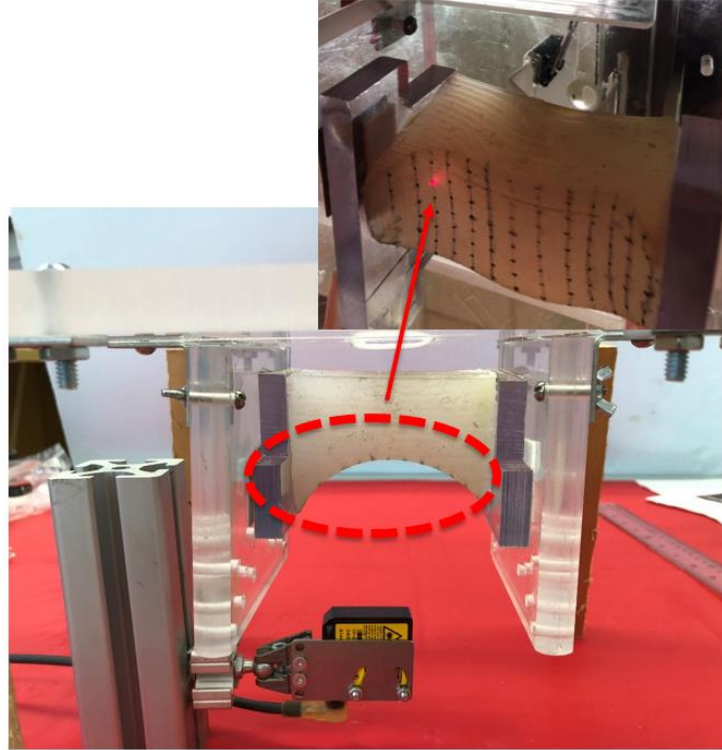


Figure 31. The position of Doppler device and marker points on the curve surface of paralyzed vocal fold model.

### 3.3 Results and discussion

In order to find the relationship between the deformation of curve surface on synthetic vocal fold and the displacements of different legs of Teflon, and the forces applied on two Teflon legs, 14 experiments involved in 5 groups were implemented in this study including the undeformed configuration (Figure 32). Table 3 lists the displacements of different legs (Leg 1 and Leg 2) in details. When the displacement of Leg 1 was fixed at 0 mm, the corresponding displacements of Leg 2 were 0 mm (unloading), 5.2 mm, 10.2 mm and 15.2 mm. The condition of displacement of Leg 2 at about 20.0 mm was skipped. In surgery, differences of displacements between Leg 1 and 2 over 15.0 mm were not considered due to instability. Moreover, due to approximately bilateral symmetry of this paralyzed vocal fold, the configuration where displacement of Leg 1 was approximate 5.0 mm and the displacement of Leg 2 was 0 mm (L5.0R0) was almost same with the configuration where displacement of Leg 1 was 0 mm and

displacement of Leg 2 was 5 mm (L0R5.0). As a result, the condition of L5.0R0 was skipped. When the displacement of Leg 1 was approximate 5.0 mm (6.0 mm in fact), the displacements of Leg 2 were 6.0 mm, 9.2 mm, 15.0 mm and 20.2 mm respectively, and so on. In the following sections, L0R0 stands for the configuration where the displacement of Leg 1 (Left leg) was 0 mm and the displacement of Leg 2 (Right leg) was 0 mm for simplicity.

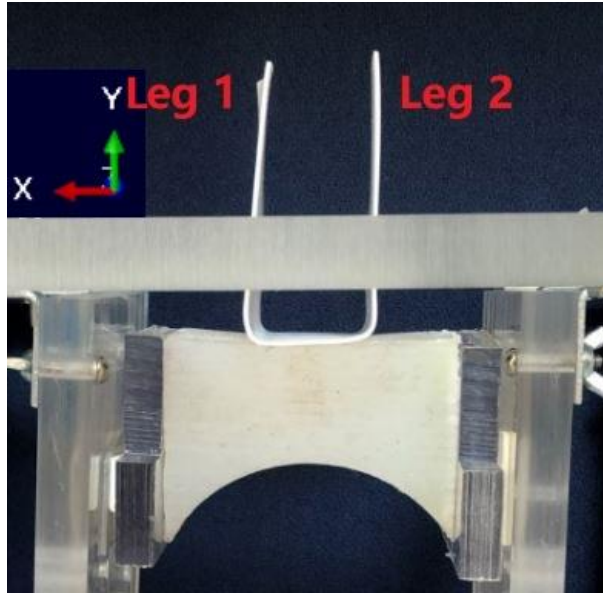


Figure 32. Unloading configuration of the paralyzed vocal fold model and Teflon patch.

Table 3. Displacements of Leg 1 and 2 and the corresponding name for 14 experiments.

Displacement of Leg 1 (mm)	Displacement of Leg 2 (mm)	Name
0.0	0.0	Undeformation (L0R0)
	5.2	L0R5.2
	10.2	L0R10.2
	15.2	L0R15.2
6.0	6.0	L6.0R6.0
	9.2	L6.0R9.2
	15.0	L6.0R15.0
	20.2	L6.0R20.0
10.0	10.0	L10.0R10.0
	15.0	L10.0R15.0

	20.2	L10.0R20.0
15.0	15.0	L15.0R15.0
	20.0	L15.0R20.0
20.0	20.0	L20.0R20.0

Figure 33 shows the initial y coordinates of 97 marker points on the curve surface of synthetic vocal fold model under the condition that no external force applied on the two legs of Teflon but initial contact between Teflon and synthetic vocal fold occurred. From Figure 33, there are 6 points in  $x=-30$ ,  $x=-25$ ,  $x=25$ , and  $x=30$  column. There are 7 points when  $x=-20$ ,  $x=-15$ ,  $x=15$ , and  $x=20$ . There are 9 points when  $x=-10$ ,  $x=-5$ ,  $x=0$ ,  $x=5$ , and  $x=10$ . It should be noted that the marker points on the curve surface can have a sort of movements in horizontal direction ( $x$ - $z$  plane in Figure 33) when the applied external forces were increased gradually. However, the horizontal displacements of marker points in  $x$ - $z$  plane were tiny compared to displacements in vertical  $y$  direction. Moreover, the gap between two vocal folds resulting from the displacements of paralyzed vocal fold in  $y$  direction was focused in this study rather than the displacements in  $x$ - $z$  plane. As a result, the horizontal displacements were all ignored.

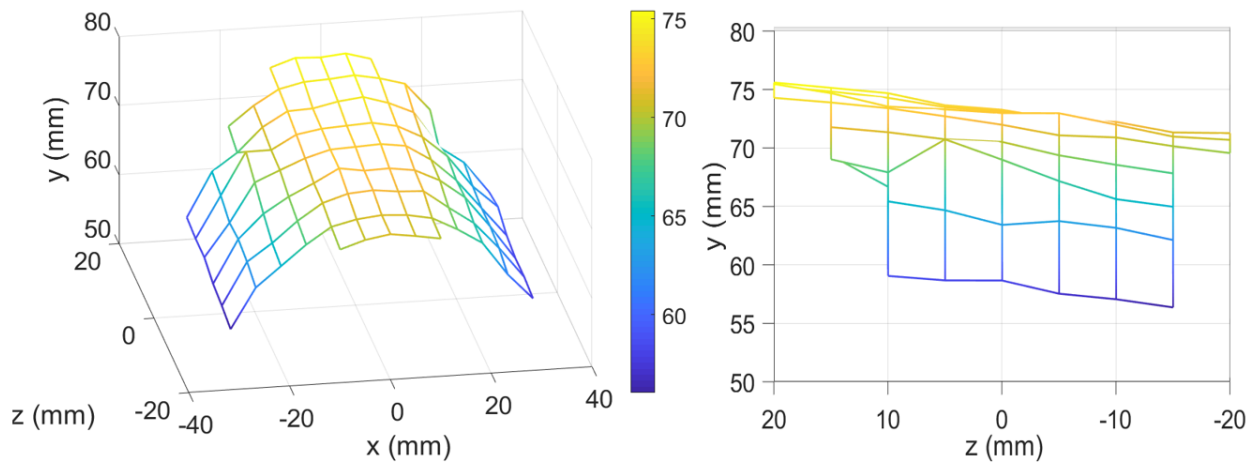


Figure 33. Three dimensional coordinates and lateral view of 97 marker points on the undeformed curve surface of vocal fold.

Almost all marker points in same  $x$  coordinates had coincident vertical  $y$  coordinates in Figure 33(a) except one point which was  $-20$  in  $x$  coordinates and  $10$  in  $z$  direction. This should be a mistake from the

Doppler displacement measurement. During this experiment, the range of data from Doppler device should be always focused in order to be checked as valid values. Figure 33(b) showed the y coordinates of marker points on curve surface had nearly linear relationship with z coordinates suggesting inclination of this curve surface. This is due to the axis of cylinder used to cut the M5 vocal fold is perpendicular to the top surface of vocal fold in Figure 18.

Figure 34 shows the y coordinates of every point on the curve surface in L0L0R5.2, L0R10.2, and L0R15.2 configurations when Leg 1 is kept at 0. It is shown that the curve surface moves downward along with the right leg of Teflon. Moreover, when the differences of displacements between two legs are up to 10 or 15 mm, the curve surface always shows nearly bilateral symmetry. The bilateral symmetry in this group is also captured by camera during experiments in Figure 35. Similar results can also be found in other groups of experiments when the left leg was kept at 6.0, 10.0, and 15.0 mm. From Figure 35, the asymmetry of two legs of Teflon do not have an influence on the symmetry of vocal fold model. Figure 35 also shows the external forces applied on the right leg of Teflon when displacements of right leg are 5.2, 10.2, and 15.2 mm respectively.

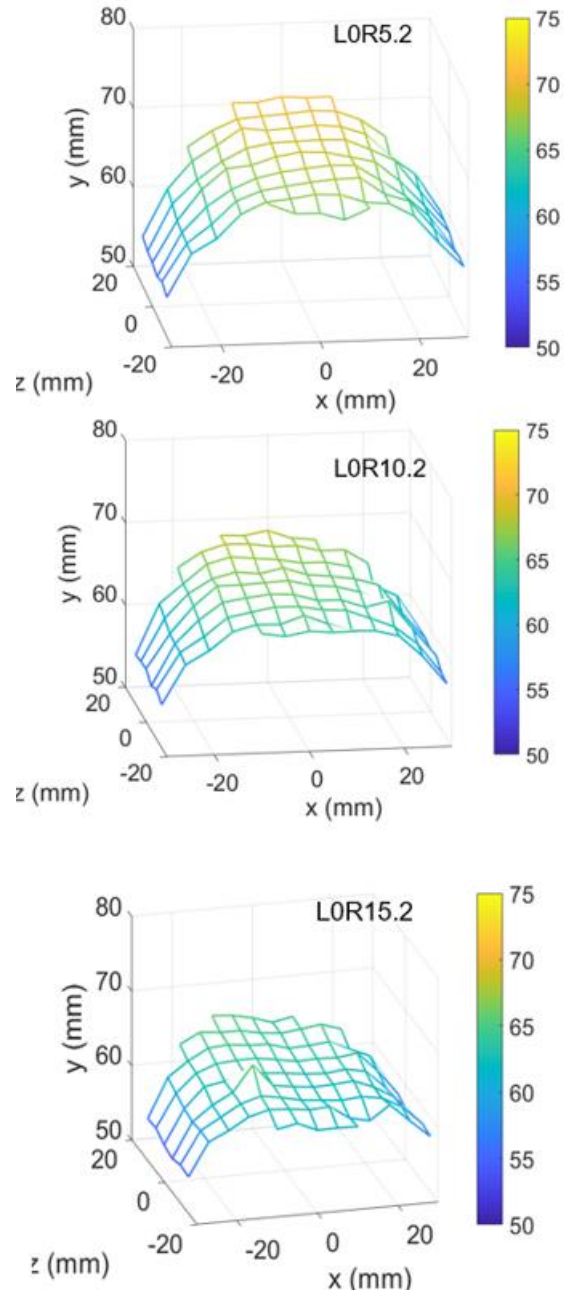


Figure 34. The y coordinates of every point on the curve surface in L0L0R5.2, L0R10.2, and L0R15.2 configurations.

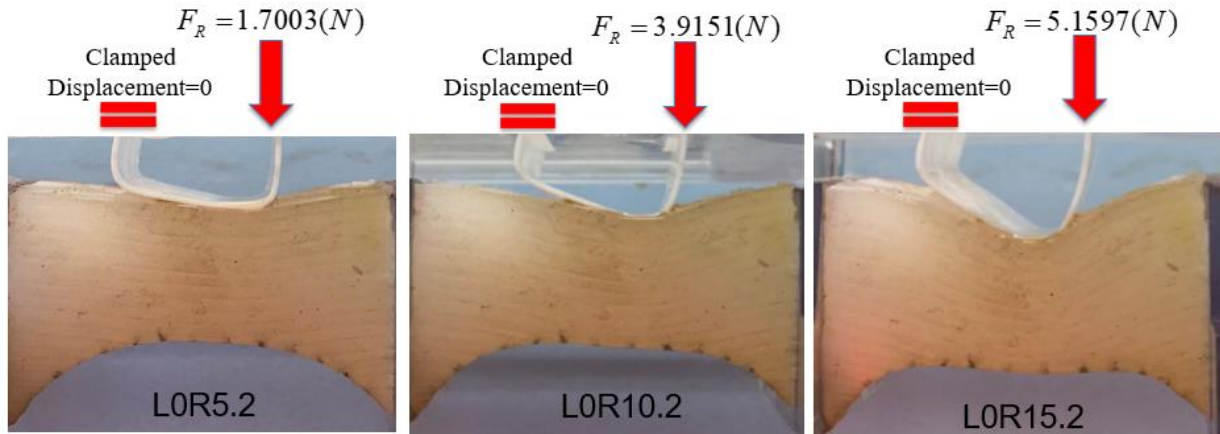


Figure 35. The external forces applied on Leg 2 when displacements of Leg 2 were 5.2, 10.2, 15.2 mm under the condition of displacement of Leg 1 was 0 mm.

In the next group of experiments when the displacement of Leg 1 was 6.0 mm, the displacements of Leg 2 were increased from 6.0 to 20.2 mm in Table 3. Figure 36 indicates the different positions of curve surfaces represented by 97 marker points on synthetic vocal fold under different loadings. With the Leg 2 of Teflon moving downward, the marker points in  $x=10.0$  mm column became the lowest points in the middle region of this curve surface at L6.0R9.2 configuration. Then at next configuration L6.0R15.0, the points with  $x=5$ mm became the lowest points. The marker points in  $x=0$  mm column became the lowest points at the last configuration at L6.0R20.0. The movement of lowest points is also shown in Figure 37 during experiments.

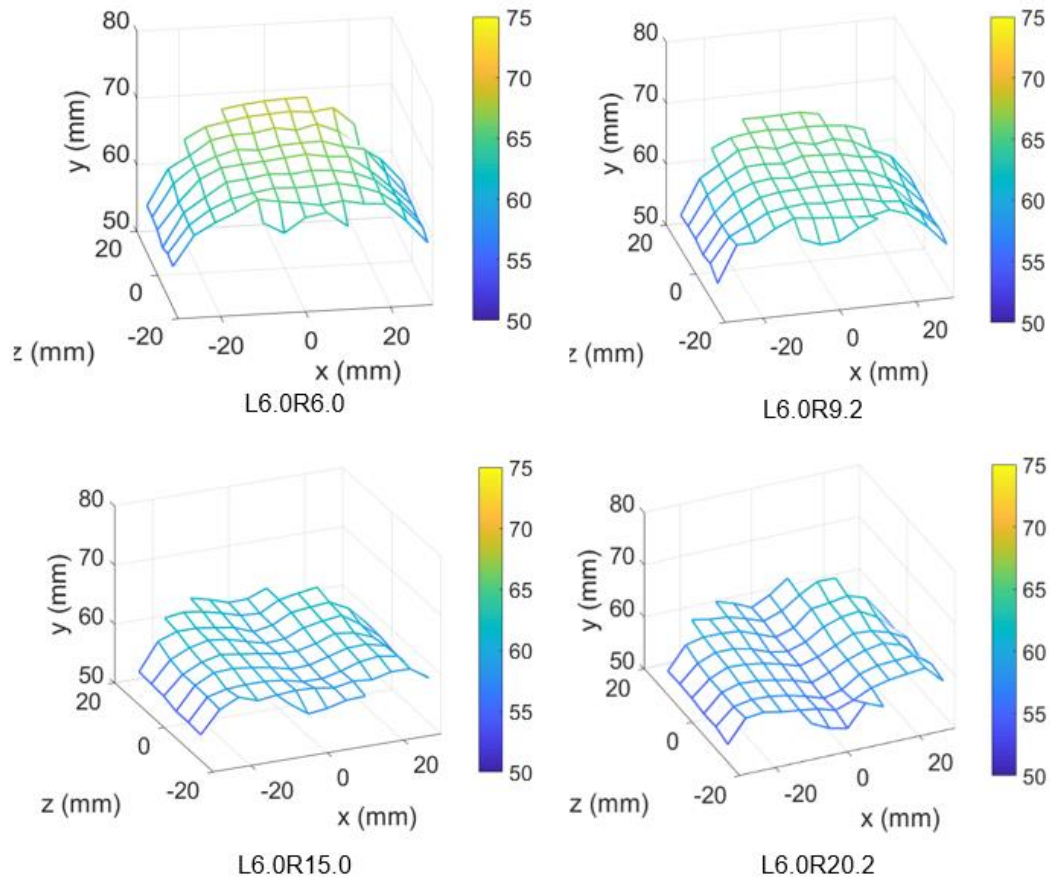


Figure 36. Different positions of the curve surfaces at L6.0R6.0, L6.0R9.2, L6.0R15.0, L6.0R20.2 configurations.

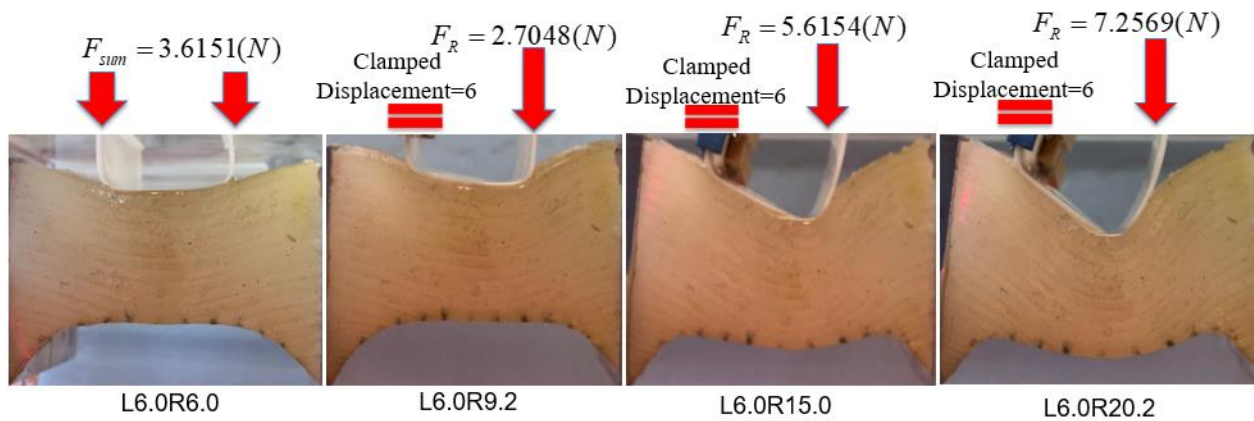


Figure 37. The external forces applied on Leg 2 when displacements of Leg 2 were 6.0, 9.2, 15.0, 20.2mm under the condition of displacement of Leg 1 was 6.0 mm.

When the displacement of Leg 1 increased to 10.0 mm in next group of experiments, Figure 38 shows the spatial locations of L10.0R10.0, L10.0R15.0, and L10.0R20.0 configurations. This group of experiments also shows the lowest points in the middle region moves from  $x=5.0$  mm to  $x=0$  mm. Figure 38 indicates the necessary forces applied on Leg 2 in experiments.

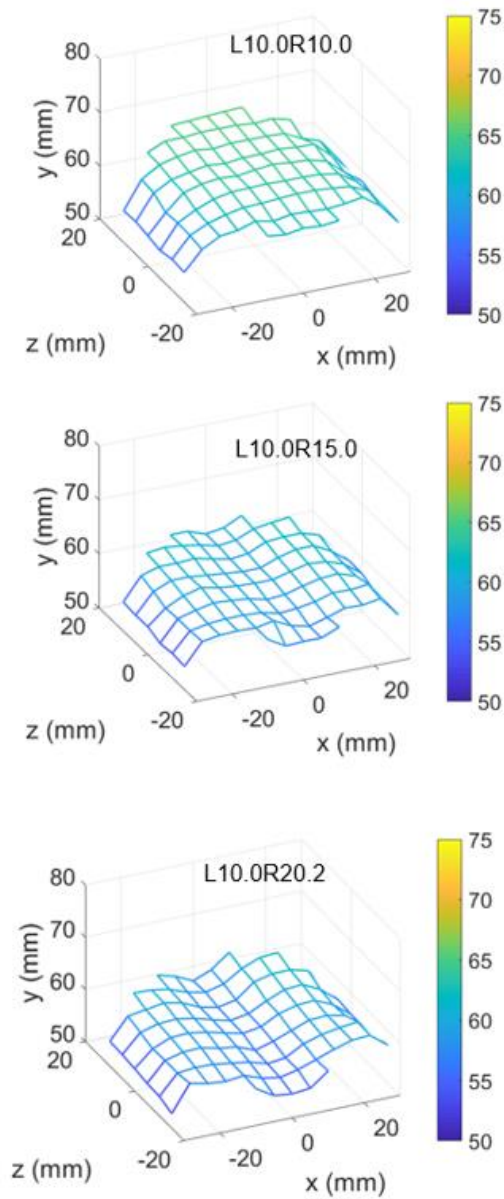


Figure 38. The y coordinates of L10.0R10.0, L10.0R15.0, and L10.0R20.0 curve surfaces.

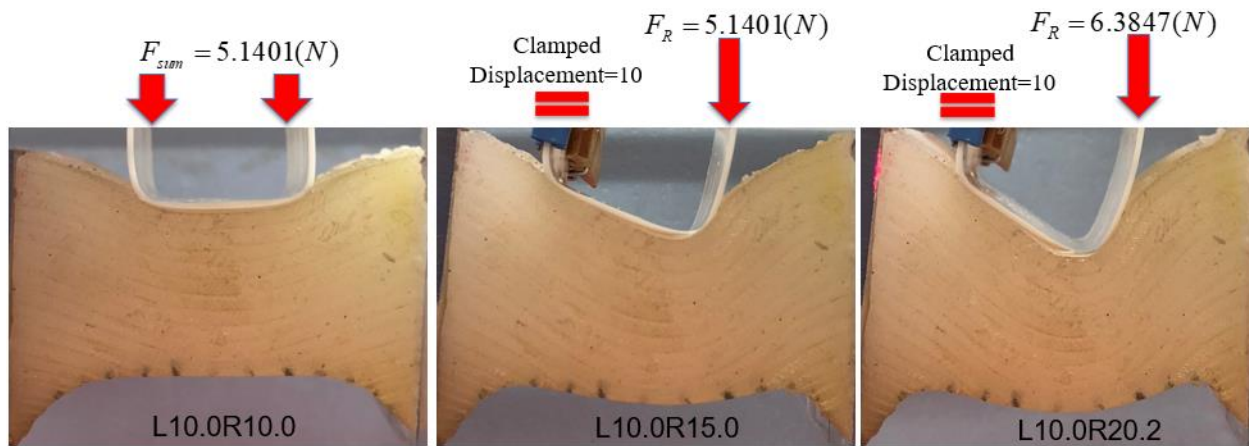


Figure 39. The external forces applied on Leg 2 when displacements of Leg 2 were 10.0, 15.0, 20.2 mm under the condition of displacement of Leg 1 was 10.0 mm.

In the fourth group of experiments where displacement of Leg 1 was kept at 15.0 mm, the displacements of Leg 2 increased from 15.0 to 20.0 mm. Figure 40 shows the spatial locations of these two curve surfaces on the vocal fold at L15.0R15.0 and L15.0R20.0 configurations. Figure 41 indicates the external forces applied on Leg 2 of Teflon when displacements of Leg 1 were 15.0 and 20.0 mm. Figure 42 shows the spatial location of the curve surfaces on the vocal fold at L20.0R20.0 configurations.

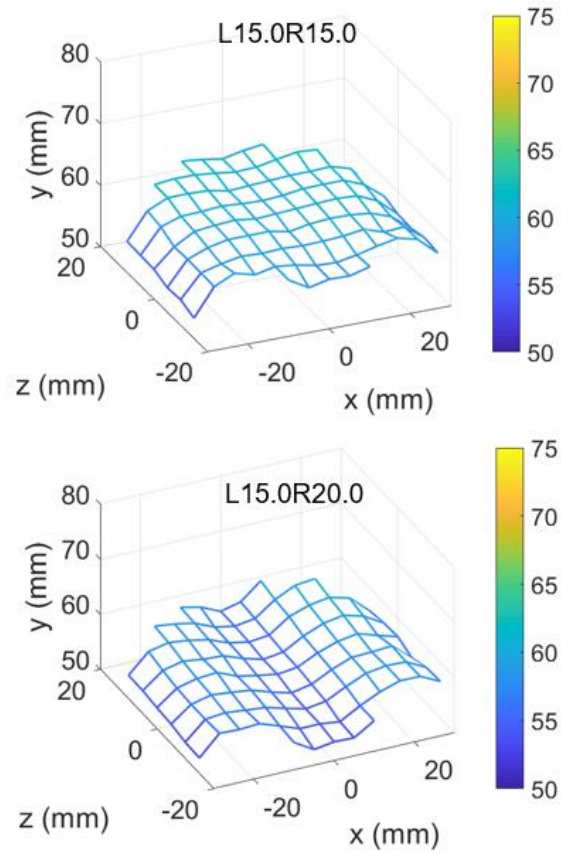


Figure 40. Spatial locations of the curve surfaces when Leg 2 moved from 15.0 to 20.0 mm and Leg 1 was kept at 15.0 mm.

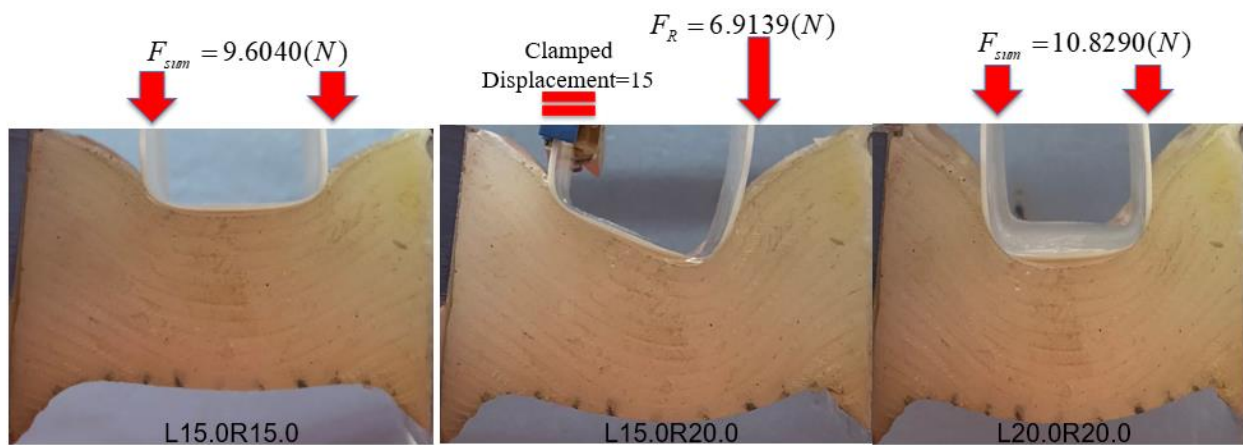


Figure 41. External forces applied on legs for displacements of Leg 1 at 15.0 and 20.0 mm configurations.

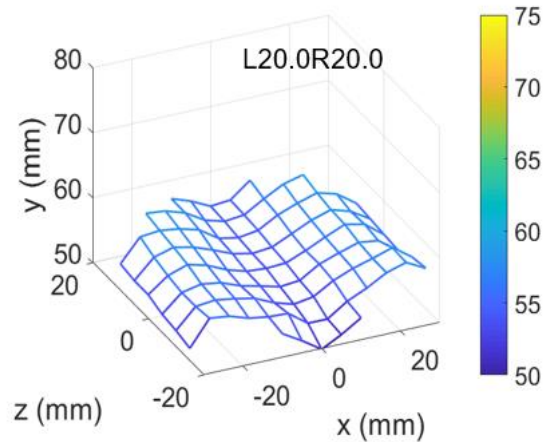


Figure 42. Y coordinates of marker points on the curve surface of L20.0R20.0 configuration.

### 3.4 Analysis

#### 3.4.1 Necessary forces on the prototype of paralyzed vocal fold

Based on the similarity theory in Section 3.2.1 where the amplification ratio  $\lambda$  of the model of the paralyzed vocal fold to the prototype was 4.6, the necessary forces on prototype can be obtained when the external forces applied on model were divided by  $\lambda^2$ . Table 4 concludes the applied forces for the paralyzed vocal fold model in each configuration and the corresponding forces for the prototype of vocal fold. From Table 4 below, the maximum necessary force applied on prototype of paralyzed vocal fold is over 0.5 N.

Table 4. The forces applied on paralyzed vocal fold model in experiments and the necessary forces for prototype in each configuration.

Leg 1 Displacement (mm)	Leg 2 Displacement (mm)	Forces on model (N)	Necessary Forces on prototype (N)
0	0	0	0
	5.2	1.7003	0.0804
	10.2	3.9151	0.1850
	15.2	5.1597	0.2438
6.0	6.0	3.9151	0.1850
	9.2	2.7048	0.1278

	15.0	5.6154	0.2654
	20.2	7.2569	0.3430
10.0	10.0	5.1401	0.2429
	15.0	5.1401	0.2429
	20.2	6.3847	0.3017
15.0	15.0	9.6040	0.4539
	20.0	6.9139	0.3267
20.0	20.0	10.8290	0.5118

### 3.4.2 Approximate bilateral symmetry

It is found that the paralyzed synthetic vocal fold model indicates bilateral symmetry for almost all configurations including the maximum differences between displacements of Leg 1 and 2 in Figure 43 were reached. When the displacement of Leg 2 was 15.2 mm and displacement of Leg 1 was 0 mm (LOR15.2), difference of displacements between Leg 1 and 2 was up to 15.2 mm, the curve surface of synthetic vocal fold still shows bilateral symmetry. Based on these four conditions below in Figure 43, Leg 2 of Teflon would contact the synthetic vocal fold model at the middle area approximately when maximum differences are reached. And from Figure 34, 36, 38, and 40 the minimum y coordinates of marker points in the middle region would gradually slide from one side to middle region. As a result, when this adjustable implant is employed in surgery, asymmetry of gap between two vocal folds resulting from the differences between displacements of Leg 1 and 2 can be ignored.

Moreover, the deformation of paralyzed vocal fold is largest at the center symmetric line in Figure 43.

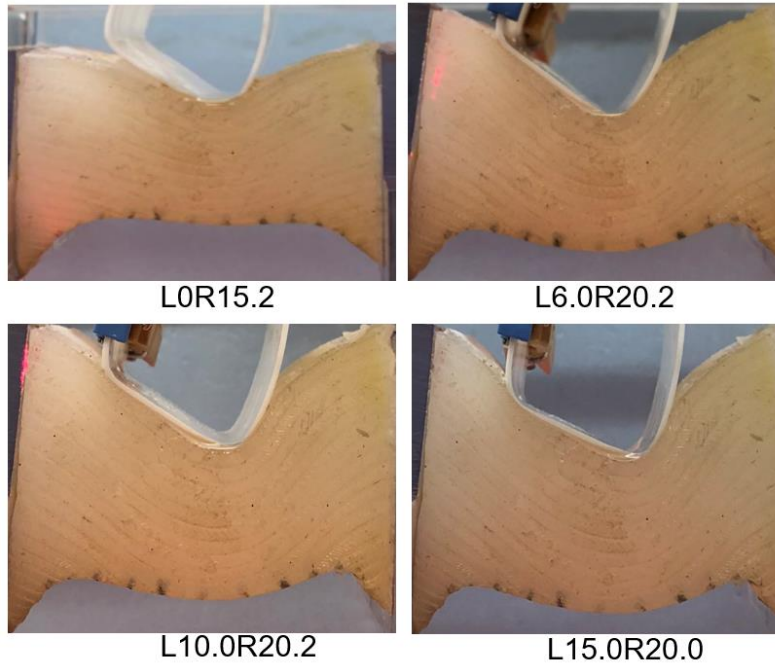


Figure 43. Behavior of the curve surfaces when maximum difference between two legs were reached.

### 3.4.3 Deformation

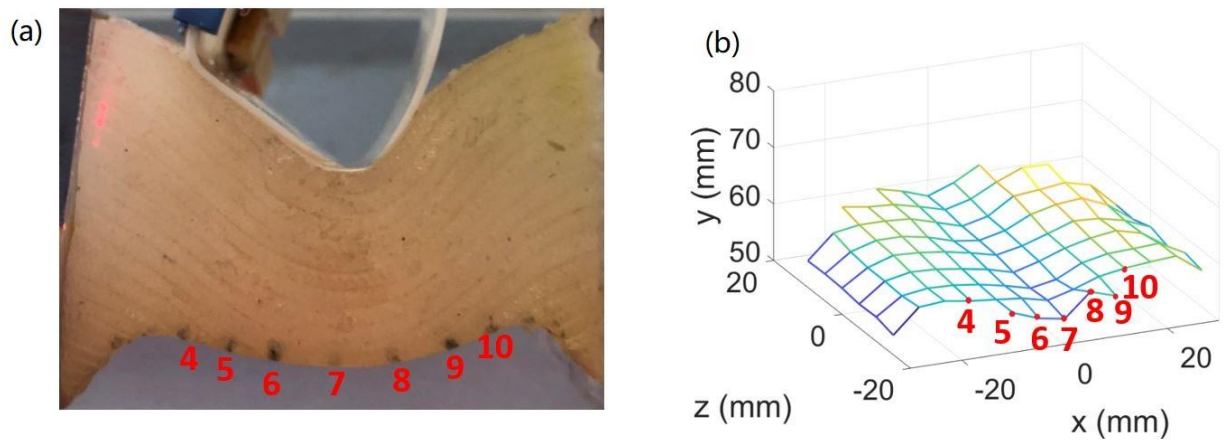


Figure 44. Line numbers on the curve surface (a) and x coordinates of numbered line (b) for L6.0R20.2 configuration.

In order to trace the deformation of the curve surface in each configuration, every line is numbered from 1 to 13. Take the configuration L6.0R20.2 for example. Figure 44 (a) shows the line numbers from 4 to 10 in the center region of curve surface. Figure 44(b) shows the x coordinates of the numbered line.

The difference of x coordinates of every two adjacent line is 5 mm. The x coordinate of the center line 7 is 0. In this study, three numbered line 4, 7, and 10 are selected to describe the deformation of the curve surface based on the displacements of these numbered lines. From Figure 43(b) there are 7 points in line 4 and 10, and 9 points in line 7. In the following section, the averaged y coordinates of line 4, 7 and 10 are used to indicate the y positions of line 4, 7 and 10, respectively.

For symmetric configurations L6.0R6.0, L10.0R10.0, L15.0R15.0, and L20.0R20.0, the relationships between force and displacement of legs of Teflon and displacements of line 4, 7, and 10 are investigated. In Figure 45, yellow points are experimental data of force on two legs and displacement of legs. Linear fitting line (yellow solid line) is used to demonstrate the relationship. Orange, blue, and grey points stand for the experiment data of point 4, 7, and 10, respectively. Dash-point lines in corresponding color are employed to suggest the linear force-displacement relationships of each point. For each group of data, the relationships are all close to linear with current data. Among these three points, the deformation of point 7 is largest which is close to the displacement of legs of Teflon. The fitting line of point 7 is close to the fitting line of legs suggesting the displacement of point 7 is similar to displacement of legs.

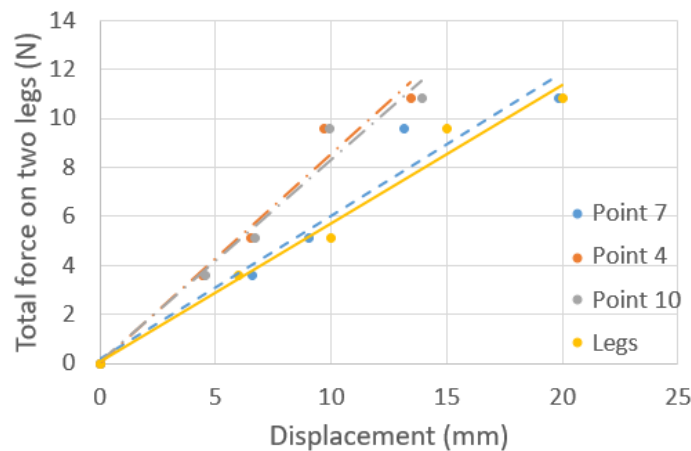


Figure 45. Relationship between force on legs and displacements of legs, point 4, 7, and 10 in symmetric configurations.

Figure 46 shows the relationship between force on Leg 2 and displacement of Leg 2 when displacements of Leg 1 is 0, 6, and 10, respectively. Linear fitting lines are used to demonstrate the relationships. When displacements of Leg 1 are different, these three lines are slightly different suggesting the displacement of one leg is affected by the displacement of the other. With larger displacement on leg 1, the force needed to generate the same displacement in leg 2 is less. It is because the displacement on leg 1 will result in some level of pre-deformation at the position of leg 2 before the force on leg 2 is applied.

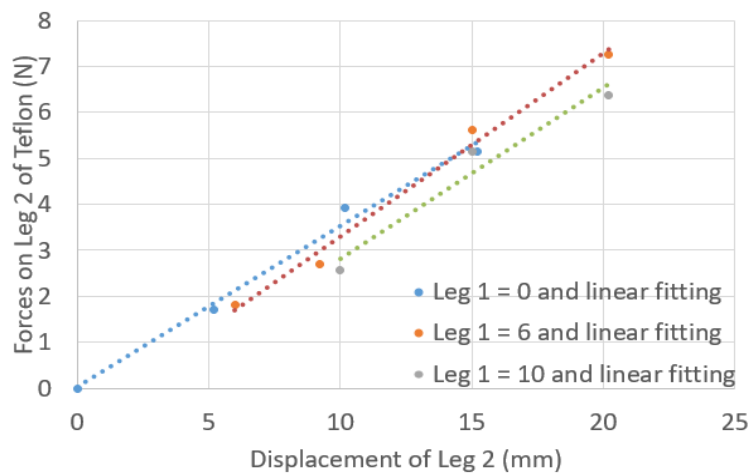


Figure 46. Relationship between force on Leg 2 and displacement of Leg 2 under different displacements of Leg 1.

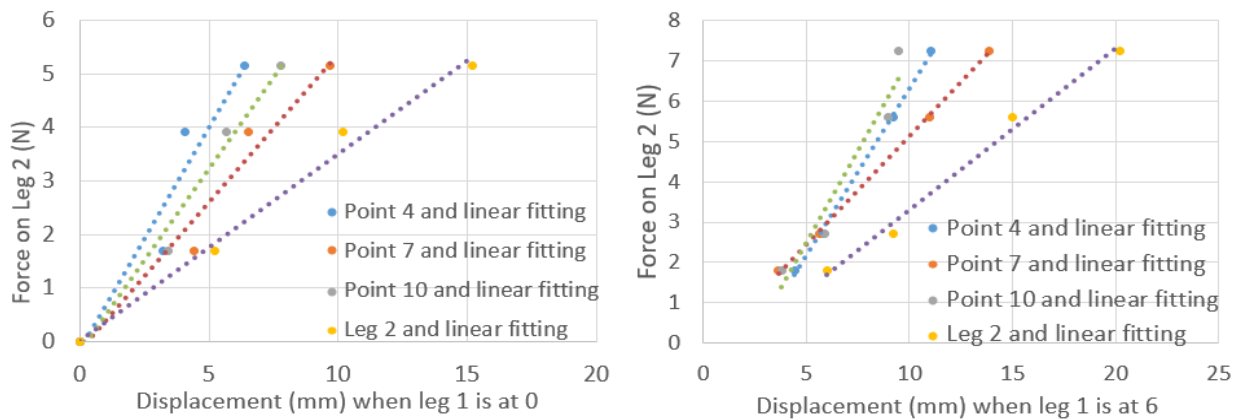


Figure 47. Relationship between displacement of Leg 2, different points and force on Leg 2 when Leg 1 is at 0 and 6.

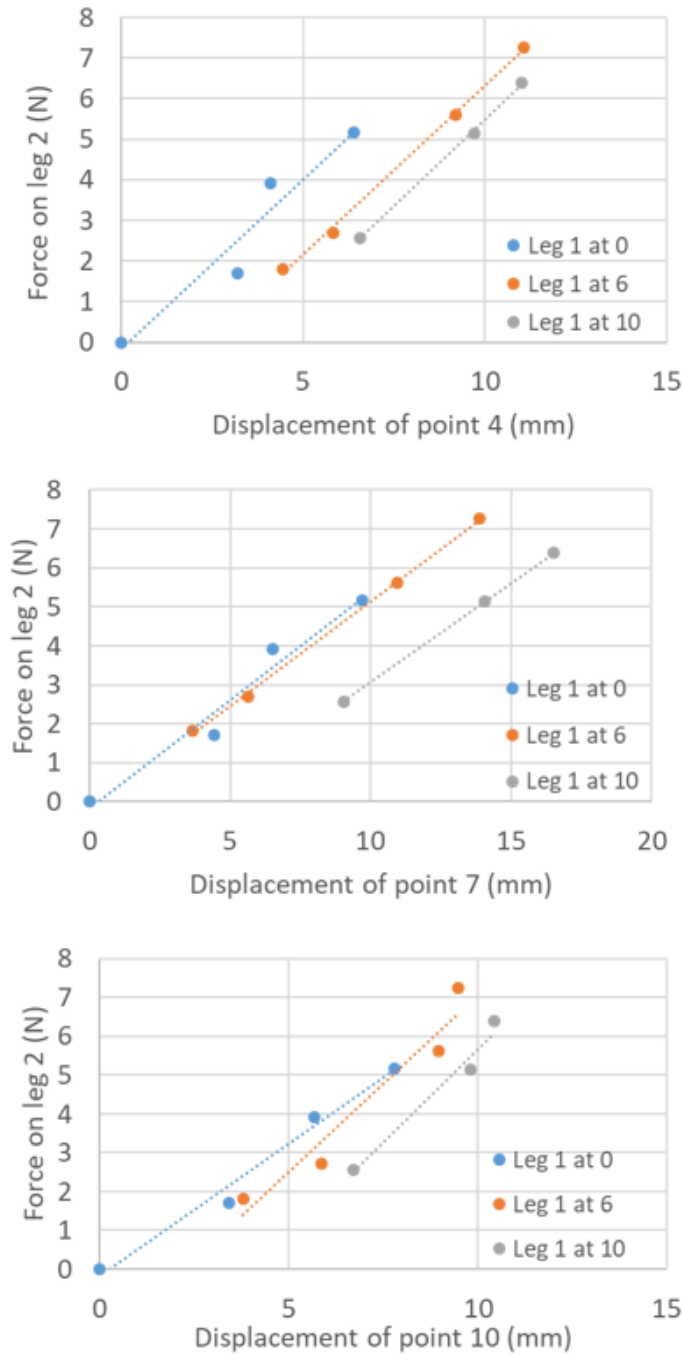


Figure 48. Relationship between displacements of different points and Force on Leg 2 when displacements of Leg 1 are different.

From Figure 47, when displacement of Leg 1 is at 0 or 6, there is a nearly linear relationship between displacements of Leg 2 and forces on Leg 2. Moreover, the relationships between displacements of different points (4, 7, and 10) and forces on Leg 2 are close to linear based on current data. Figure 48

shows the relationship between displacements of different points and force on Leg 2 when displacements of Leg 1 are different. For each group of data, the relationship is close to linear between displacements of points and force on Leg 2. Moreover, with larger displacement on leg 1, the force needed to generate the same displacement of all points 4, 7, and 10 is less.

## CHAPTER 4

### NUMERICAL SIMULATION

#### 4.1 Introduction

In this chapter, a computational method named Finite Element Method (FEM) involving contact was used to study the deformations of curve surface on the paralyzed synthetic vocal fold model when contacted with the Teflon patch where nonlinearities were considered in simulation. In total, the formulation of FEM of one specific problem results in a system of algebraic equations. The solution of this system of equations yields approximate values of unknowns at discrete positions across the domain. There are various types of FEM different in details; however, the main steps for generalized FEM are listed below:

1. Discretization. At first step for FEM, any solid body with complex geometry can be discretized to small finite elements. There are different numbers of nodes in different element shapes where nodes interact with each other.
2. Displacement function. The displacement of any point in a single element can be expressed as a polynomial function of the coordinates of several nodes within this small element.
3. Relationship between strain and stress. Based on the strain-displacement relation, the strain matrix can be expressed as functions of displacements of several nodes in one element. In plain strain,

$$[\boldsymbol{\varepsilon}] = \begin{bmatrix} \varepsilon_x \\ \varepsilon_x \\ \gamma_{xy} \end{bmatrix} = \begin{bmatrix} \partial/\partial x & 0 \\ 0 & \partial/\partial y \\ \partial/\partial y & \partial/\partial x \end{bmatrix} \begin{bmatrix} u \\ v \end{bmatrix} = \mathbf{B} \cdot \boldsymbol{\Delta} \quad (4-1)$$

Furthermore, the stress matrix is functions of strain matrix from the constitutive (Hooke's) law.

$$\sigma = C\varepsilon = CB\Delta \quad (4-2)$$

4. Element analysis. The forces of nodes in one element can be expressed as functions of displacements of nodes based on principle of virtual work.

$$F^e = K^e \Delta \quad (4-3)$$

5. Combination. Equations for each element are combined together in order to obtain equation set for all elements. This equation set shows the relationship between vectors of displacements  $\Delta$ , stiffness matrix  $K$  and vectors of forces for all nodes  $F_L$ :

$$F_L = K \Delta \quad (4-4)$$

6. Boundary condition and solution. The displacements of nodes on boundary are inserted into equation set. Afterwards, the equation set can be solved using numerical techniques. As a result, the corresponding strain and stress in arbitrary point can be obtained.

Above are the main steps for generalized FEM. In general, almost all physical problems in nature are nonlinear inherently. Linear approximations have advantages including, but not limited to, the smaller computational cost, validation of superposition, simple and inaccurate result. In fact, the linear assumptions are only valid in a small range, for example, small displacements, small strains, small changes in temperature, and so on. Nonlinear analysis is necessary especially when it comes to, but not limited to, investigation of failure of material, accurate enough result, a better understanding of true material behavior in physical phenomena. In mathematics, linear finite element method is based on linearized geometric equations, also called linearized displacement-strain relations:

$$\{\varepsilon\} = [B]\{d\} \quad (4-5)$$

Linearized constitutive equations (stress-strain relations):

$$\{\sigma\} = [E]\{\varepsilon\} = [E][B]\{d\} \quad (4-6)$$

And equations of equilibrium:

$$[K]\{D\} = \{R\} \quad (4-7)$$

Where stiffness  $[K]$  and forces  $\{R\}$  are independent of displacement  $\{D\}$  :

$$\begin{aligned} [K] &\neq [K(\{D\})] \\ \{R\} &\neq \{R(\{D\})\} \end{aligned} \quad (4-8)$$

On the contrary, in nonlinear problems, both the stiffness matrix  $[K]$  and forces vectors  $\{R\}$  depend on displacement  $\{D\}$  :

$$\begin{aligned} [K] &= [K(\{D\})] \\ \{R\} &= \{R(\{D\})\} \end{aligned} \quad (4-9)$$

Solution methods for nonlinear problems include, but not limited to, Newton's method, modified Newton method (Debnath, 1997).

In general, different kinds of nonlinearities can be categorized into three major types: geometric, material and contact nonlinearities. Geometric nonlinearities include large displacements, large strains, and large rotations. Material nonlinearity should be employed when material properties change with the different applied forces. As a result, the corresponding constitutive law of stress-strain relationship changes. In some point of view, contact nonlinearity may be included in geometric nonlinearity. Figure 49 shows the differences between linear and nonlinear assumptions considering different kinds of nonlinearities when a bar attaches to a torsional spring.

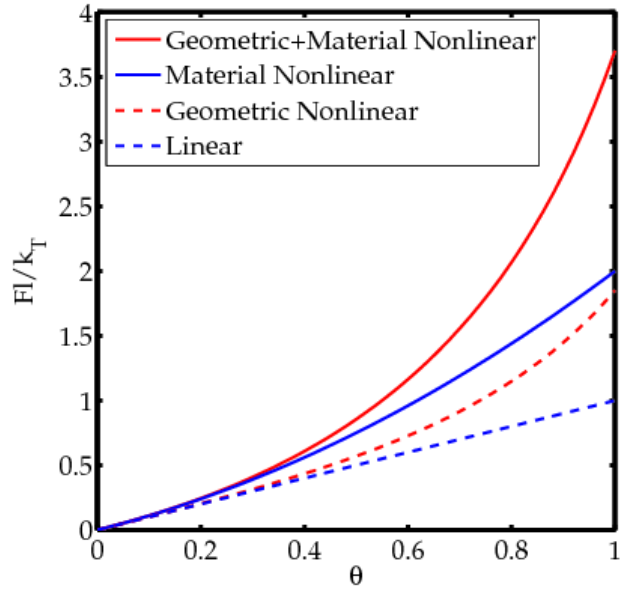


Figure 49. Forces-rotation relationship considering different kinds of nonlinearities (“Wikiversity”, 2018).

Contact interaction is also an important part in finite element analysis. Two crucial features in contact mechanics are normal behavior where stress is applied perpendicular to the contact surfaces and tangential behavior in which frictional stress is applied to the contact surfaces. For normal behavior, there are different types of contact pressure-overclosure relationships to define the contact model:

- The “hard” contact minimizes the penetration between two contact surfaces and the tensile stress is not transferred across the interface;
- a “linear” contact relationship where the contact pressure  $P$  is a linear function of the clearance  $\Delta$  between the surfaces:

$$P=K\Delta \quad (4-10)$$

- an “exponential” contact relationship where the contact pressure is an exponential function of the clearance between the surfaces:

$$p=Ke^{\beta\Delta} \quad (4-11)$$

- a “tabular” contact where a tabular pressure-overclosure relation is constructed by progressively scaling the default penalty stiffness;

For tangential behavior, there are different friction formulations involving frictionless, penalty, exponential, and so on. Due to the limit of this thesis, details about tangential behavior are not introduced.

From the above, the FEM is a numerical method for handling engineering problems involving structural analysis, heat transfer, even fluid flow and electromagnetic potential. In the field of motor industry, with the help of FEM, car crashes and bus rollover are simulated in various situations and useful guidelines are provided simultaneously (Guler, Elitok, Bayram, & Stelzmann, 2007; Jk Kim, Yim, Jeon, Jung, & Han, 2012; Witteman & Kriens, 1993). Nonlinear dynamic finite element method was used to simulate a SAE wheel impact (Chang & Yang, 2009) and stress distributions were obtained (Yildiz et al., 2012). Meanwhile, brake noise was also analyzed and brake temperature had a strong effect on noise (AbuBakar & Ouyang, 2008; Ouyang, Nack, Yuan, & Chen, 2005; Trichês Júnior, Gerges, & Jordan, 2008). Wear can also be predicted by the FEM (AbuBakar & Ouyang, 2008). In the field of biomechanics, the FEM helped to simulate dynamic loading of the knee joint on cartilage stresses and meniscus strains with explicit analyses (Figure 50) where contact pressure played a significant role on stress distribution between two surfaces (Figure 51) (Naghbi Beidokhti et al., 2016). The reliability and stability of dental implants and the transient expansion process of stent/balloon system in different stent structures were investigated based on the FEM where nonlinearities are considered (Kayabaşı, Yüzbasioğlu, & Erzincanli, 2006; Wang, Liang, Yang, & Qi, 2006). Moreover, the temperature transition from superconducting-state to normal-state was simulated with the help of the FEM (Bai, Wu, Wu, & Wang, 2006). The simulation results based on the FEM provided helpful information for LED heat dissipation and estimation of chip temperature (Cheng, Huang, & Lin, 2012).

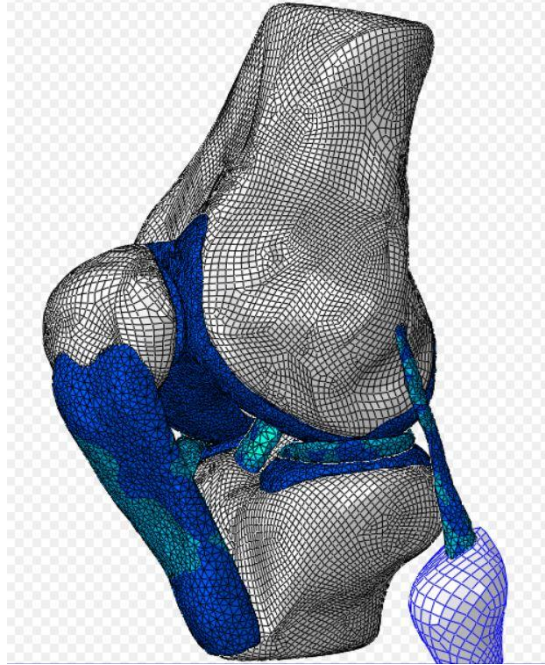


Figure 50. Finite Element Model of a human knee joint (Naghibi Beidokhti et al., 2016).

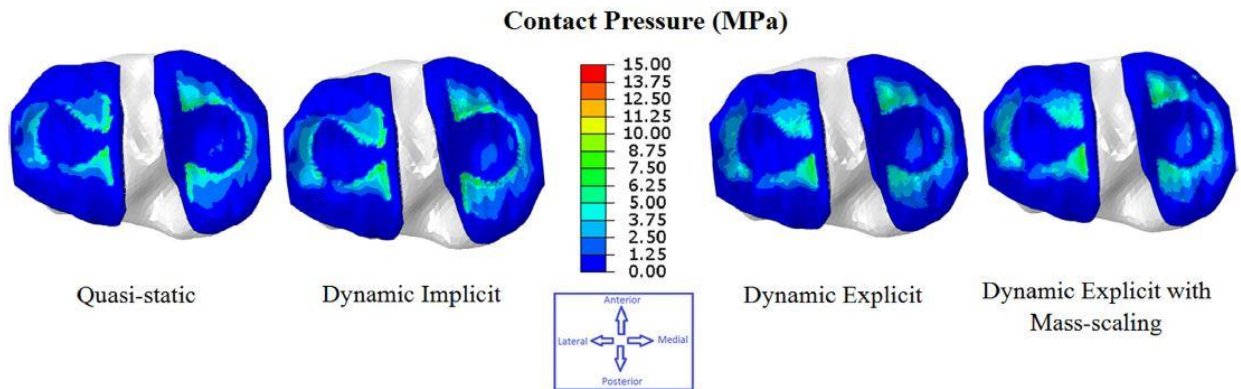


Figure 51. Contact pressure distributions in different time integration algorithms(Naghibi Beidokhti et al., 2016).

## 4.2 Methods

In this part, a commercially-available finite element code ABAQUS was used to study the interaction between a paralyzed M5 vocal fold model and the Teflon patch (e.g., AbuBakar & Ouyang, 2008; Naghibi Beidokhti et al., 2016). The aim of this numerical simulation is to find the relationship between the displacements of two edges of the Teflon patch (Leg 1 and 2) under various applied forces

and the deformation of the curve surface on a simplified paralyzed vocal fold model. And the results of numerical simulation are compared with results of experiments. The initial relative position of two parts are shown in Figure 52 where these two parts are nearly in contact status. In the following sections, details of these two parts and numerical simulation set up are described, and results are discussed.

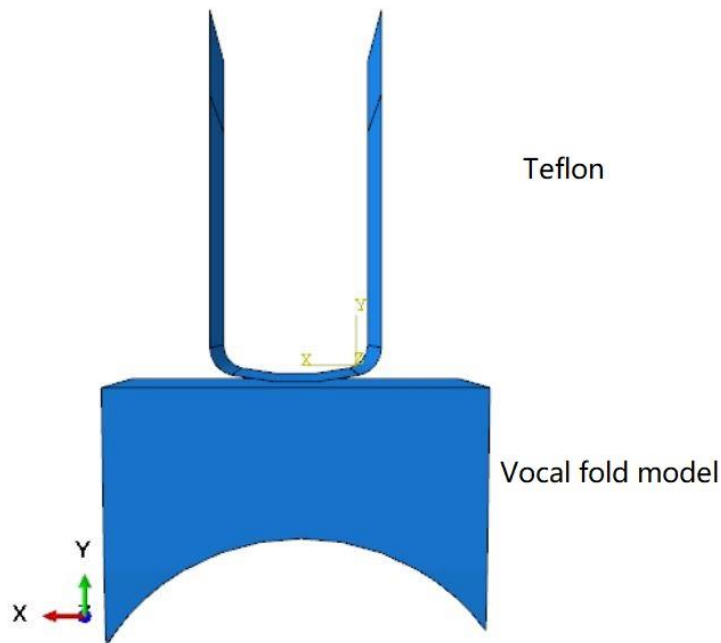


Figure 52. Relative position of the paralyzed vocal fold model and Teflon.

#### 4.2.1 Simulation set up

When it comes to element type, there is an extensive element library providing a powerful set of tools for solving different problems in ABAQUS. Geometry type is the major distinction between different element types: continuum, shell, membrane, beam, and so on. Each problem can be solved by one or more element types. Element type can be chosen by different concerns: analysis types, degrees of freedom, and different parameters from customer concerns. Hexahedral element is recommended by ABAQUS with a solution of equivalent accuracy at least computational cost. Tetrahedral element in ABAQUS is geometrically versatile and can be meshed automatically without partition before meshing.

First-order tetrahedral element (C3D4) is stiff especially in less quantity, and fine meshes are necessary to reach high accuracy results. However, the modified second-order tetrahedral element type (C3D10M) is robust for large deformation and contact problems. As a result, different element types are discussed in details for each part in next section.

In general, there are two algorithms for modeling contact in ABAQUS, general contact and contact pairs. The surfaces in general contact that can interact with more than one surfaces at the same time. Moreover, the general contact is defined automatically without specifying each individual surface. Besides, the general contact algorithm is faster than the contact pair. As a result, general contact was defined in initial step in this study. For contact property, “Hard Contact” which minimized the penetration between two contact surfaces was used in pressure-overclosure relationship as described in Section 4.1 for normal behavior. Before experiments, lubricating oil was used on the contact surfaces between Teflon patch and synthetic vocal fold model. Due to the friction was quite small, the friction coefficient was defined as 0.01 for tangential behavior. It is worth pointing out that the element size of slave surface in contact is supposed to be smaller than that of master surface.

General static step was created in this study to investigate the relationship between the applied forces on the two legs of Teflon and deformation of paralyzed vocal fold under static situation. In this step, geometric nonlinearity was considered due to large displacements and contact. Dissipated energy fraction in automatic stabilization was set to 0.0002. Initial, minimum, and maximum increment size was 0.05, 1E-010, 0.1 for automatic incrementation, respectively. It is worth noting that discontinuous analysis should be considered for convergence in all steps other than Initial step due to complexity of this simulation when large displacements of legs of Teflon happened.

Several groups of numerical simulation corresponding with the experimental groups are conducted where boundary conditions are shown in Figure 53. In order to match the boundary conditions in experiments as much as possible, the two lateral boundaries of the vocal fold model are encastre boundary

conditions suggesting  $U1=U2=U3=0$  and  $UR1=UR2=UR3=0$  at the same time. The top parts of legs of Teflon are constrained with  $U1=U3=0$  indicating that this part can move only in y direction. Two reference points, RP-1 and RP-2, are used to set displacements of two individual legs of Teflon by equation constraints coupling reference points and legs of Teflon. During simulation, the necessary external forces applied on the reference points were monitored.

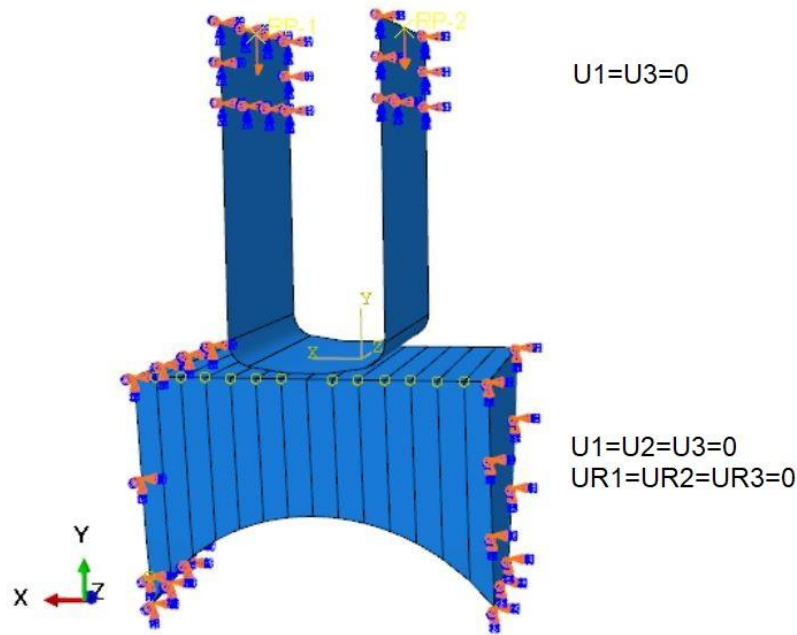


Figure 53. Boundary conditions for two parts and reference points in numerical simulation.

#### 4.2.2 Vocal fold part

All geometry sizes of the paralyzed vocal fold model and Teflon in numerical simulation follow the sizes in experiments. This part, the paralyzed vocal fold model, was 4.6 times of the prototype of the M5 geometry. Geometry parameters in details are described in Section 3.2.2.

The relationship between stress and strain of this synthetic material was obtained in Chapter 2. Figure 16 in Chapter 2 shows it is a typical hyper elastic material behavior. Hyper elastic materials are described in terms of strain energy potential which defined the strain energy stored in material per unit

volume as a function of strain. In general, there are different forms of strain energy potentials available in ABAQUS: the Arruda-Boyce form, Mooney-Rivlin form, Neo-Hookean form, Ogden form, and (Reduced) polynomial form. Moreover, the material behavior can be calibrated by Marlow model directly from experimental stress-strain data obtained in Chapter 2 without obtaining the fitting coefficients of the stress-strain curve at first. In other words, with the help of this Marlow model, the test data can directly characterize the strain energy potential avoiding errors from fitting the test data in other nonlinear models. The Poisson's ratio 0.475 was used by default in this study for hyper elastic rubber-like materials.

Hybrid element is recommended by ABAQUS user's guide for incompressible and nearly incompressible hyper elastic materials. Hexahedral elements usually provides a solution of equivalent accuracy at less cost than tetrahedron. Mesh distortion became severe when displacements of Leg 1 and 2 were large in experiments. Reduced-integration, first-order element is recommended by ABAQUS during contact. In the end, first-order, reduced-integration hexahedral hybrid element (C3D8RH) was used for modeling vocal fold part.

In order to find the relationship between the external forces applied on Teflon, the corresponding displacements and the deformation of the curve surface on paralyzed vocal fold model, grid independence was investigated for vocal fold model part at first. There are 35 and 10 elements in x and y direction on vocal fold part in Figure 54, respectively, resulting in 19,926 nodes in total on vocal fold model part. The vocal fold would be bended in y direction which is parallel to the displacements of legs of Teflon. There is no need to use fine mesh in the transverse z direction. Three different meshes are investigated for grid independence which is listed in details in Table 5.

Table 5. Different meshes used in grid independence (Figure 54).

Name	Number of nodes in total on vocal fold part	number of elements in x direction	number of elements in y direction
Mesh 1	19,926	35	10
Mesh 2	26,240	56	10
Mesh 3	30,709	35	15

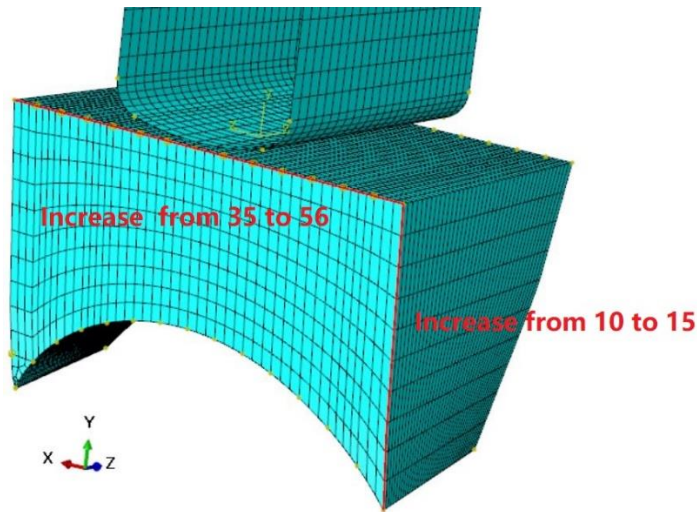


Figure 54. Demonstration of mesh on paralyzed vocal fold model.

The necessary forces in four conditions (L6.0R6.0, L10.0R10.0, L15.0R15.0, and L20.0R20.0) resulting from numerical simulation are compared to experimental results in Table 6. In the table below, Mesh 1 with 19,926 number of nodes on vocal fold part matches the results of experiments with minimum error, especially in conditions of large displacements of legs of Teflon. The displacements of one point on the curve surface of vocal fold model are monitored during simulation. The position of this monitor point is shown in Figure 55. In Table 7, almost all meshes (Mesh 1, 2, and 3) had the same error on displacements of the monitor point compared to experiments. Based on the results of necessary forces and displacements of monitor point from numerical simulation, Mesh 1, the minimum number of nodes, can meet the requirement of grid independence. Increasing the number of elements in x and y directions on vocal fold part do not have less error compared to experiments. Mesh 1 was employed in the following study.

Table 6. Comparison of necessary forces between numerical simulation and experiments on four configurations.

Number of nodes	Necessary forces at L6R6 (N)		Necessary forces at L10R10 (N)		Necessary forces at L15R15 (N)		Necessary forces at L20R20 (N)	
Exp.	-3.6151		-5.1401		-9.6040		-10.8290	
Mesh 1	-3.1824	11.96%	-6.2098	-20.81%	-10.3405	-7.67%	-14.5649	-34.50%

Mesh 2	-3.1830	11.95%	-6.1961	-20.54%	-10.3218	-7.47%	-16.5046	-52.41%
Mesh 3	-3.1739	12.20%	-6.1888	-20.40%	-10.2939	-7.18%	-15.3051	-41.33%

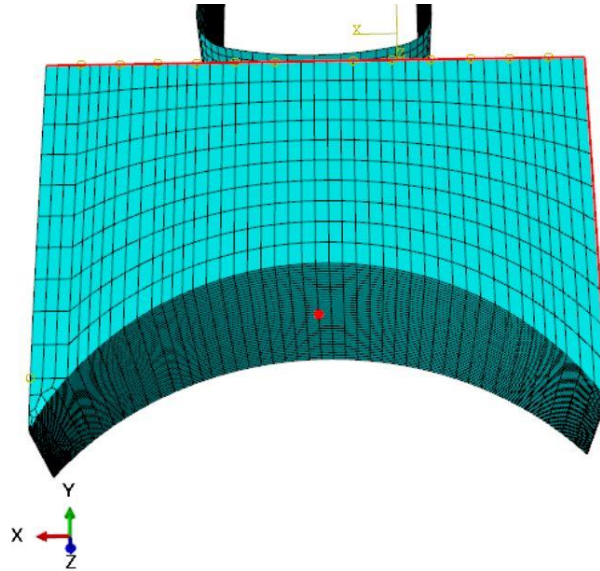


Figure 55. Schematic of the position of monitor point on curve surface.

Table 7. Comparison of displacements of the monitor point on curve surface of vocal fold model between numerical simulation and experiments.

Disp. of both legs of Teflon (m)	Disp. of the monitor point in experiment	Disp. of the monitor point with Mesh 1	Error	Disp. of the monitor point with Mesh 2	Error	Disp. of the monitor point with Mesh 3	Error
-0.006	-0.00642	-0.0042	34.6%	-0.0042	34.6%	-0.0042	34.6%
-0.010	-0.00879	-0.0075	14.7%	-0.0075	14.7%	-0.0076	13.5%
-0.015	-0.01278	-0.0118	7.7%	-0.0118	7.7%	-0.0118	7.7%
-0.020	-0.01922	-0.0159	17.3%	-0.01576	18.0%	-0.0159	17.3%

#### 4.2.3 Teflon part

The geometry of Teflon patch used in numerical simulation matches experiments as much as possible (Figure 56). The transverse length of Teflon in z direction is same with transverse length of vocal fold model which is 5 cm. The thickness of Teflon part is 1 mm. The thickness of Teflon is extremely

smaller compared to its length and width, and reduced-integration shell element (S4R) was employed to model Teflon. Teflon part is meshed by fine grid as shown in Figure 57, there is no need to investigate grid independence on Teflon. The Young's modulus and the Poisson ratio of the Teflon patch is 0.5 GPa and 0.46, respectively (DuPont, 2018).

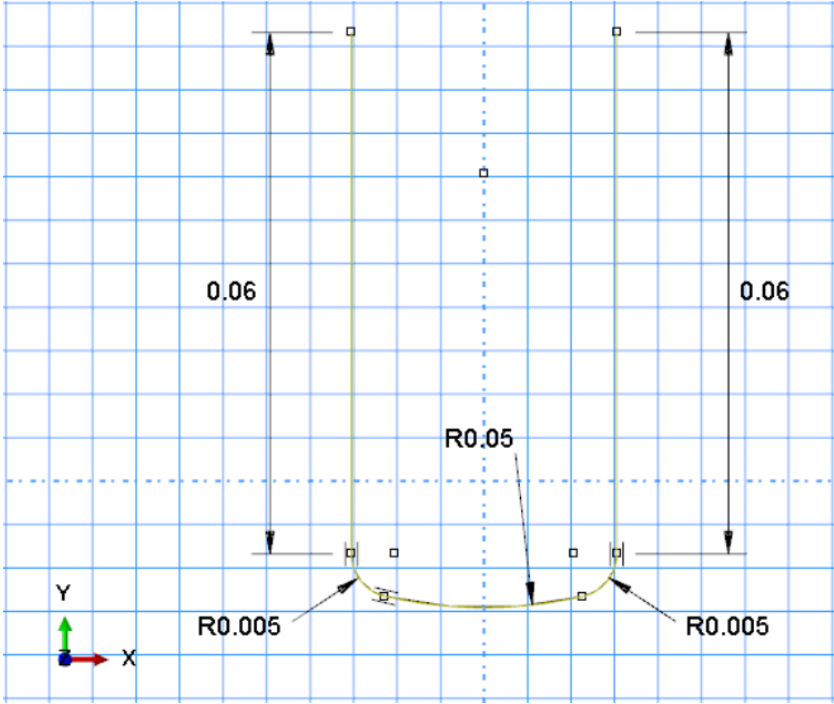


Figure 56. Geometry of Teflon patch used in numerical simulation.

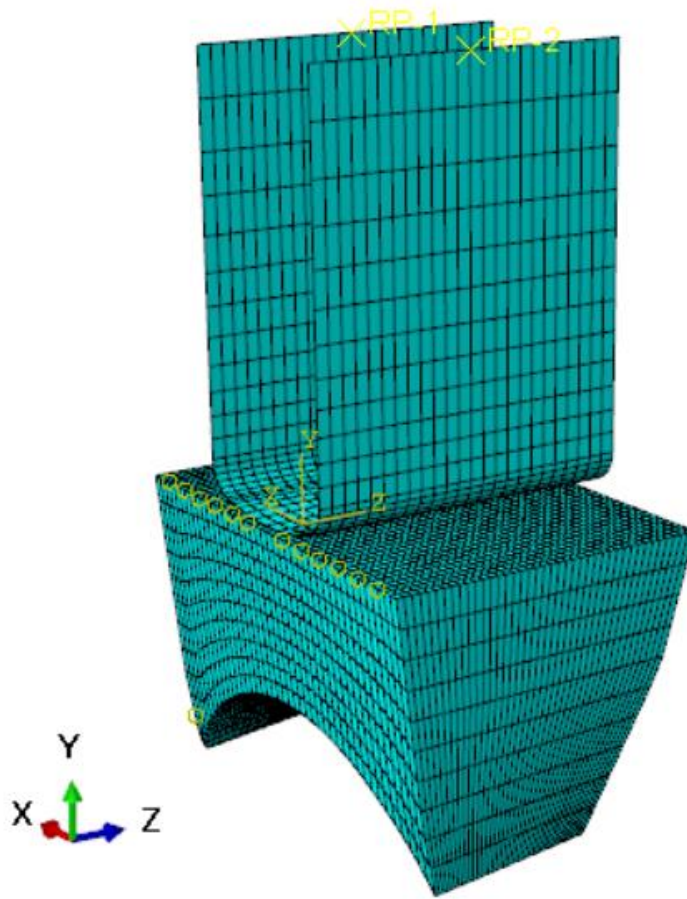


Figure 57. Schematic of mesh information used in numerical simulation.

## 4.3 Results and conclusion

### 4.3.1 Comparison of simulations and experiments

Comparison of numerical simulations and experiments on relationship between displacements and applied forces of Teflon is shown in Figure 58 on four different configurations (L6.0R6.0, L10.0R10.0, L15.0R15.0, L20.0R20.0). The fitting line of simulation results in Figure 58 seems to be linear. However, hyper elastic material property was already used to run these simulations. The error is tiny in the conditions that displacements are smaller than 0.015 m. The simulation can provide accurate results of prediction for designing this new adjustable device when deformation was not large. However, the error is up to 30% when the displacement of Teflon is 0.02 m. One possible reason may be that the necessary

stress-strain relationship at L20.0R20.0 condition beyond the limit of stress-strain curve which obtained in Section 2.4. Besides, nonlinearities in nature are always one extremely complex problem to be predicted accurately especially in large deformation.

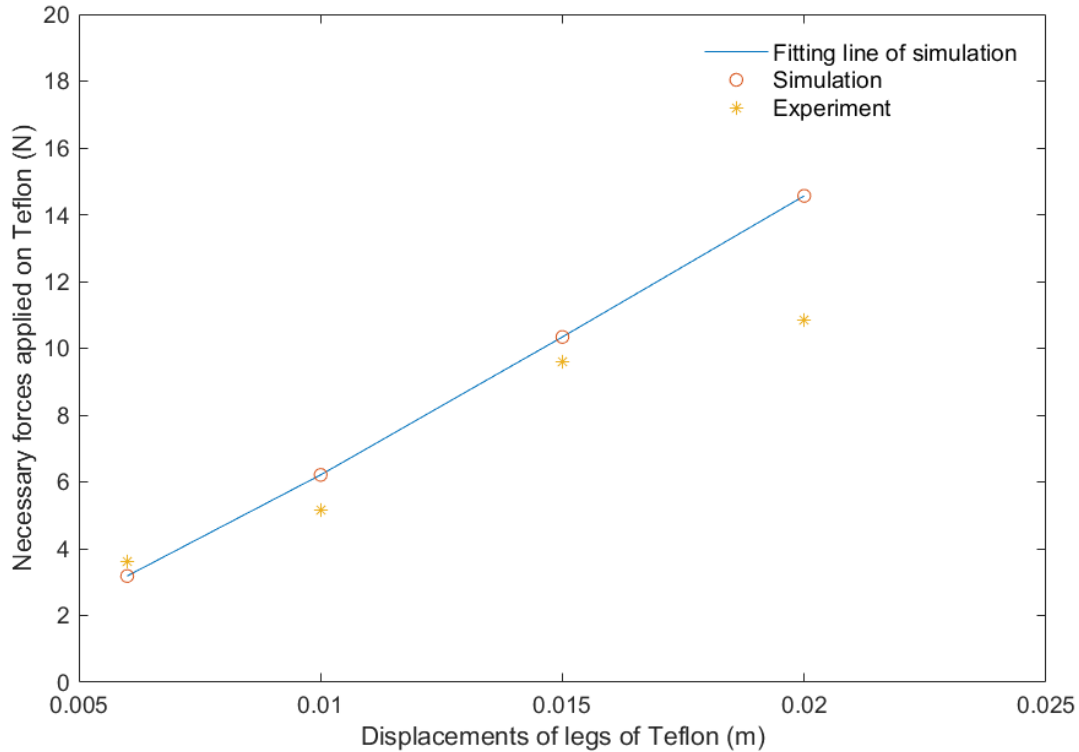


Figure 58. Comparison of numerical simulation and experiments on relationship between displacements and applied forces of Teflon.

Figure 59 below shows the comparison of numerical simulation and experiments on relationship between displacements of Teflon and displacements of the monitor point on curve surface of paralyzed vocal fold model. The fitting line of simulation results seems to be linear as before. The error is tiny when displacements of Teflon are less than 0.015 m. However, the error in the condition when displacement is 0.02 m is large as before. In total, the simulation results are always lower than those from experiments in every condition especially when displacements are small and large. The large error when displacement is small may due to the error from measuring tool. This Doppler device yielded large data sometimes during experiments. If y coordinate of the monitor point under unloading condition was large due to error from

the Doppler device and y coordinate of the monitor point under L6.0R6.0 condition was correct, the downward displacement of monitor point was large as a result in experiment.

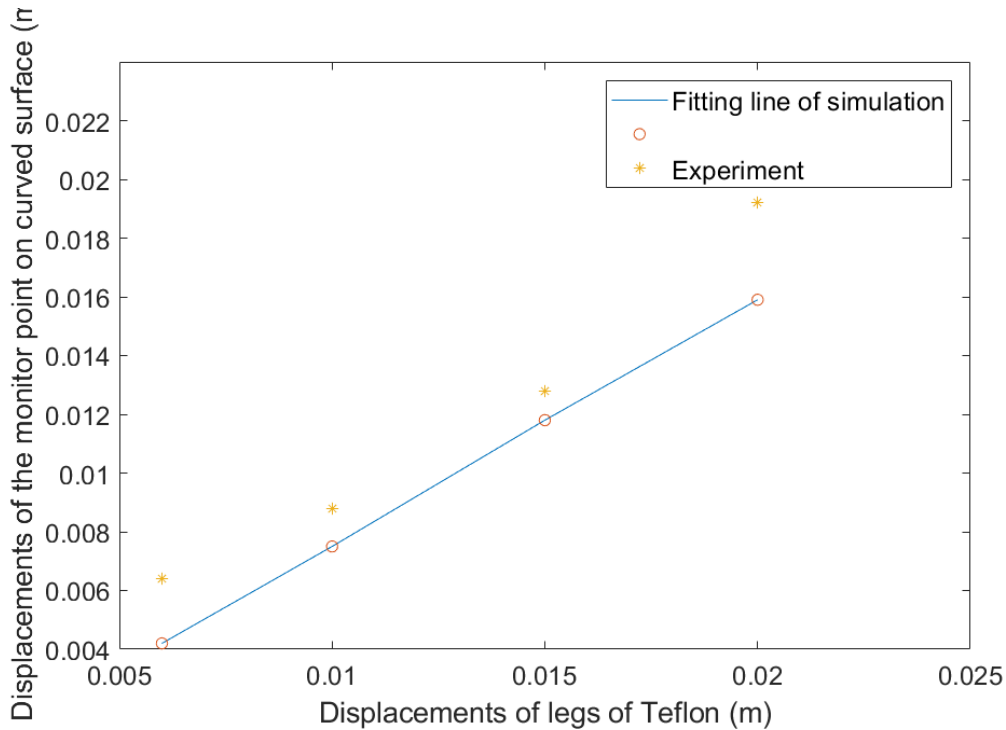


Figure 59. Comparison of numerical simulation and experiments on relationship between displacements of Teflon and displacements of the monitor point.

#### 4.3.2 Investigation of adjustable implant

As discussed before, the paralyzed vocal fold model used in experiments was 4.6 times of the prototype of vocal fold in reality. In order to quantitatively investigate the relationship between the deformation of the curve surface on the prototype of paralyzed vocal fold and the externally necessary forces applied on legs of Teflon, the displacements of Leg 1 of Teflon are supposed to be fixed at 4.6 mm, 9.2 mm, and 13.8 mm, respectively, suggesting the displacements of Leg 1 of the prototype of Teflon in reality, not model in these experiments, are 1, 2, and 3 mm. In order to simulate the operation procedure of this adjustable implant during surgery as much as possible, simulation was run where the displacement of Leg 1 of Teflon was increased from 0 to 4.6 mm and Leg 2 was fixed at 0 in step 1, and displacement of Leg 2 was increased from 0 to 18.4 mm and Leg 1 was fixed at 4.6 mm in step 2. In real surgery, a

surgeon adjusts the legs of Teflon individually, not adjusts together at the same time if both legs of Teflon should be pushed.

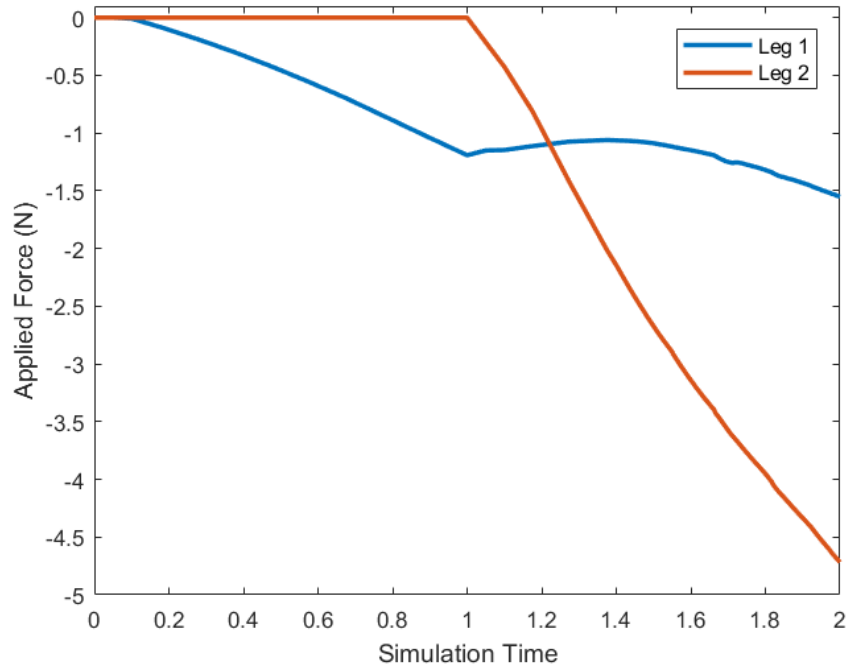


Figure 60. Applied forces on Leg 1 and 2 of Teflon during simulation

Figure 60 shows the applied forces on Leg 1 and 2 of Teflon during simulation respectively. Within step 1, the amplitude of applied force on Leg 1 was increased from 0 to 1.19 N. Afterwards in step 2, this force applied on Leg 1 decreased slightly and then increased. One possible reason may be the bending moment (Figure 61) in Leg 1 of Teflon decreased at first in step 2 then increased (Figure 62) with displacement of Leg 2 increasing from 0 to 18.4 mm. Figure 61 and 62 show y displacements of Teflon and the corresponding deformation of the paralyzed vocal fold model at the end of step 1 and step 2, respectively. In Figure 62, when the maximum difference of displacement between Leg 1 and 2 is reached, the curve surface of vocal fold model shows bilateral symmetry which agrees well with experiments. From Figure 63, when displacements of Leg 2 increased from 0.002 to 0.0184, the amplitude of applied forces on Leg 1 decreased at first then increased. The minimum force on Leg 1 is reached at the condition where displacements of Leg 1 and 2 are both at 0.006 m suggesting there is no

bending moment in Leg 1. Applied force on Leg 2 in Figure 55 has an approximately linear relationship with simulation time in step 2 ranging from 0 to 5 N. Figure 64 shows relationship between the applied forces and displacements on Leg 2 in step 2 which is linear approximately. Displacements in y direction of the monitor point on curve surface is shown in Figure 65 when the applied force on Leg 2 of Teflon is increased. It should be noted that the monitor point moved downward from 0 to -0.002 m when there is no applied force on Leg 2. The increasing displacement of Leg 1 in step 1 results in the downward movement of the monitor point.

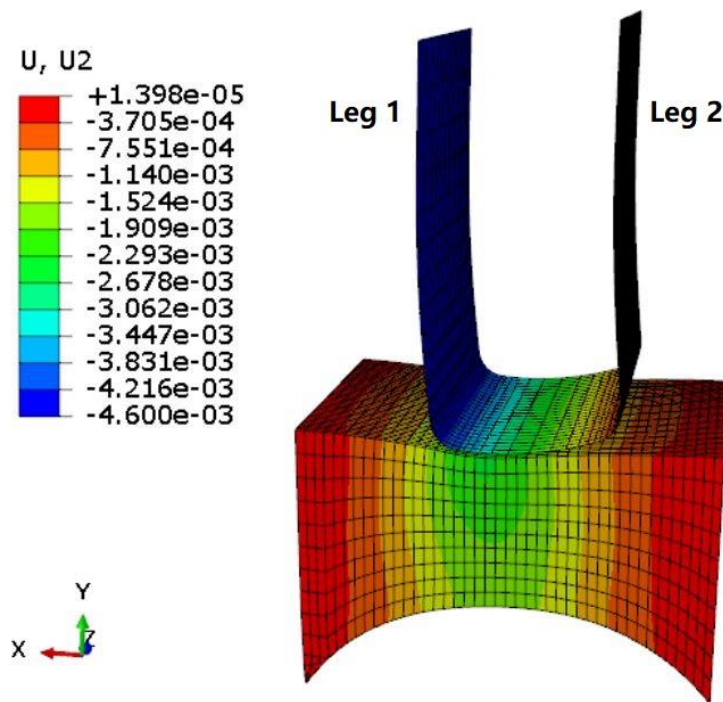


Figure 61. Displacements of Teflon and paralyzed vocal fold model at the end of step 1 in y direction.

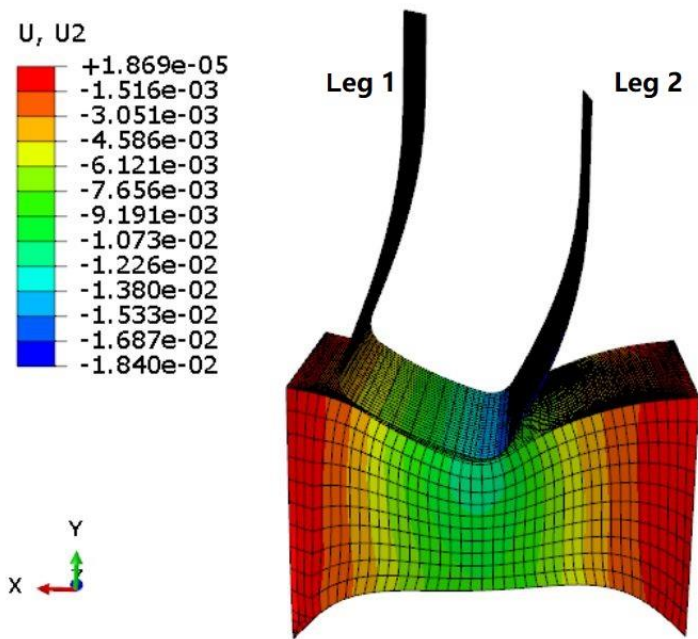


Figure 62. Displacements of Teflon and paralyzed vocal fold model at the end of step 2 in y direction.

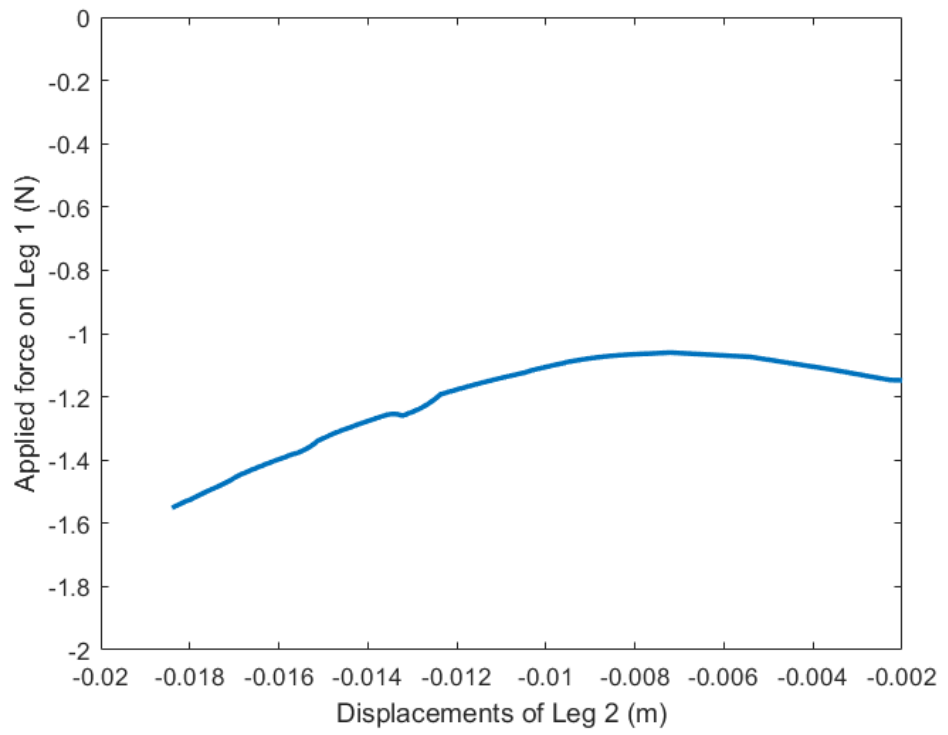


Figure 63. Applied forces on Leg 1 when displacements of Leg 2 increased.

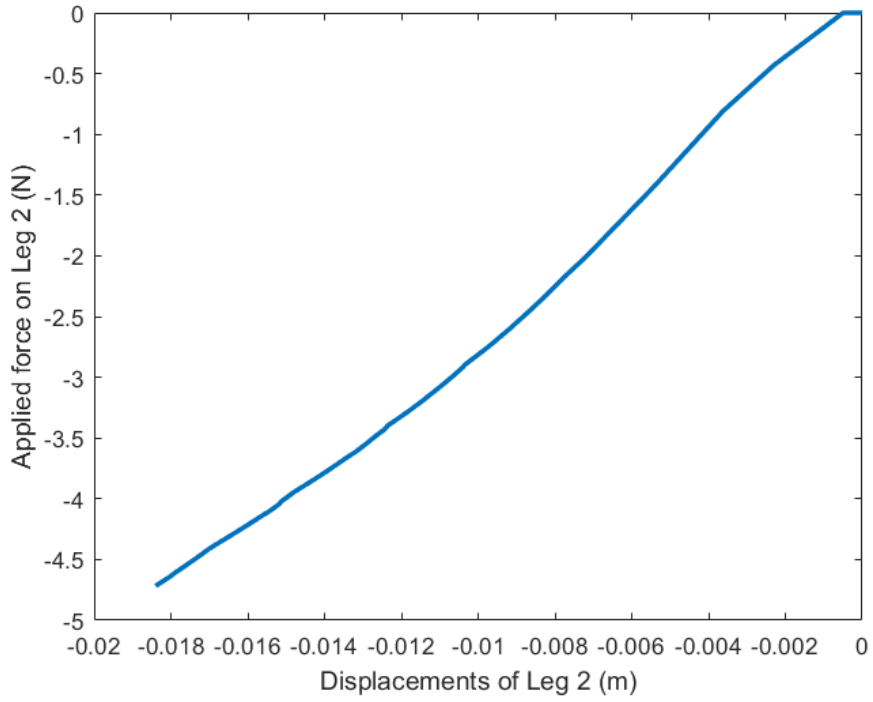


Figure 64. Relationship of the applied forces and displacements on Leg 2.

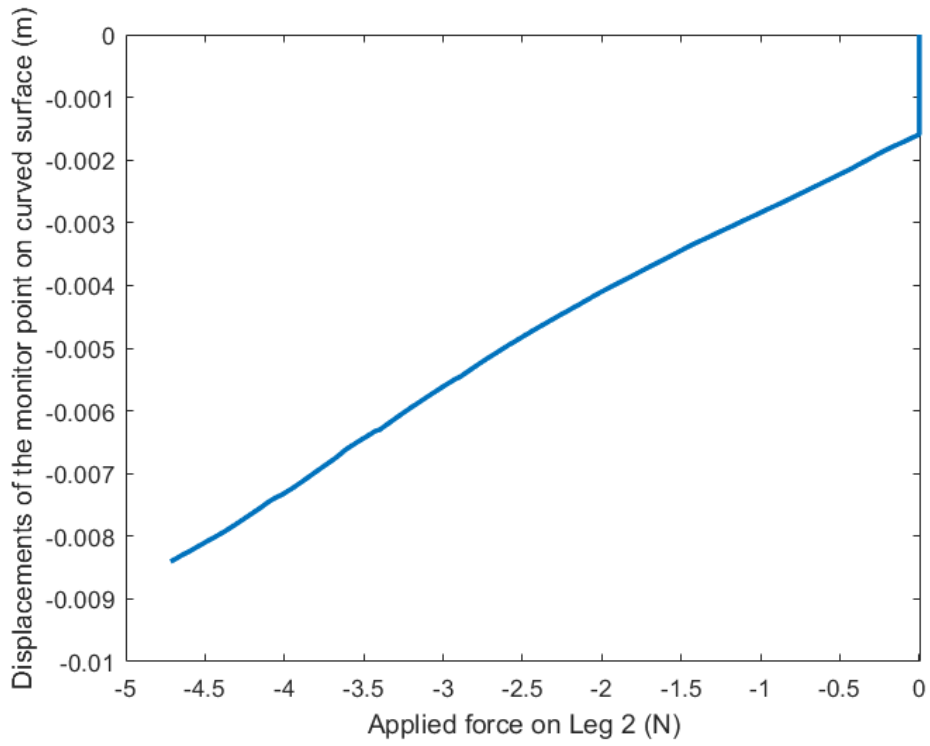


Figure 65. Displacements in y direction of the monitor point on curve surface with applied force on Leg 2 increasing.

The displacement of Leg 1 at 2 mm for the prototype of paralyzed vocal fold corresponds with the displacement of Leg 1 for the model at 9.2 mm. During surgery, Leg 1 should be pushed 2 mm by surgeon at first step, then Leg 2 should be pushed subsequently. As for paralyzed vocal fold model used in this study, not prototype, Leg 1 should be pushed 9.2 mm then Leg 2. However, simulations are divergent in this sequence. Instead, Leg 1 and 2 are pushed 9.2 mm together in step 1 and Leg 2 is pushed from 9.2 mm to 18.2 mm continuously in step 2. Fine mesh with 32,493 nodes was used for the following simulations. Figure 66 shows that the applied forces on Leg 1 and 2 of Teflon vary with displacements of the monitor point on curve surface of paralyzed vocal fold model. In Figure 66, the applied force on each leg of Teflon is same when the monitor point moved from 0 to -0.0068 mm because they are pushed together in step 1. The applied force on Leg 1 decreases a little at the beginning of step 2, then continues to increase with a less slope compared to the slope of Leg 2. This decrease at the beginning of step 2 may result from Leg 2 undertaking most of the reaction force from vocal fold model at the beginning of step 2. Von Mises stresses across Teflon at the end of step 1 and at the beginning of step 2 are shown in Figure 67 and 68, respectively. The low stress region on Leg 1 at the beginning of step 2 in Figure 68 is slightly larger than the low region on Leg 1 at the end of step 1 in Figure 67. Furthermore, the low Von Mises stress region of Leg 2 at the beginning of step 2 is obviously smaller than the low Von Mises stress region of Leg 2 at the end of step 1. Moreover, at the beginning of step 2, there is a yellow region of Von Mises stress at the end of Leg 2 suggesting higher stress. These are the reasons why applied force on Leg 2 increased at a large slope and applied force on Leg 1 decreased at the beginning of step 2.

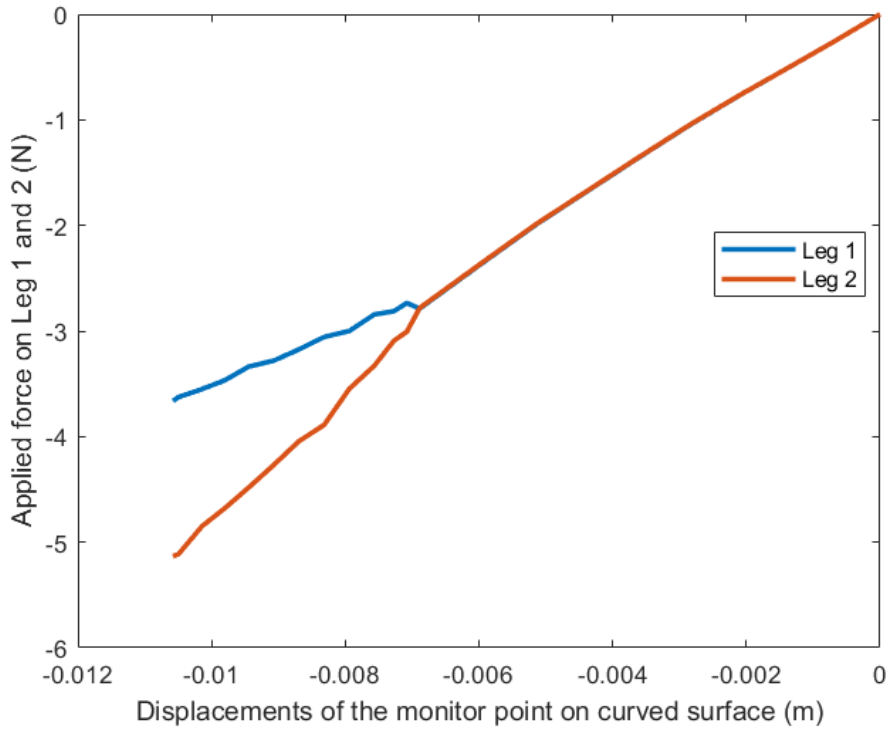


Figure 66. Relationship between displacements of monitor point and applied force on each leg when displacement of Leg 1 and 2 was set to 9.2 mm at step 1.

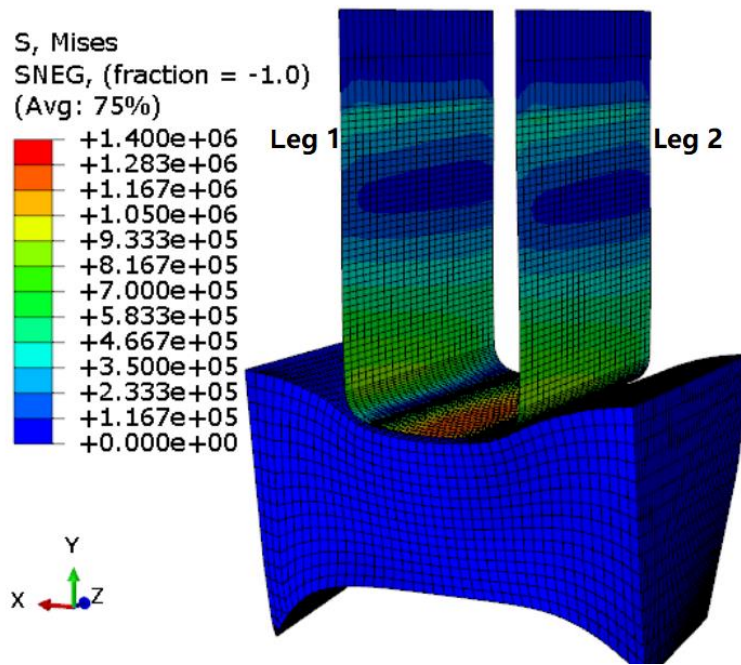


Figure 67. Von Mises stress distribution across Teflon at the end of step 1.

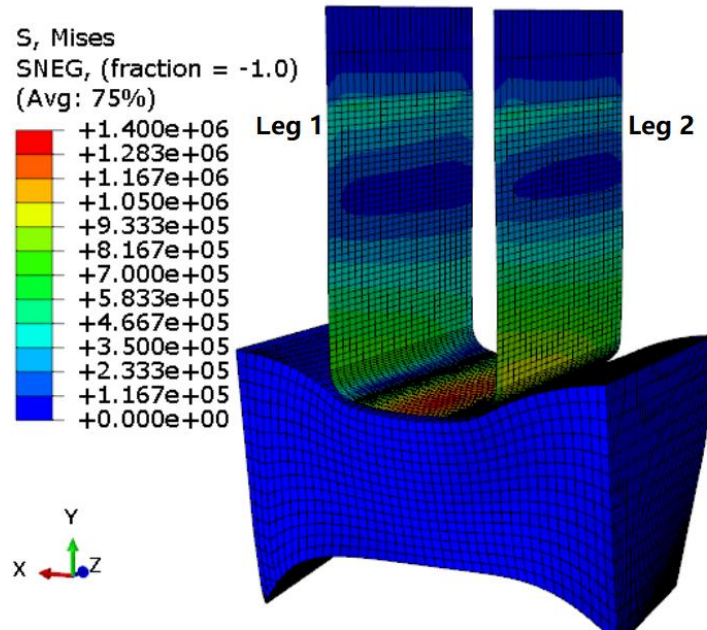


Figure 68. Von Mises stress distribution across Teflon at the end of step 2.

When the displacement of Leg 1 is 3 mm for the prototype of paralyzed vocal fold, the corresponding displacement of Leg 1 for the model should be 13.8 mm. Similarly, due to divergence problem, simulation was run where displacements of Leg 1 and 2 moved 13.8 mm together in step 1 and displacement of Leg 2 moved from 13.8 mm to 18.4 mm in step 2. From Figure 69, when displacement of Leg 1 and 2 is 13.8 mm, the displacement of the monitor point is 11 mm at the end of step 1. Similarly, the applied force of Leg 1 decreases at first in step 2 then increases. The reason has been pointed out before.

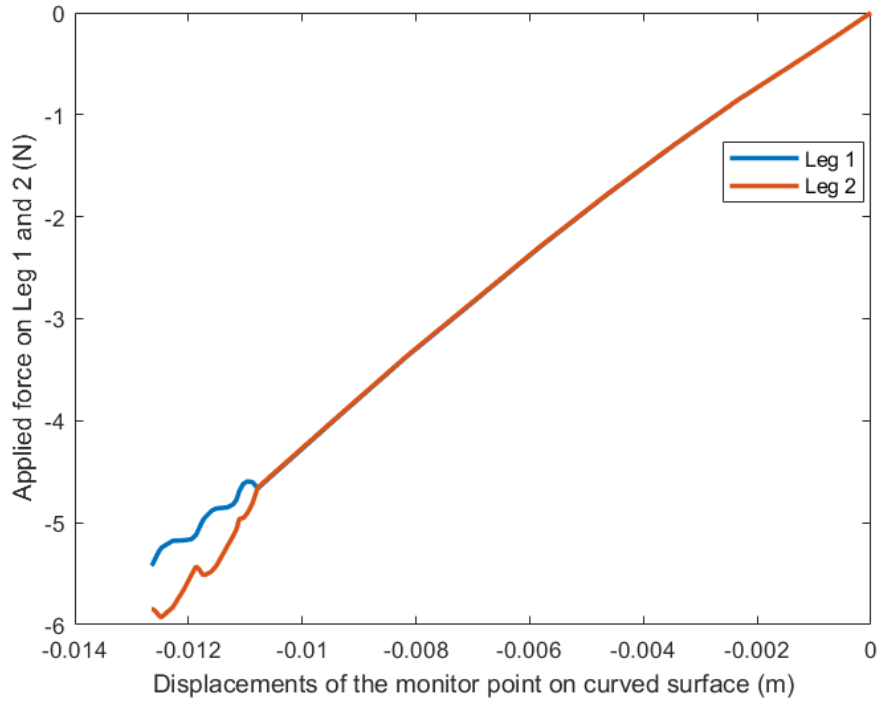


Figure 69. Relationship between displacements of monitor point and applied force on each leg when displacement of Leg 1 and 2 was set to 13.8 mm at step 1.

## CHAPTER 5

### CONCLUSION

The results of 14 groups of experiments quantitatively studied the necessary forces applied on two legs of Teflon and the corresponding deformation of the curve surface on paralyzed vocal fold model suggesting the forces for the prototype of paralyzed vocal fold can be obtained thereafter based on similarity theory. Based on numerical simulation on contact between the paralyzed vocal fold model and Teflon patch, the applied forces on Teflon used in prototype of vocal fold, not the model in experiments, can be calculated if the paralyzed vocal fold was decreased 4.6 times with the help of similarity theory. Figure 70 shows the draft geometry of the built-in base embedded in Thyroid cartilage. If Leg 1 moves 1 mm in surgery and be kept thereafter, the tooth which hold Leg 1 should apply

$$1.5510 \div 4.6^2 = 0.073N$$

Figure 71 shows the applied force on Leg 2 and the corresponding displacements of the monitor point in prototype of vocal fold and Teflon. The relationships between displacements of monitor point and the applied force on each leg of Teflon when displacement of Leg 1 and 2 was 2 mm for the prototype of paralyzed vocal fold are shown in Figure 72 and 73.

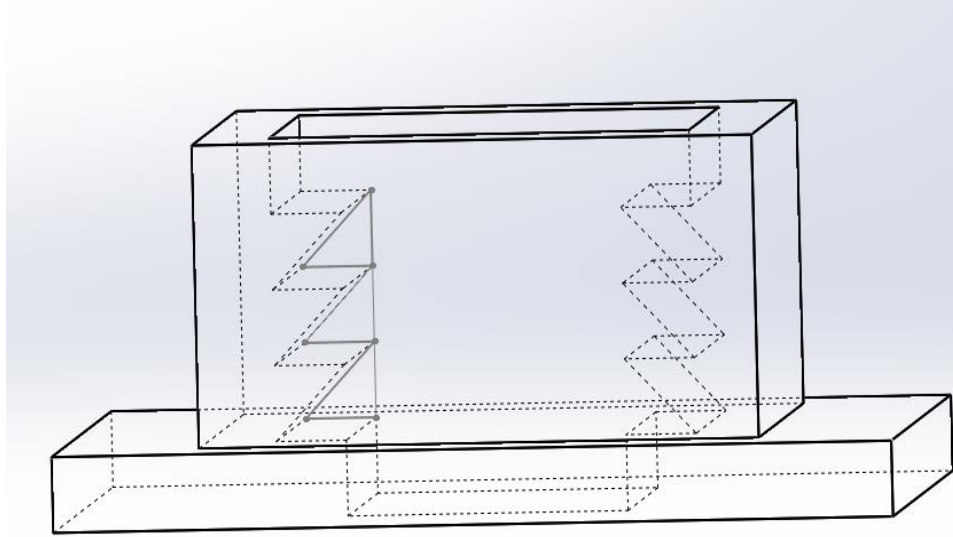


Figure 70. Inner geometry of the built-in base embedded in Thyroid cartilage.

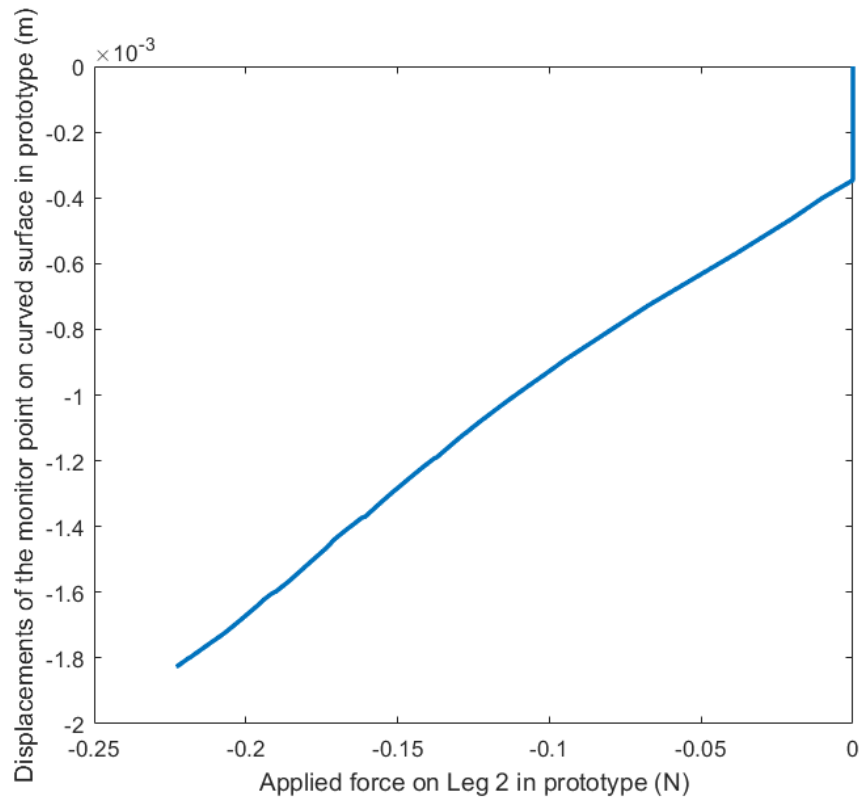


Figure 71. Displacements of the monitor point on curve surface and the corresponding applied force on Leg 2 in prototype of vocal fold and Teflon.

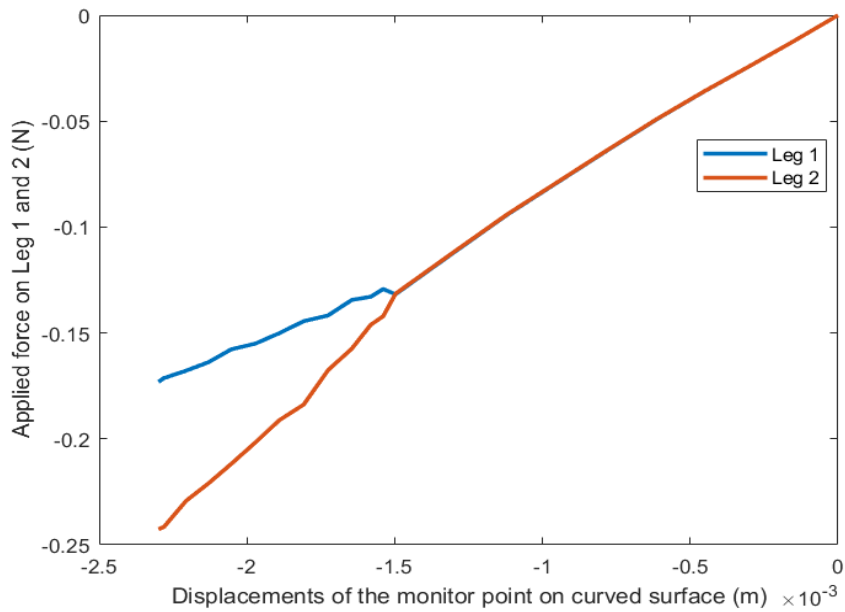


Figure 72. Relationship between displacements of monitor point and applied force on each leg when displacement of Leg 1 and 2 was 2 mm for prototype of paralyzed vocal fold.

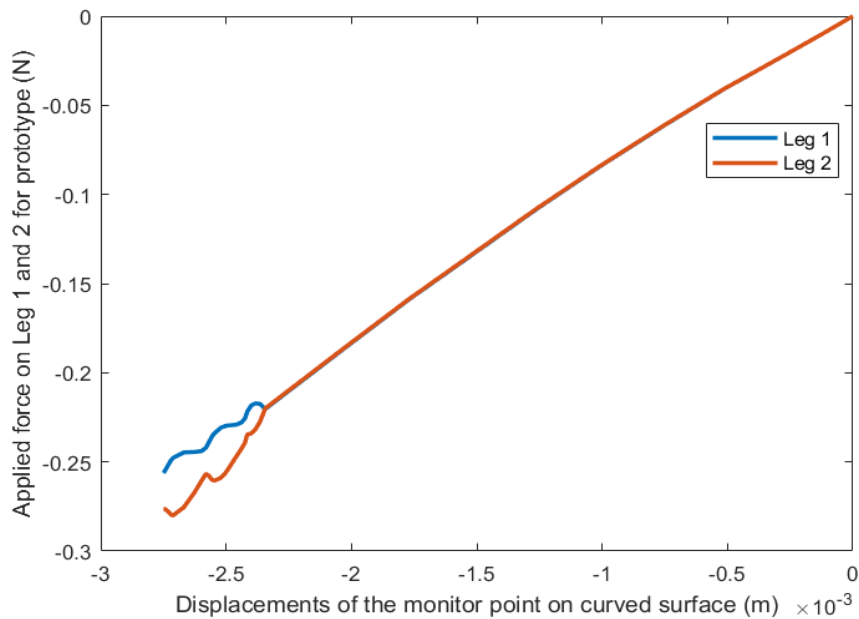


Figure 73. Relationship between displacements of monitor point and applied force on each leg when displacement of Leg 1 and 2 was 3 mm for prototype of paralyzed vocal fold.

Based on the experimental data in Figure 46 and simulation data in Figure 64, force on one leg is affected by the displacement of the other leg in asymmetric configurations. As a result, symmetry of legs of Teflon is better and simple for implant, asymmetry of legs is complex and unstable which should be avoided in surgery.

Moreover, the curve surfaces on the paralyzed vocal fold model in different configurations are always shown bilateral symmetry approximately regardless of the difference of displacements of two legs of Teflon. In asymmetric configurations, the contact point will gradually slide to midpoint of vocal fold as displacement of Leg 2 increase.

The results of experiments are also the foundations of numerical simulation. The results of numerical simulation agree well with the results from corresponding experiments where the error of necessary forces of Teflon and the error of displacements of monitor point are both around 10%. Although largest error on necessary force is 34.5% at large deformation, the range of error between numerical simulation and experiments is clear for prediction of the contact process of Teflon and paralyzed vocal fold in surgery in future.

External force is the sum of the applied force on legs of Teflon obtained from simulation which can push Teflon forward and the maximum static friction force between teeth on legs of Teflon and teeth on the base embedded in Thyroid cartilage.

## BIBLIOGRAPHY

- AbuBakar, A. R., & Ouyang, H. (2008). Wear prediction of friction material and brake squeal using the finite element method. *Wear*, 264, 1069–1076.
- Alipour, F., Berry, D. A., & Titze, I. R. (2000). A finite-element model of vocal-fold vibration. *The Journal of the Acoustical Society of America*, 108, 3003–3012.
- Amy, C. (2018, June 5). *A Real Explanation for Vocal Fatigue*. Retrieved from <http://www.ohniww.org/vocal-fatigue/>.
- Anne, R.K. (2016, February 7). *Singers, take care! Protect yourself from vocal abuse*. Retrieved from <http://rustyknuckles.blogspot.com/2016/02/singers-take-care.html>.
- Atzberger, P. J., Kramer, P. R., & Peskin, C. S. (2009). A Stochastic Immersed Boundary Method for Fluid-Structure Dynamics at Microscopic Length Scales, 1–52.
- Bai, Z. M., Wu, X., Wu, C. L., & Wang, J. X. (2006). Quench propagation properties analysis of high-temperature superconductors using finite element method. *Physica C: Superconductivity and Its Applications*, 436, 99–102.
- Benninger, M. S., Murry, T., & Johns, M. M. (2015). The Performer's Voice, 480.
- Chang, C. L., & Yang, S. H. (2009). Simulation of wheel impact test using finite element method. *Engineering Failure Analysis*, 16, 1711–1719.
- Cheng, H. H., Huang, D. S., & Lin, M. T. (2012). Heat dissipation design and analysis of high power LED array using the finite element method. *Microelectronics Reliability*, 52, 905–911.
- Chhetri, D. K., Zhang, Z., & Neubauer, J. (2011). Measurement of Young's modulus of vocal folds by indentation. *Journal of Voice*, 25, 1–7.
- De Oliveira Rosa, M., Pereira, J. C., Grellet, M., & Alwan, A. (2003). A contribution to simulating a three-dimensional larynx model using the finite element method. *The Journal of the Acoustical Society of America*, 114, 2893.
- Debnath, L. (1997). Nonlinear Partial Differential Equations, 49, 507–554.
- Deverge, M., Pelorson, X., Vilain, C., Lagrée, P.-Y., Chentouf, F., Willems, J., & Hirschberg, A. (2003). Influence of collision on the flow through in-vitro rigid models of the vocal folds. *The Journal of the Acoustical Society of America*, 114, 3354–3362.
- Doellinger, M., & Berry, D. A. (2006). Visualization and Quantification of the Medial Surface Dynamics of an Excised Human Vocal Fold During Phonation. *Journal of Voice*, 20, 401–413.
- Drechsel, J. S., & Thomson, S. L. (2008). Influence of supraglottal structures on the glottal jet exiting a two-layer synthetic, self-oscillating vocal fold model. *The Journal of the Acoustical Society of America*, 123, 4434–4445.

- Erath, B. D., & Plesniak, M. W. (2006). An investigation of bimodal jet trajectory in flow through scaled models of the human vocal tract. *Experiments in Fluids*, *40*, 683–696.
- Friedrich, G. (1999). Titanium vocal fold medializing implant: Introducing a novel implant system for external vocal fold medialization. *Annals of Otolaryngology, Rhinology and Laryngology*, *108*, 79–86.
- Geng, B., Xue, Q., & Zheng, X. (2016). The effect of vocal fold vertical stiffness variation on voice production. *The Journal of the Acoustical Society of America*, *140*, 2856–2866.
- Giovanni, A., Ouaknine, M., Guelfucci, B., Yu, P., Zanaret, M., & Triglia, J. M. (1999). Nonlinear behavior of vocal fold vibration: The role of coupling between the vocal folds. *Journal of Voice*, *13*, 465–476.
- Guler, M. A., Elitok, K., Bayram, B., & Stelzmann, U. (2007). The influence of seat structure and passenger weight on the rollover crashworthiness of an intercity coach. *International Journal of Crashworthiness*, *12*, 567–580.
- Gunter, H. E. (2003). A mechanical model of vocal-fold collision with high spatial and temporal resolution. *The Journal of the Acoustical Society of America*, *113*, 994–1000.
- Hunter, E. J., Titze, I. R., & Alipour, F. (2004). A three-dimensional model of vocal fold abduction & adduction. *The Journal of the Acoustical Society of America*, *115*, 1747–1759.
- Jiang, W., Zheng, X., & Xue, Q. (2017). Computational Modeling of Fluid–Structure–Acoustics Interaction during Voice Production. *Frontiers in Bioengineering and Biotechnology*, *5*, 1–10.
- Kayabaşı, O., Yüzbasioğlu, E., & Erzincanlı, F. (2006). Static, dynamic and fatigue behaviors of dental implant using finite element method. *Advances in Engineering Software*, *37*, 649–658.
- Kerdok, A. E., Cotin, S. M., Ottensmeyer, M. P., Galea, A. M., Howe, R. D., & Dawson, S. L. (2003). Truth cube: Establishing physical standards for soft tissue simulation. *Medical Image Analysis*, *7*, 283–291.
- Kim, J., Kim, D., & Choi, H. (2001). An Immersed-Boundary Finite-Volume Method for Simulations of Flow in Complex Geometries. *Journal of Computational Physics*, *171*, 132–150.
- Kim, J., Yim, E., Jeon, C., Jung, C., & Han, B. (2012). Cold performance of various biodiesel fuel blends at low temperature. *International Journal of ...*, *13*, 293–300.
- Luo, H., Dai, H., Sousa, P. J. S. a F. De, & Yin, B. (n.d.). On the numerical oscillation of the direct-forcing immersed-boundary method for moving boundaries Fluid Solid body Solid body Extrapolated node Fluid Fluid n Solid body n Interpolated node, *1*, 1–27.
- Malo, R.C. (2018, December 1). *Stress Strain Diagram For mild Steel and Concrete*. Retrieved from <https://www.howtocivil.com/stress-strain-diagram-mild-steel-concrete-civil/>.
- Mendelsohn, A. H. (2011). Phonation threshold pressure and onset frequency in a two-layer physical model of the vocal folds. *The Journal of the Acoustical Society of America*, *130*, 2961–2968.

- Mittal, R., Dong, H., Bozkurttas, M., Najjar, F. M., Vargas, A., & von Loebbecke, A. (2008). A versatile sharp interface immersed boundary method for incompressible flows with complex boundaries. *Journal of Computational Physics*, 227, 4825–4852.
- Mittal, R., & Iaccarino, G. (2005). Immersed Boundary Methods. *Annual Review of Fluid Mechanics*, 37, 239–261.
- Mori, Y., & Peskin, C. S. (2008). Implicit second-order immersed boundary methods with boundary mass. *Computer Methods in Applied Mechanics and Engineering*, 197, 2049–2067.
- Murray, P. R. (2011). Flow-induced Responses of Normal , Bowed , and Augmented Synthetic Vocal Fold Models.
- Naghibi Beidokhti, H., Janssen, D., Khoshgoftar, M., Sprengers, A., Perdahcioglu, E. S., Van den Boogaard, T., & Verdonschot, N. (2016). A comparison between dynamic implicit and explicit finite element simulations of the native knee joint. *Medical Engineering and Physics*, 38, 1123–1130.
- National Institute on Deafness and Other Communication Disorders (2016, June 7). *Taking Care of Your Voice*. Retrieved from <https://www.nidcd.nih.gov/health/taking-care-your-voice>.
- Neubauer, J., Zhang, Z., Miraghaie, R., & Berry, D. a. (2007). Coherent structures of the near field flow in a self-oscillating physical model of the vocal folds. *The Journal of the Acoustical Society of America*, 121, 1102–1118.
- Ou Pont. (2018, June 12). *Teflon PTFE*. Retrieved from [http://www.rjchase.com/ptfe\\_handbook.pdf](http://www.rjchase.com/ptfe_handbook.pdf).
- Ouyang, H., Nack, W., Yuan, Y., & Chen, F. (2005). Numerical analysis of automotive disc brake squeal: a review. *Int. J. Vehicle Noise and Vibration*, 1, 207–231.
- Peskin, C. S. (2002). The immersed boundary method. *Acta Numerica*, 11, 479–517.
- Pickup, B. A. (2010). Influence of Material and Geometric Parameters on the Flow-Induced Vibration of Vocal Folds Models.
- Pickup, B. A., & Thomson, S. L. (2009). Influence of asymmetric stiffness on the structural and aerodynamic response of synthetic vocal fold models. *Journal of Biomechanics*, 42, 2219–2225.
- Poppy, P. (2017, June 5). *Anatomy and physiology of the larynx*. Retrieved from <http://slideplayer.com/user/12343952/>.
- Radina, (2016, Aug. 17). *Respiratory System*. Retrieved from <https://www.mendeley.com/guides/apa-citation-guide>.
- Riede, T., Tokuda, I. T., Munger, J. B., & Thomson, S. L. (2008). Mammalian laryngeal air sacs add variability to the vocal tract impedance: Physical and computational modeling. *The Journal of the Acoustical Society of America*, 124, 634–647.
- Scherer, R. C., Shinwari, D., De Witt, K. J., Zhang, C., Kucinski, B. R., & Afjeh, A. A. (2001). Intraglottal pressure profiles for a symmetric and oblique glottis with a divergence angle of 10 degrees. *The Journal of the Acoustical Society of America*, 109, 1616–1630.

- Schindler, A., Bottero, A., Capaccio, P., Ginocchio, D., Adorni, F., & Ottaviani, F. (2008). Vocal Improvement After Voice Therapy in Unilateral Vocal Fold Paralysis. *Journal of Voice*, 22, 113–118.
- Seo, J. H., & Mittal, R. (2011). A sharp-interface immersed boundary method with improved mass conservation and reduced spurious pressure oscillations. *Journal of Computational Physics*, 230, 7347–7363.
- Story, B. H. (2015). 3 Mechanisms of Voice Production.
- Sulica, L., & Blitzer, A. (2006). Vocal Fold Paralysis.
- Tao, C., Jiang, J. J., & Zhang, Y. (2006). Simulation of vocal fold impact pressures with a self-oscillating finite-element model. *The Journal of the Acoustical Society of America*, 119, 3987–3994.
- Thomson, S. L., Mongeau, L., & Frankel, S. H. (2005). Aerodynamic transfer of energy to the vocal folds. *The Journal of the Acoustical Society of America*, 118, 1689–1700.
- Trichês Júnior, M., Gerges, S. N. Y., & Jordan, R. (2008). Analysis of brake squeal noise using the finite element method: A parametric study. *Applied Acoustics*, 69, 147–162.
- Tsai, M. S., Yang, M. Y., Chang, G. H., Tsai, Y. Te, Lin, M. H., & Hsu, C. M. (2017). Autologous thyroid cartilage graft implantation in medialization laryngoplasty: A modified approach for treating unilateral vocal fold paralysis. *Scientific Reports*, 7, 1–8.
- Vampola, T., Laukkanen, A. M., Horacek, J., & Svec, J. G. (2011). Vocal tract changes caused by phonation into a tube: a case study using computer tomography and finite-element modeling. *J Acoust Soc Am*, 129, 310–5.
- Wang, W. Q., Liang, D. K., Yang, D. Z., & Qi, M. (2006). Analysis of the transient expansion behavior and design optimization of coronary stents by finite element method. *Journal of Biomechanics*, 39, 21–32.
- Wikiversity. (2017, July 26). *Nonlinear finite elements/Nonlinearities in solid mechanics*. Retrieved from [https://en.wikiversity.org/wiki/Nonlinear\\_finite\\_elements/Nonlinearities\\_in\\_solid\\_mechanics](https://en.wikiversity.org/wiki/Nonlinear_finite_elements/Nonlinearities_in_solid_mechanics).
- Witteman, W. J., & Kriens, P. R. F. C. (1993). the Necessity of an Adaptive Vehicle Structure Deceleration Pulses for Different Crash Velocities, 1–10.
- Wittenberg, T., Tigges, M., Mergell, P., & Eysholdt, U. (2000). Functional imaging of vocal fold vibration: Digital multislice high-speed kymography. *Journal of Voice*, 14, 422–442.
- Xue, Q., Mittal, R., Zheng, X., & Bielamowicz, S. (2012). Computational modeling of phonatory dynamics in a tubular three-dimensional model of the human larynx. *The Journal of the Acoustical Society of America*, 132, 1602–1613.
- Zhang, Z., Neubauer, J., & Berry, D. A. (2006). The influence of subglottal acoustics on laboratory models of phonation. *The Journal of the Acoustical Society of America*, 120, 1558–1569.
- Zheng, X., Mittal, R., & Bielamowicz, S. (2011). A computational study of asymmetric glottal jet deflection during phonation. *The Journal of the Acoustical Society of America*, 129, 2133–2143.

## APPENDICES

### APPENDIX A: Draft data of elasticity experiments on synthetic material

Table 8. Draft data of elasticity experiments on synthetic material

Weight No.	Mass (kg)	Applied force (N)	Value at end 1 (cm)	Measurement 1 (cm)	Measurement 2 (cm)	Avg. Meas. (cm)	Length (cm)	Delta L (cm)
0	0.00000	0	1.80	14.96	15.05	15.01	13.21	0
1	0.00374	0.03668	1.80	15.18	15.28	15.23	13.43	0.22
2	0.00561	0.05502	1.80	15.29	15.39	15.34	13.54	0.33
3	0.00650	0.06374	1.80	15.40	15.43	15.42	13.62	0.405
4	0.00800	0.07845	1.80	15.48	15.54	15.51	13.71	0.5
5	0.01650	0.16181	1.80	16.07	16.18	16.13	14.33	1.115
6	0.02400	0.23536	1.80	16.64	16.78	16.71	14.91	1.7
7	0.04500	0.44130	1.80	18.51	18.81	18.66	16.86	3.65
8	0.09250	0.90712	1.80	24.01	24.32	24.17	22.37	9.155
9	0.11100	1.08854	1.80	26.52	26.85	26.69	24.89	11.675
10	0.12700	1.24544	1.80	28.69	29.10	28.90	27.10	13.885
11	0.13200	1.29448	1.80	29.27	29.90	29.59	27.79	14.575
12	0.14800	1.45138	1.80	31.43	31.78	31.61	29.81	16.595
13	0.16500	1.61810	1.80	33.45	33.92	33.69	31.89	18.675
14	0.17800	1.74558	1.80	35.00	35.70	35.35	33.55	20.34
15	0.19400	1.90249	1.80	36.78	37.68	37.23	35.43	22.22
16	0.22000	2.15746	1.80	39.20	40.30	39.75	37.95	24.74
17	0.23900	2.34379	1.80	40.88	41.99	41.44	39.64	26.425
18	0.26000	2.54973	1.80	43.80	43.55	43.68	41.88	28.665
19	0.27200	2.66741	1.80	43.61	44.99	44.30	42.50	29.29
20	0.29300	2.87335	1.80	45.82	45.80	45.81	44.01	30.8
21	0.32300	3.16755	1.80	47.30	47.53	47.42	45.62	32.405

## **BIOGRAPHY OF THE AUTHOR**

Hai Zi was born in Zunhua, Hebei, China on May, 1992. He was raised there for 17 years by his parents Zhanzhong Zi and Cuiying Li until graduated from the First High School in Zunhua, Hebei in 2009. For his short-lived life in America, he has been nicknamed “Hai”, means “ocean” in Chinese. After National Entrance Exam in China, he was admitted into China Agricultural University and graduated in 2013 with a Bachelor’s degree in Engineering. Without requiring entrance examinations from candidates on recommendation, he graduated in 2015 with a Master’s degree in Engineering. In the summer of 2016, he entered the Mechanical Engineering program at the University of Maine. He transferred from Ph.D. to Master program at April, 2017. Hai was a candidate for the Master of Science degree in Mechanical Engineering from the University of Maine in August 2018.